Spring 2009

The corrosion of Ni_3Si alloys in sulfuric acid

Christopher Marc Larson

Department:

THE CORROSION OF NI3SI ALLOYS IN SULFURIC ACID

by

CHRISTOPHER M. LARSON

A THESIS

Presented to the Faculty of the Graduate School of the

MISSOURI UNIVERSITY OF SCIENCE AND TECHNOLOGY

In Partial Fulfillment of the Requirements for the Degree

MASTER OF SCIENCE IN MATERIALS SCIENCE AND ENGINEERING

2009

Approved by

Richard K. Brow, Advisor
Joseph W. Newkirk
F. Scott Miller

ABSTRACT

Hydrogen production from water, the world's most renewable natural resource, can provide an economical and sustainable form of energy for the future. One means to achieve this is with a nuclear reactor-based sulfur-iodine (S-I) thermochemical cycle. Currently there are few materials available, other than precious metals like gold and platinum, that possess the corrosion resistance and mechanical properties required for the sulfuric acid decomposition loop of the S-I process. However, alloys based on Ni_3Si show promise to be a more affordable, corrosion resistant materials option for this technology. In this study, the corrosion behavior of $NiSi_{22}$ and $NiSi_{20}(Nb,Ti)_3$ alloys in boiling 70 wt. % sulfuric acid is examined. The mechanism that provides corrosion resistance for these alloys is the formation of an inert SiO_2 surface film which spontaneously grows in oxidizing acid mediums. However, niobium and titanium alloying each have very different effects on the corrosion behavior. The results presented herein indicate that niobium alloying enhances the corrosion resistance of Ni_3Si, whereas titanium alloying has deleterious effects. The changes in corrosion behavior that are imparted by niobium and titanium alloying are linked to the alloy properties, and are the focus of this research.

ACKNOWLEDGMENTS

Many people have helped me throughout the course of my Master's degree, both on a personal level and academically. Without the support from these people this research would not have been possible, and I am very thankful for that.

I would first like to thank my loved ones for their support. This includes my dear friend Arason Parkman, my immediate family; Jeanie, Margaret, Mary, and Warren Larson, and my darling adorable grandmother Barbara Fickel. Their love and support has been the best thing that I have.

My deepest thanks go to Richard Brow, my advisor, whose wisdom and guidance has been invaluable to me. I thank Joseph Newkirk (the principal investigator of this project) for his keen insight into the metallurgical aspects of this research. Special thanks also go to Scott Miller for his expert assistance with the surface characterization techniques used in this research.

I express my deepest thanks to my fellow students who have assisted me throughout my Master's degree. They include Jen Hsien Hsu, Ryan Hedrick, and Ryan Moore. Special thanks also go to Jeff Wight of the Materials Research Center at the Missouri University of Science and Technology for his assistance with Auger and X-ray photoelectron spectroscopy experiments. Much of the data collected for this thesis are a direct result of his efforts. To that end I must also thank Harry Meyer of the High Temperature Materials Laboratory (HTML) at Oak Ridge National Lab (ORNL) for his assistance with scanning Auger and x-ray photoelectron spectroscopy experiments, and Tom Lillo of Idaho National Laboratory (INL) for use of his corrosion testing facility.

Finally, I would like to thank the Nuclear Energy Research Initiative branch of the United States Department of Energy for their financial support of this research (Grant number DE-FC07-061D14753).

TABLE OF CONTENTS

Page

LIST OF ILLUSTRATIONS

Page

LIST OF TABLES

Page

1. INTRODUCTION TO Ni_3Si BASED INTERMETALLICS

There have been significant efforts to develop nickel intermetallics for aerospace, petrochemical, and nuclear industries in recent years. Nickel silicides have physical, chemical, and electronic properties that distinguish them from other nickel intermetallics. They come in a variety of stoichiometric forms; $NiSi_2$, NiSi, Ni_3Si_2, Ni_2Si, Ni_5Si_2. Ni_3Si in particular has a desirable combination of increased tensile strength with elevated temperature, along with excellent resistance to oxidizing aqueous environments (particularly sulfuric acid). This makes it an attractive materials option for high temperature structural and corrosive acid containment applications. However, because Ni_3Si is inherently brittle, the production of large scale industrial parts has proven to be prohibitively difficult.

Alloying processes have been explored in attempts to improve the mechanical properties of Ni_3Si, but only with limited success. These studies have been aimed at determining the effects of alloying elements on the mechanical properties, determining the effects of alloying elements on the microstructure, and correlating the observed changes in properties with the microstructure and composition.

This chapter provides a review of the research that has been done on the mechanical and corrosion properties of Ni_3Si alloys. Descriptions of the fundamental principles of corrosion film formation are provided. Finally, an overview of the S-I thermochemical cycle for the production of hydrogen is provided and its materials requirements are discussed.

1.1. MICROSTRUCTURE AND MECHANICAL PROPERTIES

Ni_3Si has an $L1_2$ crystal structure that is based on the face-centered cubic lattice (see Figure 1.1). The lattice parameter of Ni_3Si is 0.3497 nm [1]. The Ni-Si phase diagram displayed in Figure 1.2 shows that the β_1 phase is stable between 23 & 25 at% Si. As-cast Ni_3Si alloys have polyphasic microstructures consisting of alpha, beta, and gamma phases [1]. According to the phase diagram, a homogeneous β_1 phase microstructure is thermodynamically obtainable through heat treatment below 1035 ºC.

However, experiments have indicated that these polyphasic microstructures are difficult to homogenize thermally [2].

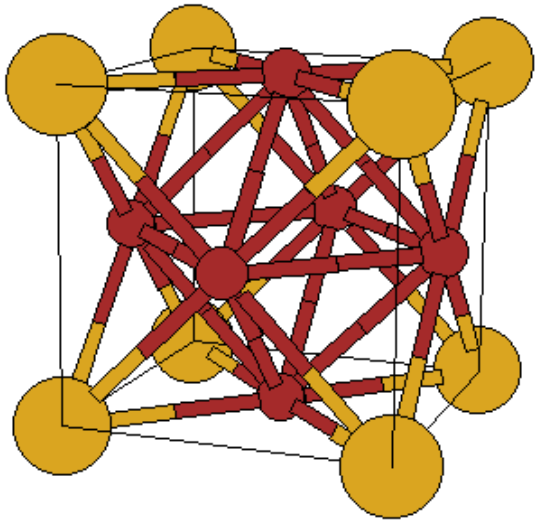

Figure 1.1 The $L1_2$ face-centered cubic crystal structure of Ni_3Si.

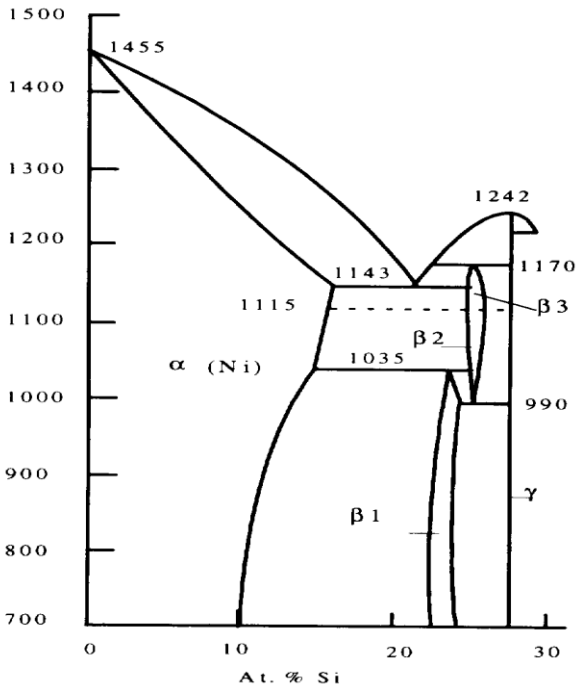

Figure 1.2 The nickel-rich portion of the Ni-Si phase diagram [3].

Ni_3Si exhibits increasing yield stress with increasing temperature [3]. While this is an attractive property for structural applications, the low ductility of Ni_3Si makes it impractical to produce wrought products such as pipes. Attempts to forge and roll Ni_3Si have been unsuccessful. As a result many researchers have explored alternate alloying options.

The affect of boron on the mechanical properties of Ni_3Al was previously studied by Aoki and Izumi [4]. They showed that the ductility of Ni_3Al, which has the same crystal structure and comparable properties to Ni_3Si, could be increased up to 35% with the addition of small quantities (< 500 ppm) of boron. It was reported that the improvement in ductility was caused by boron segregation to grain boundaries, which significantly reduced grain boundary embrittlement.

Schulson et al reported that boron additions to Ni_3Si only increased its ductility by 2-5% [5]. One explanation for why boron affected Ni_3Al and Ni_3Si differently was provided by Lui et al [6], who studied the effect of boron on the fracture behavior of $NiSi_{22.5}$. These authors suggested that unlike the Ni_3Al system, boron did not affect the grain boundary cohesion of Ni_3Si, and this explains why it showed very little improvement in room temperature tensile ductility. Other studies of boron segregation in Ni_3Si alloys seem to corroborate that conclusion.

The effects of ternary alloying on the mechanical properties of Ni_3Si have also previously been studied. Takasugi et al [1] discovered that titanium is soluble in Ni_3Si up to 11 at. % as a substitute for silicon. Titanium contents of greater than 2 at% were shown to eliminate the polyphasic structures observed in unalloyed Ni_3Si, as well as stabilize the $L1_2$ β_1-phase. Strength tests revealed that the presence of titanium significantly enhanced ductility. Figure 1.3 shows a compressive yield stress vs. temperature plot of Ni_3Si alloys containing between zero and 11.3 at. % titanium. Alloys containing titanium exhibit enhanced strengths.

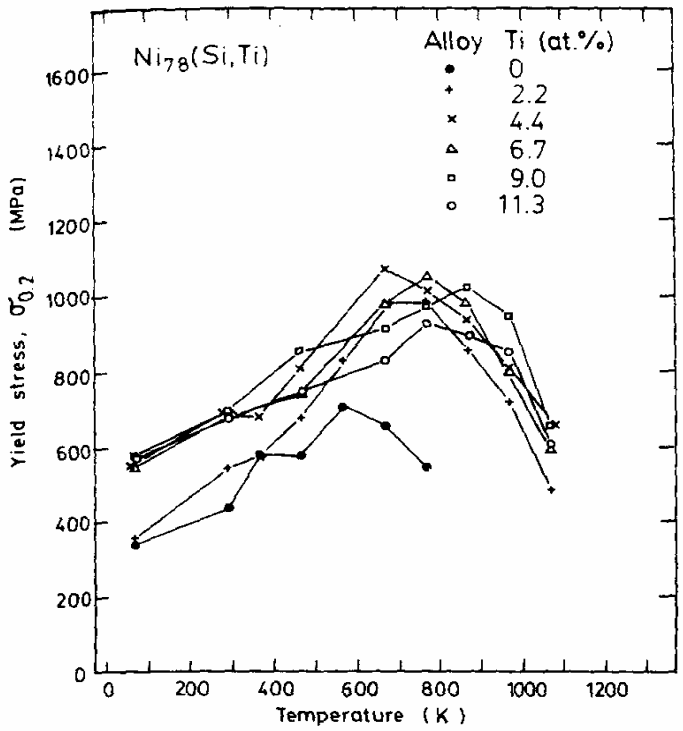

Figure 1.3 The dependence of titanium concentration on the mechanical strength of $Ni_3(Si,Ti)$ [1].

Niobium and vanadium additions have been shown to enhance the room temperature ductility of Ni_3Si. Jang [7] observed that niobium concentrations of up to 5 at. % stabilized the β_1 phase by allowing it to form directly from the melt rather than through a liquid-solid or solid-solid reaction. It was suggested that the improved tensile ductility of $NiSi_{19}Nb_3$ was imparted by the lattice expansion of the matrix β_1 phase caused by the presence of niobium, as well as by the strain imparted by Nb-rich precipitates on the matrix β_1 phase. Boron additions further improved mechanical properties. The addition of 400 ppm boron increased the elongation three-fold and the ultimate strength by 60% compared to the un-doped alloy. In addition, boron had a positive impact on the fracture mode, changing it from brittle to ductile behavior. Takasugi suggested that boron enhances the shape of Nb-rich precipitates (which are a medium for crack propagation), and thus makes the alloy more crack resistant.

Zhang et al. [2] found that the tensile properties of Ni-Si-Nb-B alloys are very sensitive to composition. Figure 1.4 shows a proposed ternary Ni-Si-Nb phase diagram showing the compositional window of interest for this system. It can be seen that silicon

contents of greater than 20 at. % lead to the presence of hard needle-like γ phases, which impart brittleness, whereas silicon contents of less than 18 at. % lead to the presence of α phase which have negative effects on both the corrosion resistance and mechanical properties. Zhang demonstrated that α and γ phases could be eliminated with heat-treatments of as-cast $NiSi_{20}Nb_3B_{0.5}$ alloys, but heat treatments had little effect on Nb-rich precipitates.

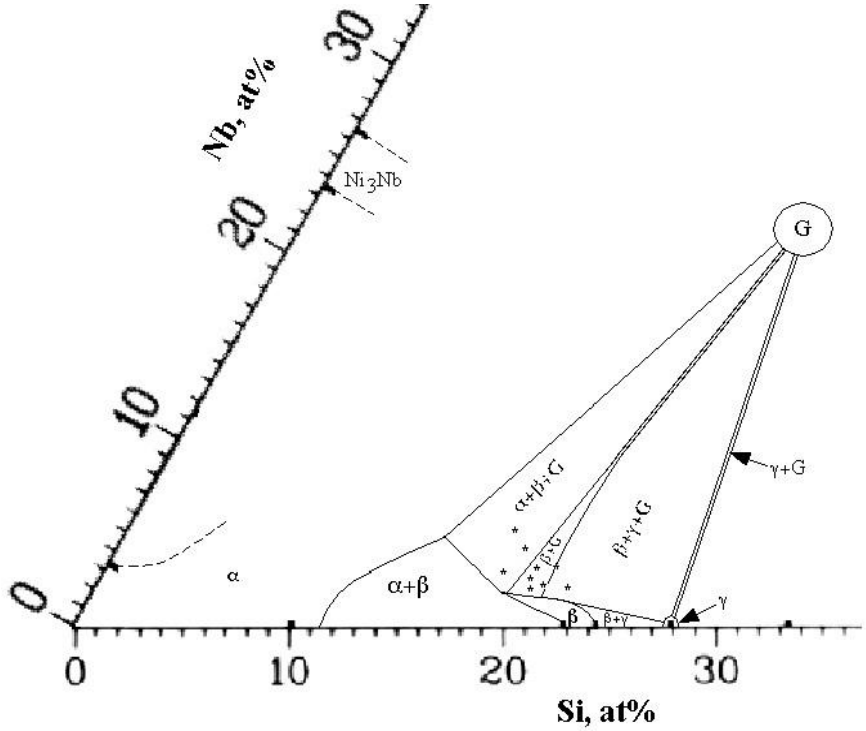

Figure 1.4 Proposed 950 ºC isotherm of the Ni-Si-Nb system with 0.5 at% B [2].

The synergistic effects of Nb and Ti on the mechanical properties were also explored by Zhang [2]. It was found that the addition of 0.5-1 at. % Ti to $NiSi_{20}Nb_3B_{0.05}$ encouraged the formation of Nb-rich precipitates and by doing so decreased the mechanical strength and the ductility of the alloy. A significant increase in grain boundary embrittlement was also observed.

1.2. CORROSION AND OXIDATION BEHAVIOR

Intermetallic alloys have long been known to resist corrosive attack by aqueous solutions. Alloys based on Ni_3Al, FeAl, TiAl, and Ni_3Si have been developed for corrosion resistant applications. Alloys based on Ni_3Si and Fe_3Si are perhaps the best candidates for sulfuric applications due to their tendency to form protective silica films in sulfuric acid environments. Fe_3Si however is extremely brittle [4]. Hastelloy D ($NiSi_{10}Cu_3$), which was developed in the 1920's for sulfuric acid containment applications, has had the greatest technological impact of any Ni_3Si alloy developed to date. It was developed with an improved understanding of the physical metallurgy of nickel alloys, especially the effects that alloying elements have on the mechanical and corrosion properties. Hastelloy D has a microstructure consisting of $\alpha + \beta$ dendrites with $\beta + \gamma$ in interdendritic regions. It performs well in a wide concentration range of sulfuric acid. Kumar [9] found that heat treatments of the alloy tended to increase the corrosion rate, which was believed to be due to the formation of a secondary β_2 phase which has less resistance than the β_1-phase. However, the ductility of the alloy was significantly enhanced due to the absence of the γ-phases following heat treatment.

Takasugi et al. [10] found that ternary Ni-Si-Cr alloys with 3 at. % Cr and 0.005 at. % B had superior corrosion resistance to Hastelloy D in 60 wt. % sulfuric acid solution. Its microstructure consists of β_1, α, and γ phases. The addition of 1 at.% Cu along with heat treatment at 950 °C for 50 hours eliminated the γ phase completely and enhanced the corrosion resistance.

In addition to studies dealing with corrosion and oxidation of Ni_3Si alloys in aqueous environments, some work has also been done on the corrosion behavior in gaseous environments. Takasugi et al. [8] studied the microstructure, high temperature compressive and tensile deformation, and oxidation behavior of alloys based on the $Ni_3(Si,Nb,Ti)$ system. It was concluded that oxidation resistance at 1000 °C in air was imparted by a continuous SiO_2 surface film. Furthermore, the oxidation behavior was found to be sensitive to composition (i.e. silicon content), but not microstructure. Takashi found that the alloy with the highest silicon content ($NiSi_{8.2}Ti_{8.2}Nb_{4.1}B_{50ppm}$) exhibited the best overall corrosion and oxidation resistance.

Lui et al. [11] studied the high temperature oxidation behavior of $NiSi_{19}$ and $NiSi_{19}Cr_8$ alloys in air. The isothermal oxidation kinetics in the range of 500 – 900 °C was determined via weight measurements. The oxidation kinetics did not exhibit a parabolic growth rate law, but rather a power law of the form $\Delta W^n = kt$ with n values ranging from 2.7 to 4.9. At lower temperatures (< 800 °C), oxides were identified as NiO. At higher temperatures, thin silica layers were found to be formed at the base of the NiO layer. It was suggested by Lui that at elevated temperatures the thermodynamics become favorable for SiO_2 formation, however due to the inert behavior of SiO_2 at lower temperatures further oxidation of Si ceases. Oxide growth stresses caused micro-cracks in the silica layer which allowed for rapid diffusion of Ni^{2+} ions through the film, which subsequently allowed for the formation of a NiO scale directly above the protective silica layer. Figure 1.5 illustrates the effect of Si concentration on the oxidation of Ni-Si alloys at high temperatures.

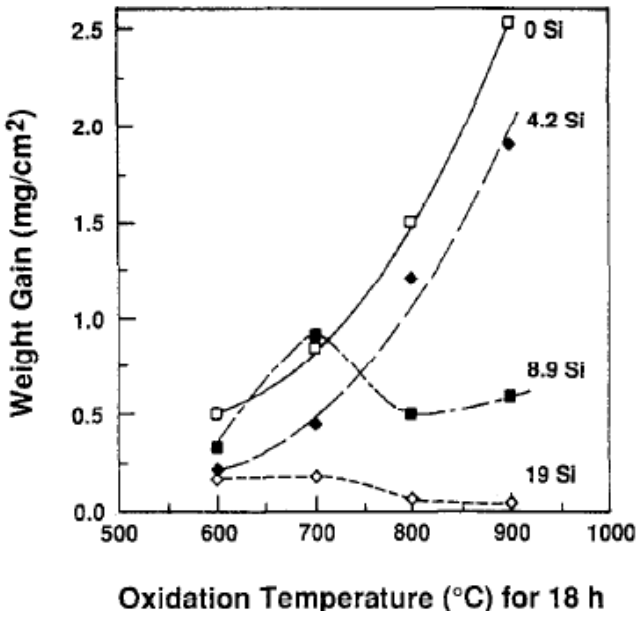

Figure 1.5 Mass gain vs. heating temperature showing the effect of silicon content on the oxidation behavior of binary Ni-Si alloys [11].

1.3. OVERVIEW OF PASSIVE CORROSION FILMS

Perhaps the most important factor influencing the corrosion protection of metals and alloys is passivity. Passivity is described by a significant decrease in the corrosion rate of a metal due to the formation of a surface film that provides a barrier to ionic diffusion. Reactions between metals and their environments (gaseous or liquid) typically result in the formation of a surface film, which most commonly consists of polycrystalline or amorphous metal oxides, sulfides, and/or hydrates. When a corrosion film is established at the surface, any further corrosion must result from either the diffusion of metal ions and/or oxygen/sulfur/water through the film, or from detachment of the film itself. Because these surface films have significantly lower electronic conductivities and ionic diffusivities than the underlying metal, a significant decrease in the corrosion rate is observed. This is the basic nature of all passivation processes and it is of fundamental importance to the development of corrosion resistant materials.

While thermodynamics dictate the initial reactions that occur at a metal-environment interface, other factors such as growth kinetics, ionic diffusivity, electronic conductivity, thermal expansion differences between the alloy and its surface film, and film stresses determine the durability of the corrosion film. Numerous models have been developed to explain these properties. They generally are concerned with one of two different phenomena: 1) growth kinetics and the transport of mass and charge, or 2) electronic properties. While these phenomena are intimately related, the mathematical approaches used to model each are different. The focus of this review will be on growth kinetics and mass/charge transport as these phenomena are most relevant to the present study.

One of the earliest attempts to model the oxidation of alloys in gaseous environments was provided by Pilling and Bedworth [12]. It had been observed that high temperature metal oxidation often obeyed a parabolic growth rate law of the form $L(t) \alpha t^{1/2}$, where L(t) is the thickness of the film as a function of time. Starting with Fick's first law, they derived a parabolic growth law for the film thickness (L) using four assumptions: 1) diffusing species are charge neutral 2) the diffusion coefficient D is independent of the concentration of diffusing species C, 3) the concentration of diffusing species at the metal/oxide and oxide/gas interfaces (C(0) and C(L)) are independent of

the film thickness, and 4) the concentration of diffusing species is time independent. From these four assumptions they obtained an expression for the oxide thickness (L) shown in Equation 1.1.

$$L = \sqrt{2kt} \tag{1.1}$$

where the rate constant k = VD[C(0)-C(L)], and V is the volume of oxide formed with each atom diffusing through the oxide film. The Pilling-Bedworth parabolic growth law successfully accounts for the $t^{1/2}$ dependence of the film thickness observed for many metals in higher temperatures.

In addition to the parabolic growth law, Pilling and Bedworth proposed a set of guidelines to identify protective oxide coatings for corrosion protection. They noticed that the porosity of a metal oxide can be correlated with its specific density. The Pilling-Bedworth ratio (PBR) of a metal oxide is defined as the ratio of the volume of metal oxide to the volume of consumed metal. The Pilling-Bedworth ratio is shown in Equation 1.2.

$$PBR = \frac{V_{\text{metal oxide produced}}}{V_{\text{metal consumed}}} \tag{1.2}$$

When the PBR of a metal or alloy is less than 1, the metal oxide film tends to be porous and therefore non-protective because of its inability to cover the entire surface. A plot of weight gain versus time for such metals is typically linear. Alloys with PBR values between 1 and 2 are ideal for corrosion protection, and usually exhibit either logarithmic or parabolic weight gain behavior. For PRB values much larger than 1, compressive stresses within the oxide cause buckling and spalling which eventually lead to further corrosive attack. In this case the initial kinetics are typically parabolic or logarithmic, but with increasing time discontinuous jumps in the weight can be observed due to spalling. In addition to the PBR, factors such as the relative coefficients of thermal expansion and the adherence between the oxide and metal were found to be important in determining oxide durability.

Several models have been developed to describe the growth of passive films on metals and alloys in aqueous solutions. These models are based on experimental data indicating either a logarithmic or inverse logarithmic dependence of the film thickness on time. The general forms of these two laws are shown in Equations 1.3 and 1.4 respectively.

$$L(t)=A+B\ln(t) \tag{1.3}$$

$$L(t)=\frac{1}{C-D\ln(t)} \tag{1.4}$$

where L(t) is the film thickness, t is time, and A, B, C, and D are constants. Many authors have attempted to model the corrosion of alloys in aqueous media by deriving forms of these expressions using physical parameters.

The previous works of Wagner [13], Cabrera and Mott [14], Fehlner and Mott [15], Castro [16, 17], MacDonald et. al. [18], and numerous others, has been aimed at providing these physical models. Descriptions of these models can be found in appendix A.

1.4. MATERIALS REQUIREMENTS FOR THE S-I THERMOCHEMICAL CYCLE

The sulfur-iodine thermochemical cycle provides one means to generate large quantities of hydrogen [19]. Unfortunately, a lack of suitable structural materials has stymied its development. The coupled chemical reactions which constitute the S-I thermochemical cycle are shown in Figure 1.6. In the decomposition section of the cycle (the middle section in Figure 1.6), dilute 50 wt. % sulfuric acid is concentrated up to 98 wt. %, vaporized, and super-heated. Most commercial alloys designed for sulfuric acid handling rapidly dissolve under these conditions.

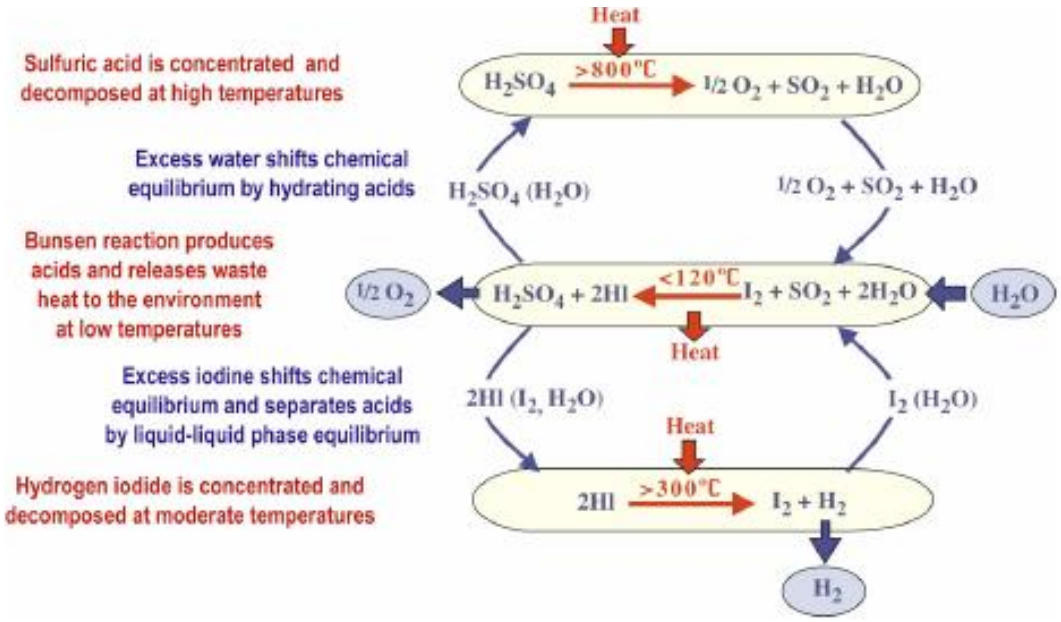

Figure 1.6 The coupled chemical reactions of the S-I hydrogen cycle.

Materials such as platinum, gold, quartz, silicon carbide, and certain high silicon iron alloys are the only materials options with demonstrated capability to resist these conditions. Unfortunately, these materials are either prohibitively expensive (e.g. Au and Pt), or exhibit a catastrophic failure mode due to low ductility (e.g. SiO_2, SiC, Fe_3Si). Therefore, a new material that exhibits the necessary corrosion resistance and mechanical integrity needs to be developed. Alloys based on Ni_3Si show promise as a more affordable and corrosion resistant materials option.

Past research has provided valuable insight into alloying processes that enhance the mechanical properties of Ni_3Si. Niobium and titanium additions in particular have proven to be effective at increasing ductility and tensile strength [1]. Their effects on the corrosion rate in concentrated boiling sulfuric acids, however, are not fully understood. Figure 1.7 summarizes work from Zhang [2] on Ni_3Si, $Ni_3(Si,Nb)$, and $Ni_3(Si,Ti)$ alloys in boiling 60, 70, and 80 wt. % sulfuric acid solutions.

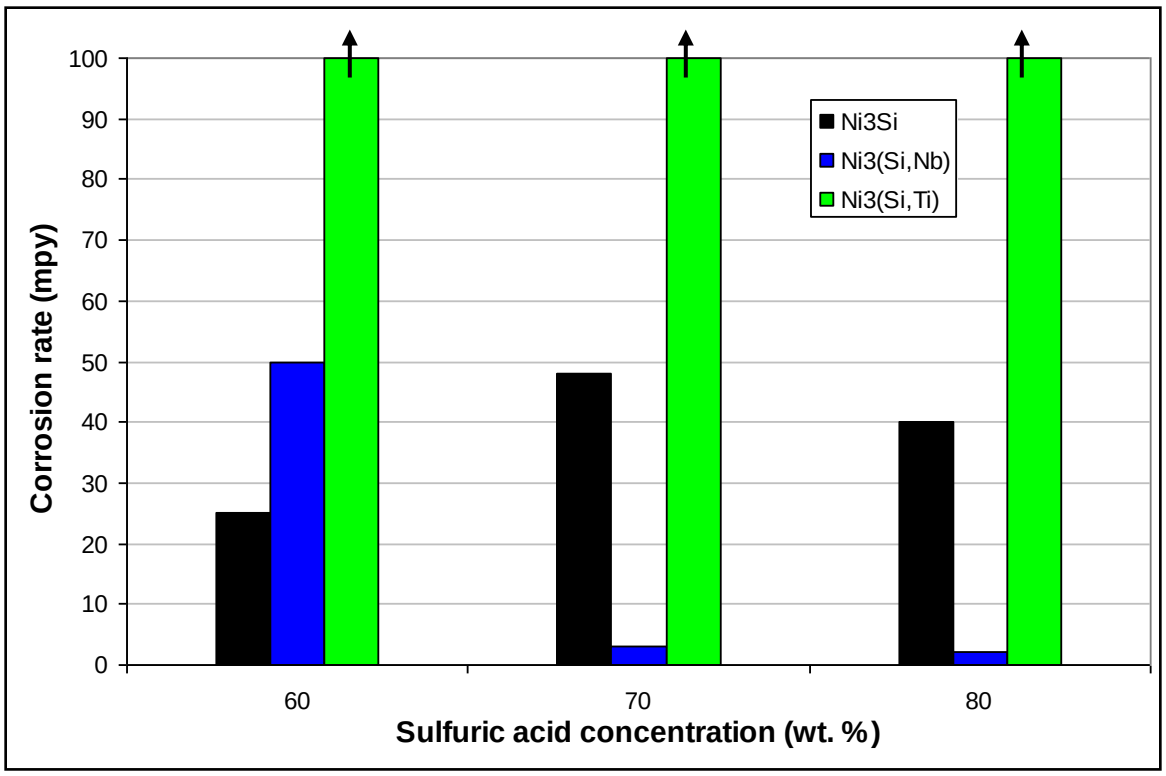

Figure 1.7 The corrosion rates of Ni_3Si alloys in boiling sulfuric acid [2].

Titanium additions appear to have deleterious effects on the corrosion rate of Ni_3Si in both reducing (60 wt. %), and oxidizing (70 and 80 wt. %) sulfuric acid solutions. Under oxidizing conditions the addition of niobium appears to provide enhanced corrosion protection. The extremely low corrosion rate of $Ni_3(Si,Nb)$ in boiling 70 wt. % solution is truly unique for an nickel alloy; the oxidizing power of sulfuric acid reaches a maximum at this concentration, and therefore most alloys corrode the fastest under this condition. $Ni_3(Si,Nb)$ exhibits anomalous behavior in this respect.

The objective of this research is to identify and understand the effects that niobium and titanium have on the corrosion behavior of Ni_3Si. Emphasis is placed on the correlation between the observed corrosion behavior and the properties of the alloy an corrosion film. Several key questions that are addressed in this research are listed below:

- What is the mechanism of corrosion protection in boiling 70 wt. % sulfuric acid?
- How does the presence of Nb and Ti affect the corrosion properties of the alloy?

- What effects do Nb and Ti have on the microstructure of the alloy?
- How does the microstructure affect the corrosion resistance?
- What mechanism governs passive film formation on Ni_3Si?
- Do Nb and Ti alter this mechanism?
- What role does S play in these films (i.e. sulfates or sulfides)?
- What role does B play in these films (i.e. borosilicate)?

A better understanding of the underlying mechanisms by which these alloy additions alter the corrosion behavior will provide insight into alternate alloying processes, and eventually lead to an alloy composition with enhanced corrosion resistance. The objective of this study is to answer these questions.

2. EXPERIMENTAL PROCEDURE

2.1. ALLOY FABRICATION

The Ni_3Si alloys studied in this research were fabricated by Zhang [2]. They were prepared by induction melting of the metal components (Inco Ni pellet, Si metal, Ni-Nb metal) in a graphite mold under an Argon atmosphere. Melts were held at 1500 °C for 15 minutes to allow for solution formation. The temperature was then decreased to 1350 °C and held for 5 minutes before the melts were cast into the graphite molds. For further information regarding alloy fabrication refer to Zhang [2].

The four alloy compositions studied here are listed in Table 2.1. Nominal compositions of the alloys are given under the "Alloy" column, while the analyzed compositions are shown in the right columns. Boron was added to all of the compositions studied for the purpose of improving the mechanical properties.

Table 2.1 Alloy compositions (atomic percent)

Alloy	Heat treatment	Alloy composition*				
		Ni	Si	Nb	Ti	B
"Ni-Si" $NiSi_{22}B_{0.01}$	900 °C for 24 hours in Ar	78.87	21.12	-	-	0.01
"Ni-Si-Nb" $NiSi_{20}Nb_3B_{0.05}$	900 °C for 24 hours in Ar	77.08	19.69	3.05	-	0.02
"Ni-Si-Ti" $NiSi_{20}Ti_3B_{0.025}$	900 °C for 24 hours in Ar	77.40	19.77	-	2.83	0
"Ni-Si-Nb-Ti" $NiSi_{19}Nb_3Ti_1B_{0.05}$	900 °C for 24 hours in Ar	79.17	17.02	3.16	0.66	0

* Analysis done by Climax Research Services. Accuracy of data with 95% confidence is: Si ± 3%, Nb ± 5%, B ± 10%.

2.2. CORROSION TESTING

Corrosion tests in sulfuric acid were performed in accordance with ASTM G31-72. The corrosion rates of Ni_3Si alloys were calculated using the formula given in Equation 2.1.

$$\text{Corrosion rate (mpy)} = \frac{365{,}000 \bullet \Delta m}{S \bullet \rho \bullet t} \tag{2.1}$$

where Δ m is the mass loss given in grams (g), S is the surface area of the test sample given in square inches (in^2), ρ is the density of the alloy given in grams per cubic inch (g/in^3), t is the testing time given in days. Tests were carried out in Pyrex flasks with a condensor attached to the top, as shown in Figure 2.1. Cold water was circulated through the condensor to liquefy hot vapors from the boiling solution. The Pyrex container was surrounded with copper shot in a stainless steel container, which in turn sat on a hot plate. Copper shot was put in place as a safety precaution to neutralize the acid in a controlled manor in the event of a spill. A thermometer was used to monitor the temperature of the acid, which was kept at the boiling temperature throughout the duration of testing. The corrosion tests were carried out in 70 wt. % aqueous sulfuric acid solution at its boiling temperatures of 165 °C. Kinetic studies of alloy weight losses were performed by removing test samples from solution periodically and measuring their weight losses. Samples were removed from solution, rinsed for 5 seconds with de-ionized water, and then dried using compressed air. Weight measurements were taken on the dried alloy samples and then they were placed back into solution.

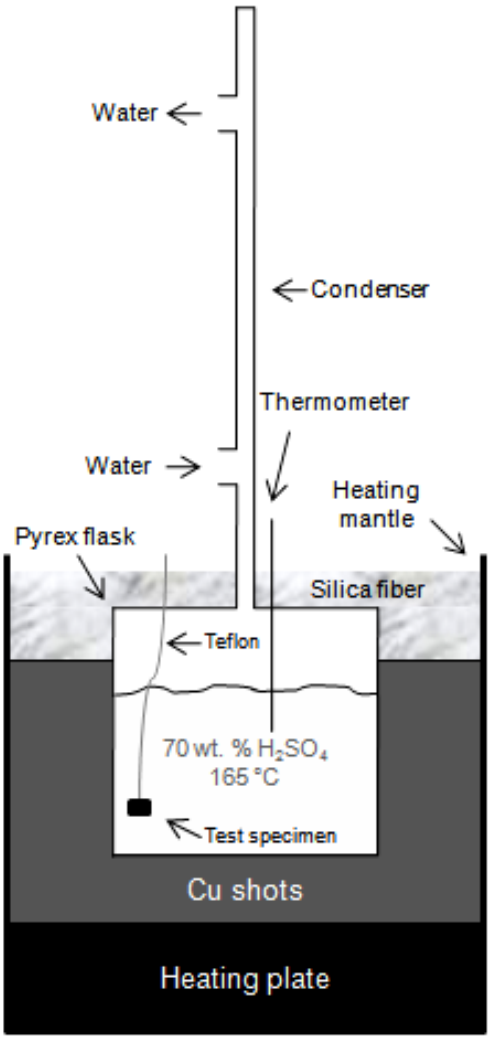

Figure 2.1 Corrosion testing apparatus used for corrosion experiments.

2.3. SAMPLE PREPARATION

Ni_3Si alloys were originally cast into cylindrical risers measuring 4.4 cm in diameter. These risers were subsequently cut into ~ 150 mm^3 test samples. Test samples were polished using silicon carbide paper ranging from 180 – 1200 grit. Fine polishing was performed using 3 and 6 μm diamond particle solutions. Cross-sections of corroded alloy surfaces were prepared by cutting them with a diamond blade, mounting them in an epoxy mold, and then polishing them using the said procedure.

2.4. SURFACE CHARACTERIZATION

2.4.1. X-ray photoelectron spectroscopy (XPS). For the experiments performed at the Missouri University of Science and Technology, a Kratos 165 Physical Electronics XPS instrument was used. An Mg Kα radiation source was operated at 15 kV with a beam current of 15 mA. Specimens were sputtered with argon ions accelerated through 4 kV at a current of 25 mA, yielding an approximate sputter rate of 10 nm/min. Scans were recorded on 'as received' samples and after 30 and 60 seconds of argon ion sputtering. Survey scans were taken with the detector biased at +80 kV and high resolution scans of each element were taken with the detector biased at +20 kV. All spectra are referenced to a C 1*s* binding energy of 284.6 eV. Differential charging was not considered in this analysis. Peaks were fit using KRATOS peak fitting software to find the relative peak areas of nickel, niobium, oxygen, and silicon photoelectron peaks, as well as the relative areas between metallic silicon and oxidized silicon photoelectron peaks.

The second set of experiments was conducted at the High Temperature Materials Laboratory at Oak Ridge National Lab. The system was a Thermo Scientific K-Alpha XPS with a monochromatic Al (Kα) x-ray source, hemispherical electron energy analyzer, Ar-ion sputter gun, and a charge compensation gun utilizing both low energy Ar-ions and low energy electrons. The x-ray spot size was 400 μm. Base pressure in the analysis chamber was ~ $5x10^{-9}$ torr and was maintained by introducing samples through an automated, turbo-pumped load-lock. Data were acquired and analyzed using the Avantage Software package.

2.4.2 Scanning Auger electron spectroscopy (AES). Scanning AES experiments were conducted at the High Temperature Materials Laboratory at Oak Ridge National Lab. The scanning Auger system was a Physical Electronics Phi-680 Scanning Auger Nanoprobe with a field emission electron gun, cylindrical mirror electron energy analyzer, and Ar-ion sputter gun. The energy and current of the probe electron beam was 20 kV and 10 nA, respectively, and gave a spot size for the probe beam of ~15 nm. The beam was held at fixed points to yield spectral information (i.e. surface composition) for that feature or rastered over a given area to give either secondary electron images or Auger elemental maps. Depth profiling was performed in selected areas by monitoring the Auger signal of selected elements while alternately sputtering for a given amount of

time. The sputter rate that was used (calibrated for a standard SiO_2 film) was 150 nm/min. The base pressure of the analysis chamber was ~5 x 10^{-10} torr and maintained by introducing the samples through a turbo-pumped load-lock. Data was acquired using Phi PC-Access software and analyzed using Phi MatLab software.

2.4.3. Scanning electron microscopy (SEM) and energy dispersive spectroscopy (EDS). Two SEM and EDS systems were used to characterize alloy surfaces. The first set of experiments was carried out in the Materials Research Center at the Missouri University of Science and Technology on a Hitachi S-570 equipped with a lanthanum hexaboride (LaB_6) electron gun. Data were processed using a 4Pi Spectral Engine II digital acquisition system for secondary electron imaging, backscatter electron imaging, and compositional mapping.

The second set of experiments was conducted at the High Temperature Materials Laboratory at Oak Ridge National Lab on a Hitachi S-3400 equipped with a lanthanum hexaboride (LaB_6) electron gun.

2.4.4. X-ray diffraction (XRD). X-ray diffraction patterns of alloy surfaces were taken with a Philips X'Pert diffractometer equipped with a Cu Kα radiation source. An X-ray mirror (PW3088/60) and a 0.18° parallel plate collimator were used as the incident beam and diffracted beam modules respectively. A fixed incident angle of 1° was maintained and the instrument was operated in the continuous mode with a step size of 0.03° and a counting time of 70 s.

2.4.5. Inductively coupled plasma mass spectrometry (ICP MS). The concentrations of dissolved Ni, Si, Nb, and Ti ions in sulfuric acid solutions following corrosion testing were measured with an Optima 2000 DV ICP MS instrument. Sulfuric acid test solutions were diluted with water to 5 % by volume, and subsequently by a factor of 10 with 1 vol. % HNO_3 prior to the experiments.

3. RESULTS

3.1. CORROSION BEHAVIOR

3.1.1. Corrosion kinetics. Figure 3.1.a. displays the mass losses of Ni-Si, Ni-Si-Nb, Ni-Si-Ti, and Ni-Si-Nb-Ti alloys in boiling 70 wt. % sulfuric acid. The obvious commonality between each of these alloys is the passivation. There is a clear transition from active corrosion to passive corrosion. This is evidenced by the significant decrease in the weight loss rate with increasing time. However, there are significant differences in both the amount of weight loss that occurs prior to passivation, and the amount of time taken to passivate, between the alloys. Perhaps the most significant difference is the weight loss discrepancy between the Ni-Si-Nb and Ni-Si-Ti alloys. Niobium alloying clearly improves the corrosion resistance of Ni_3Si, whereas titanium alloying decreases it significantly. The quaternary Ni-Si-Nb-Ti alloy shows decreased corrosion resistance relative to the Ni-Si alloy, although to a much lesser extent than the Ni-Si-Ti alloy.

Niobium and titanium alloying also appears to affect the corrosion kinetics. This is particularly evident in comparing the active corrosion regions of these alloys. Figure 3.1.b. displays the mass losses during the first 300 minutes of testing. The Ni-Si alloy shows a clear transition from active corrosion behavior to passive corrosion behavior near 150 minutes. On the other hand each of the alloys containing titanium exhibit intermediate regions in which the weight loss rate increases prior to the onset of passivation. This suggests that there are two active corrosion regions. The weight loss curve of the Ni-Si-Nb alloy does not show full maturation to the passive state, even though it exhibits the least amount of corrosion. Figure 3.2 - Figure 3.5 show the individual weight loss curves displayed in Figure 3.1.a., along with logarithmic representations of the data. These data are broken down into the individual active and passive regions. The two active regions observed on the titanium containing alloys are denoted as “Active I” and “Active II”.

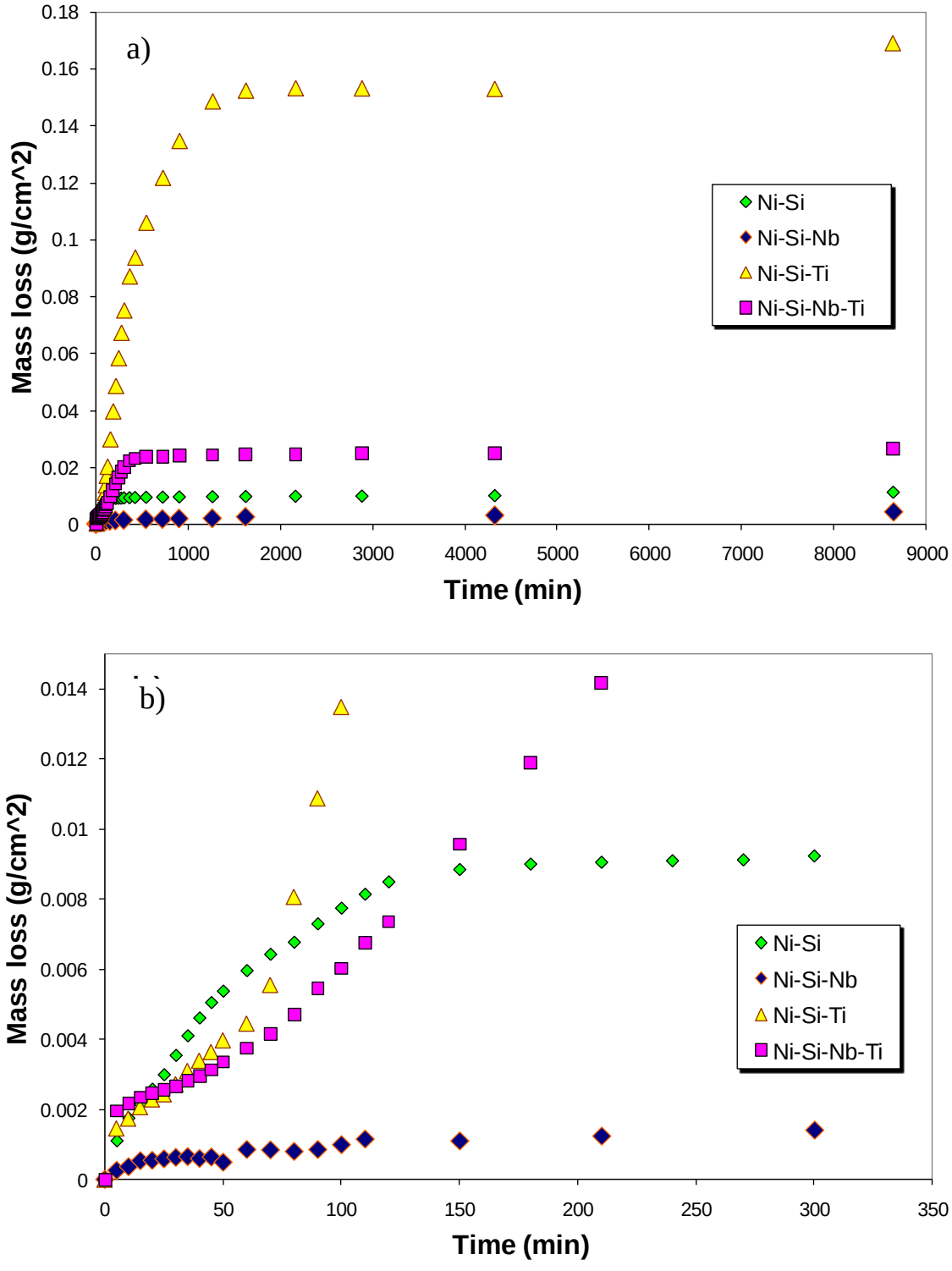

Figure 3.1 a) The mass losses of Ni-Si, Ni-Si-Nb, Ni-Si-Ti, and Ni-Si-Nb-Ti alloys during six days of exposure to boiling 70 wt. % sulfuric acid, and b) the mass losses during the initial 300 minutes.

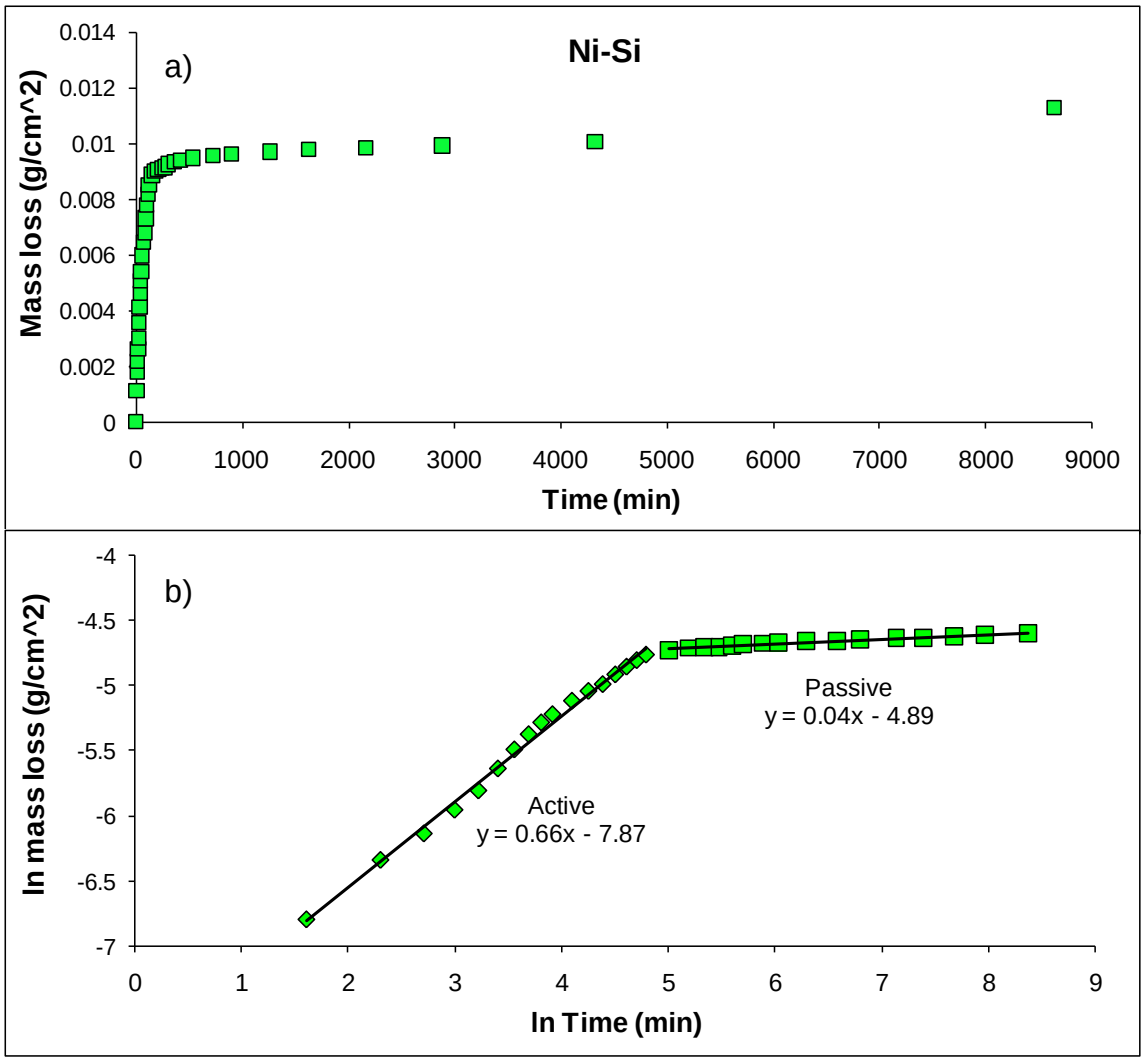

Figure 3.2 a) The mass loss of the Ni-Si alloy in boiling 70 wt. % sulfuric acid, and b) a logarithmic plot of the mass loss data shown in part a).

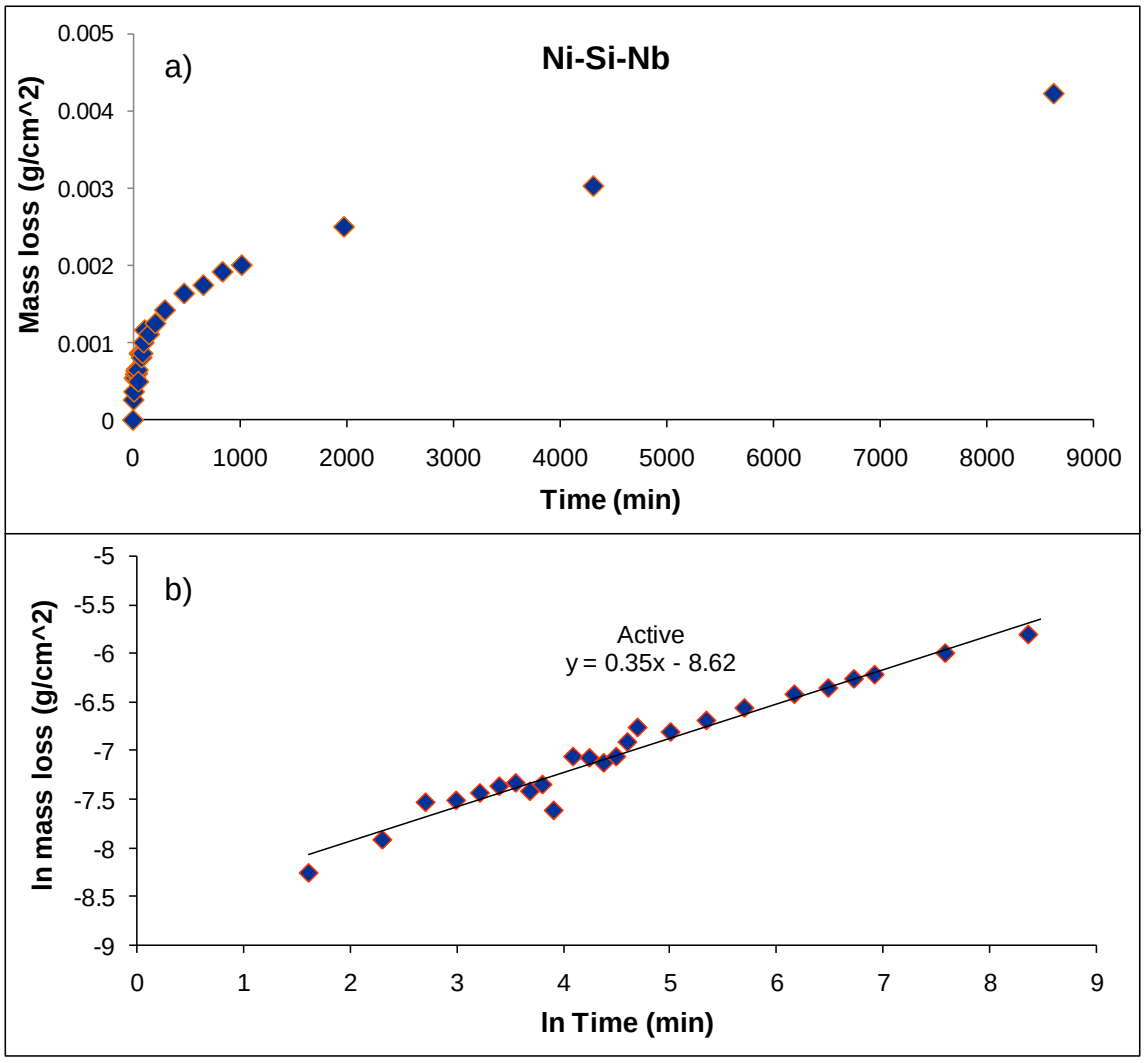

Figure 3.3 a) The mass loss of the Ni-Si-Nb alloy in boiling 70 wt. % sulfuric acid, and b) a logarithmic plot of the mass loss data shown in part a).

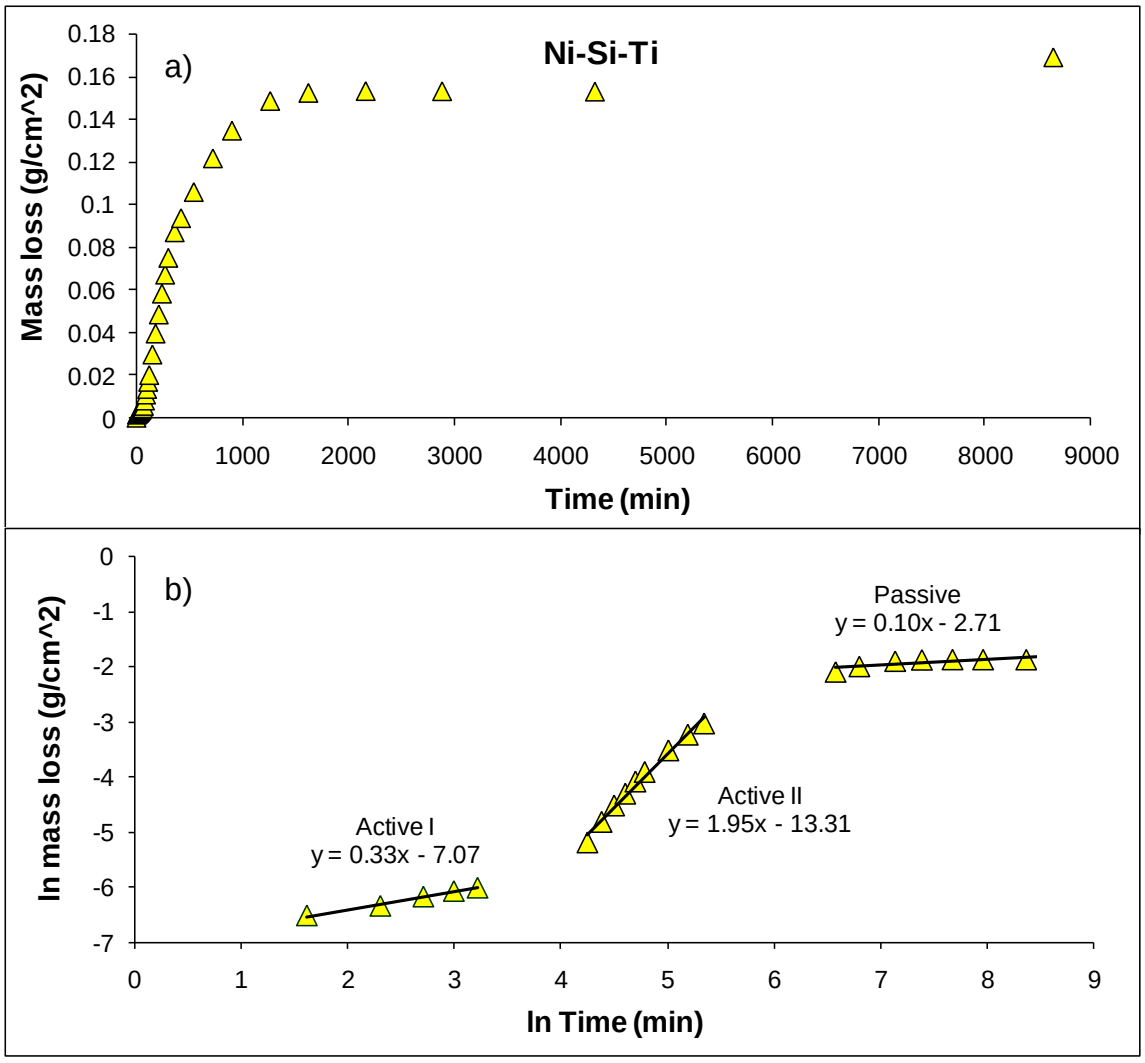

Figure 3.4 a) The mass loss of the Ni-Si-Ti alloy in boiling 70 wt. % sulfuric acid, and b) a logarithmic plot of the mass loss data shown in part a).

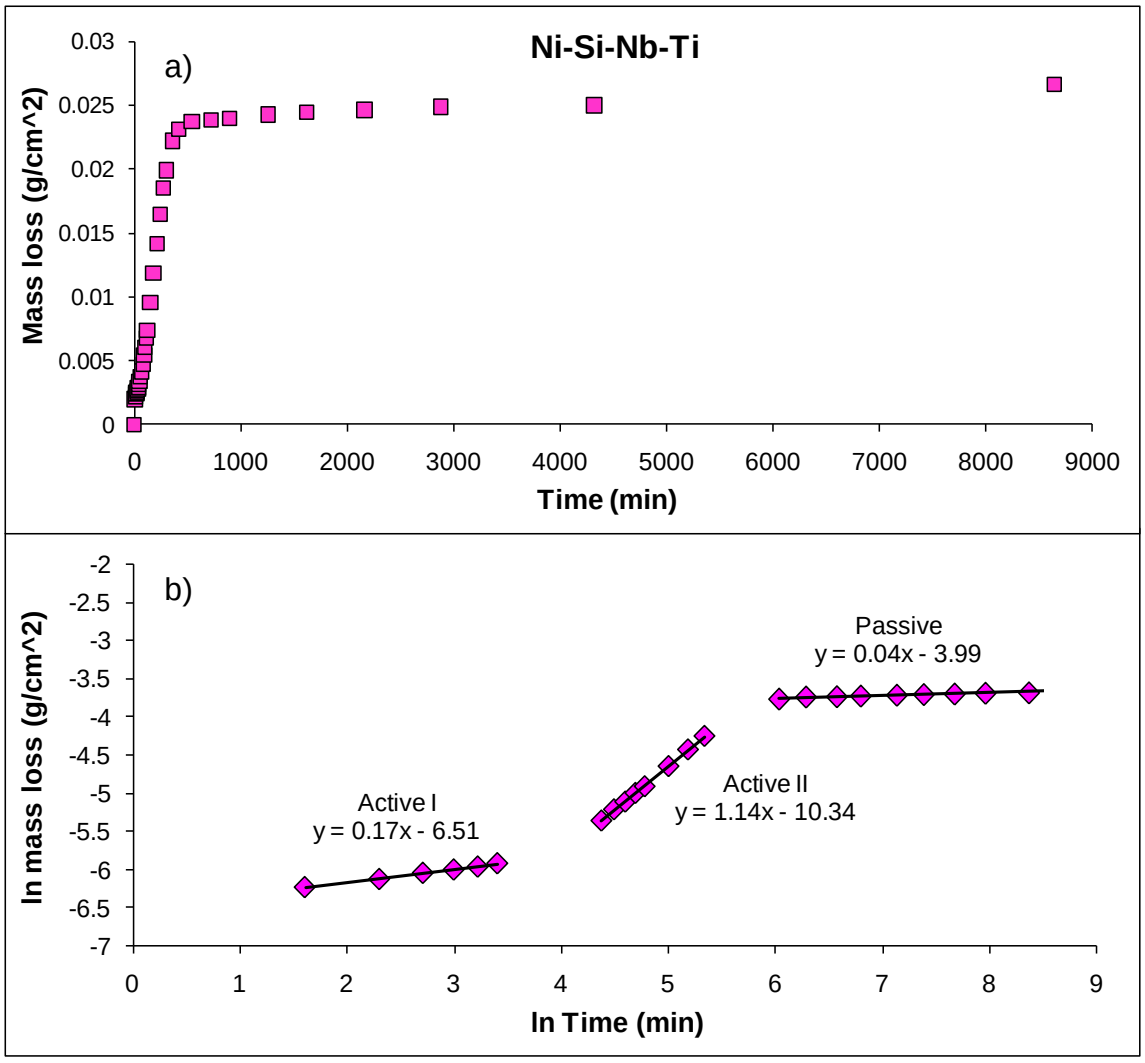

Figure 3.5 a) The mass loss of the Ni-Si-Nb-Ti alloy in boiling 70 wt. % sulfuric acid, and b) a logarithmic plot of the mass loss data shown in part a).

Figure 3.2 - Figure 3.5 can be summarized as follows:

- The base Ni-Si alloy exhibits one transition from active corrosion behavior to passive corrosion behavior between 120 and 150 minutes. This transition coincides with the single transition observed on the logarithmic plot of this data.
- The Ni-Si-Nb alloy exhibits a noticeable decrease in the weight loss rate between 110 and 150 minutes, however, it does not exhibit the full passivation that is observed for the other alloys. The logarithmic plot of this data shows no discernable transition.
- The Ni-Si-Ti alloy exhibits two transitions. The first transition occurs near 60 minutes and it separates two active corrosion regions. The second transition, which marks the onset of passivation, occurs between 1260 and 1620 minutes. Both of these transitions coincide with the transitions observed on the logarithmic plot of this data.
- The Ni-Si-Nb-Ti alloy exhibits two transitions. The first transition occurs near 60 minutes and it separates two active corrosion regions. The second transition marks the onset of passivation, which occurs between 420 and 540 minutes. Both of these transitions coincide with the transitions observed on the logarithmic plot of this data.

The corrosion rates of the four Ni_3Si alloys over the regions outlined in Figure 3.2 - Figure 3.5 are displayed in Table 3.1. They are given in units of mils per year (mpy) and were calculated using Equation 2.1. The amount of time taken for each alloy to passivate is also listed. Because the Ni-Si-Nb alloy did not exhibit full passivation, the corrosion rate calculated over the entire 6 day testing period is shown. The corrosion behavior of a Ni-Si-Nb alloy with rare earth alloying additions is presented in Appendix C.

Table 3.1 The corrosion rates in boiling 70 wt. % sulfuric acid.

Alloy	Corrosion Rate (mpy)			
	Active I	Active II	Passive	Time to Passivate (min)
Ni-Si	2138	-	9	120 – 150
Ni-Si-Nb	13*	-	-	**
Ni-Si-Ti	1287	7743	60	1260 – 1620
Ni-Si-Nb-Ti	732	1890	11	420 – 540

* Corrosion rate calculated over the entire 6 day period. See appendix B for comparison.
** This alloy did not exhibit full passivation.

3.1.2. Chemical analyses of corrosion test solutions. ICP MS experiments were performed on corrosion test solutions to determine the mass of dissolved metal ions resulting from corrosion. The results are given in Table 3.2. Mass losses are normalized to g/cm^2 and broken down by element. The total masses of each alloy element (i.e. Ni, Si, Nb, Ti) dissolved per unit area of alloy surface are given in the far right column.

Table 3.2 ICP MS results from sulfuric acid solutions following three and six days of corrosion testing.

Alloy	Days	Ni	Si	Nb	Ti	Total
		mg/cm^2	mg/cm^2	mg/cm^2	mg/cm^2	mg/cm^2
Ni-Si-Nb	3	16.42 ± 0.28	0	0.95 ± 0.01	-	17.37 ± 0.29
	6	23.71 ± 0.24	0	1.34 ± 0.01	-	25.05 ± 0.25
Ni-Si-Nb-Ti	3	19.87 ± 0.40	0	1.72 ± 0.01	0.21 ± 0.01	21.80 ± 0.42
	6	23.96 ± 0.14	0	1.97 ± 0.01	0.25 ± 0.01	26.18 ± 0.16
Ni-Si-Ti	3	137.87 ±2.34	0.12 ± 0.01	-	4.19 ± 0.02	142.18 ± 2.37
	6	203.69 ±1.43	0.22 ± 0.02	-	6.39 ± 0.03	210.30 ± 1.48

The Ni-Si-Ti alloy exhibits significantly greater alloy dissolution than the ternary Ni-Si-Nb and quaternary Ni-Si-Nb-Ti alloys (roughly 10 times greater than the Ni-Si-Nb

alloy, and 8 times greater than the Ni-Si-Nb-Ti alloy). This is consistent with the relative corrosion rates between these alloys (see Table 3.1). Comparison of the net ion mass in solution (Table 3.2) with the net weight losses of the alloys (Figure 3.1) indicates that the net weight loss is less than the mass of ions in solution. This is due to the incorporation of oxygen and sulfur onto the surface, as will be discussed in Chapter 4.

3.2. THE MORPHOLOGY AND MICROSTRUCTURE OF CORRODED ALLOY SURFACES

In the preceding section the corrosion behavior of four Ni_3Si alloy compositions in boiling 70 wt. % sulfuric acid were discussed. In this section the characterization of corroded Ni_3Si alloy surfaces is presented. Optical microscopy was used to determine the morphology of these surfaces following corrosion testing. Electron imaging was used to obtain 3-dimensional morphological and compositional profiles of alloy surfaces following sulfuric acid exposure. The lateral and depth distributions of elements comprising the corrosion films were identified using EDS mapping and SEM. Chemical compositions of alloy surfaces and chemical states of elements comprising these surfaces were probed using XPS.

3.2.1. The morphology of corroded surfaces. Figure 3.6 displays images of Ni_3Si alloys following three days of exposure to boiling 70 wt. % sulfuric acid. The photographs were captured with a 35 mm DSLR camera. The high magnification images displayed below these photographs were captured on an optical microscope. Each of the alloys has an obvious corrosion film, however there are noticeable differences in their appearances. The morphologies of these surfaces range from relatively smooth on Ni-Si-Nb, to very coarse and grainy on Ni-Si-Ti. Optical images reveal a semi-transparent film on the surface of the Ni-Si-Nb, whereas Ni-Si-Ti and Ni-Si-Nb-Ti surfaces are completely opaque. Both of the titanium containing alloys exhibit significant spalling (the Ni-Si-Ti alloy being the worst), whereas the film on the ternary Ni-Si-Nb alloy was adherent to the surface.

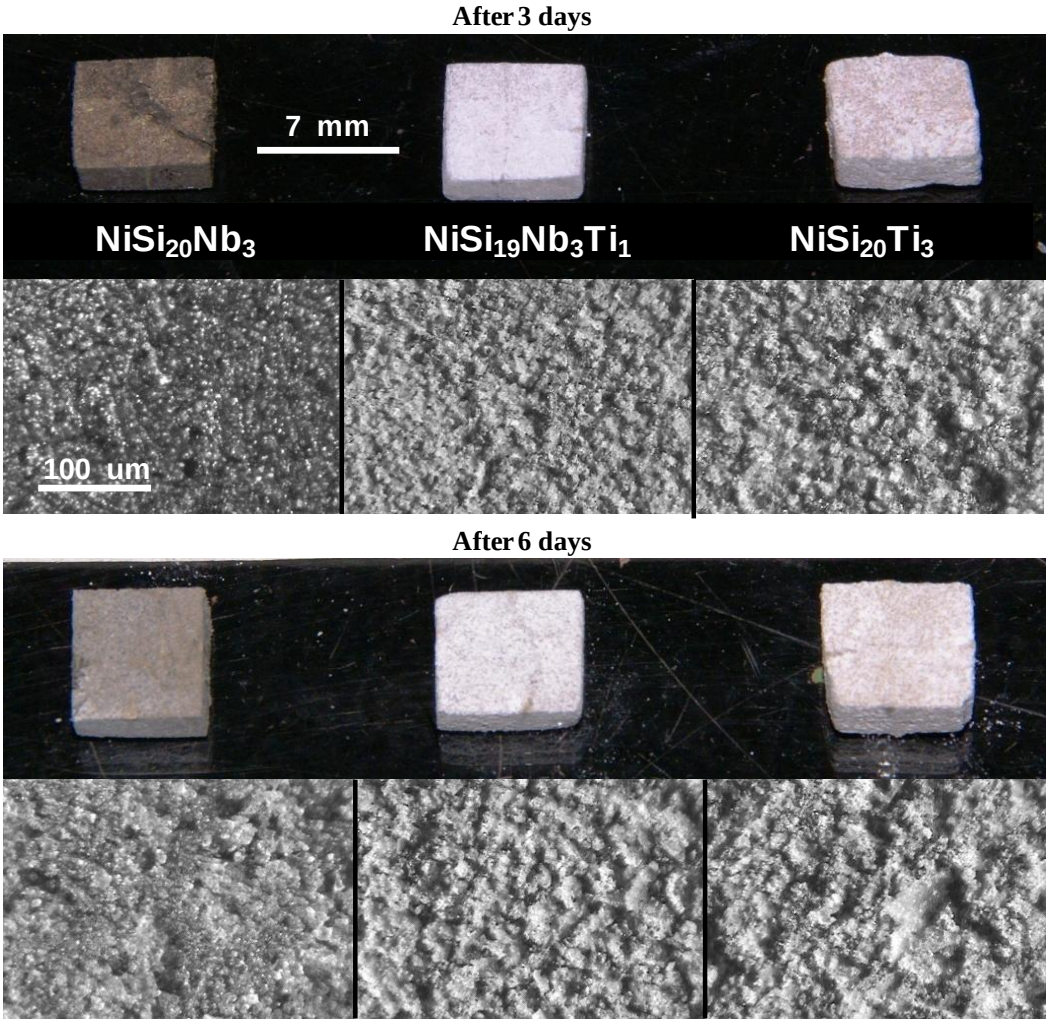

Figure 3.6 Optical images of Ni-Si-Nb, Ni-Si-Nb-Ti, and Ni-Si-Ti alloys following 3 days of exposure (top) and 6 days of exposure (bottom) to boiling 70 wt. % sulfuric acid.

3.2.2. The microstructures of uncorroded surfaces. The uncorroded microstructures of the four alloys listed in Table 2.1 are shown in Figure 3.7. They are comprised of the following phases (at. %):

α: Ni (FCC)

β_1: Ni_3Si

γ: $Ni_{31}Si_{12}$

G: $Ni_{55}Si_{24}Nb_{21}$

Figure 3.7 is summarized as follows: the binary Ni-Si microstructure is comprised of β_1, γ, α, and eutectic $\alpha + \beta_1$ phases. The ternary Ni-Si-Nb microstructure is comprised of β_1, γ, and G phases. The quaternary Ni-Si-Nb-Ti microstructure is comprised of β_1, G, and eutectic β_1 + G phases. The ternary Ni-Si-Ti microstructure is comprised of a single β_1 phase. Each of these phases is labeled.

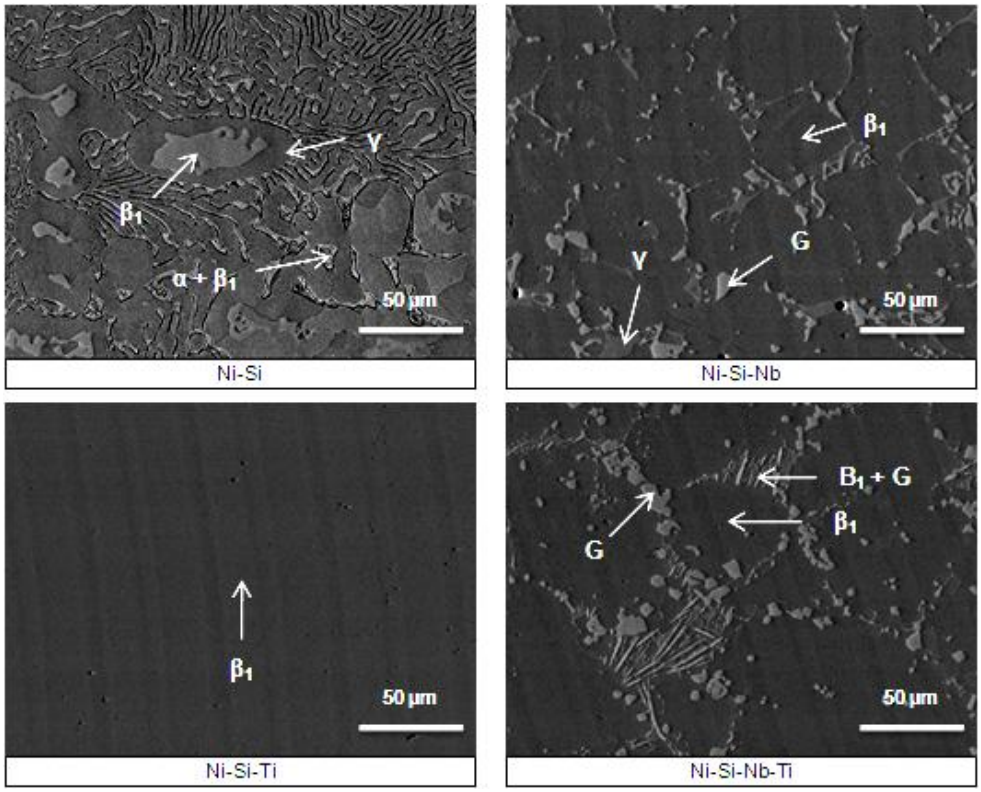

Figure 3.7 The microstructures of Ni-Si, Ni-Si-Nb, Ni-Si-Nb-Ti, and Ni-Si-Ti alloys.

3.2.3. The microstructures of corroded surfaces. Figure 3.8 shows a BSE image of a Ni-Si-Nb alloy surface that was exposed to boiling 70 wt. % sulfuric acid for one minute. The β_1, γ, and G phases are labeled in this image.

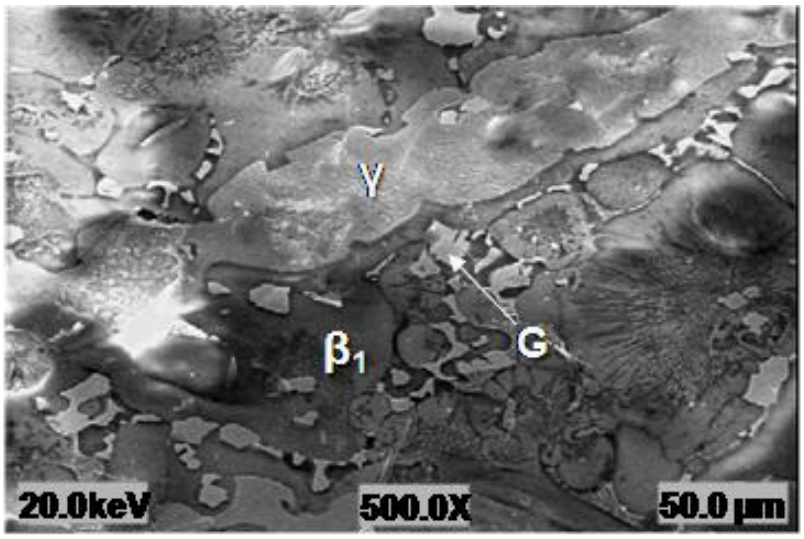

Figure 3.8 BSE image of a Ni-Si-Nb alloy surface exposed to boiling 70 wt. % sulfuric acid for one minute.

Figure 3.9 shows compositional depth profiles of the corroded β_1, γ, and G phases shown in Figure 3.8. Composition profiles were obtained by sputtering the surfaces with Ar ions and then analyzing them with an Auger nanoprobe. The Ar sputter gun was operated at a rate of 150 nm/min. The surface compositions on these phases appear to be SiO_2. This is evident by the ~ 1:2 silicon to oxygen ratio prior to sputtering. The oxides covering these phases do not have the same thickness. The β_1 phase contains an oxide that is roughly 300 nm thick. This is evident by the simultaneous decrease of silicon (Si^{4+}) and oxygen with the increase of nickel and elemental silicon that is observed with increasing sputtering time. The γ phase is covered by a ~ 150 nm thick SiO_2 layer. The G phase is covered by a ~ 30 nm thick oxide. Further Auger analysis of corroded Ni-Si-Nb, Ni-Si-Ti, and Ni-Si-Nb-Ti alloy surfaces can be found in Appendix D.

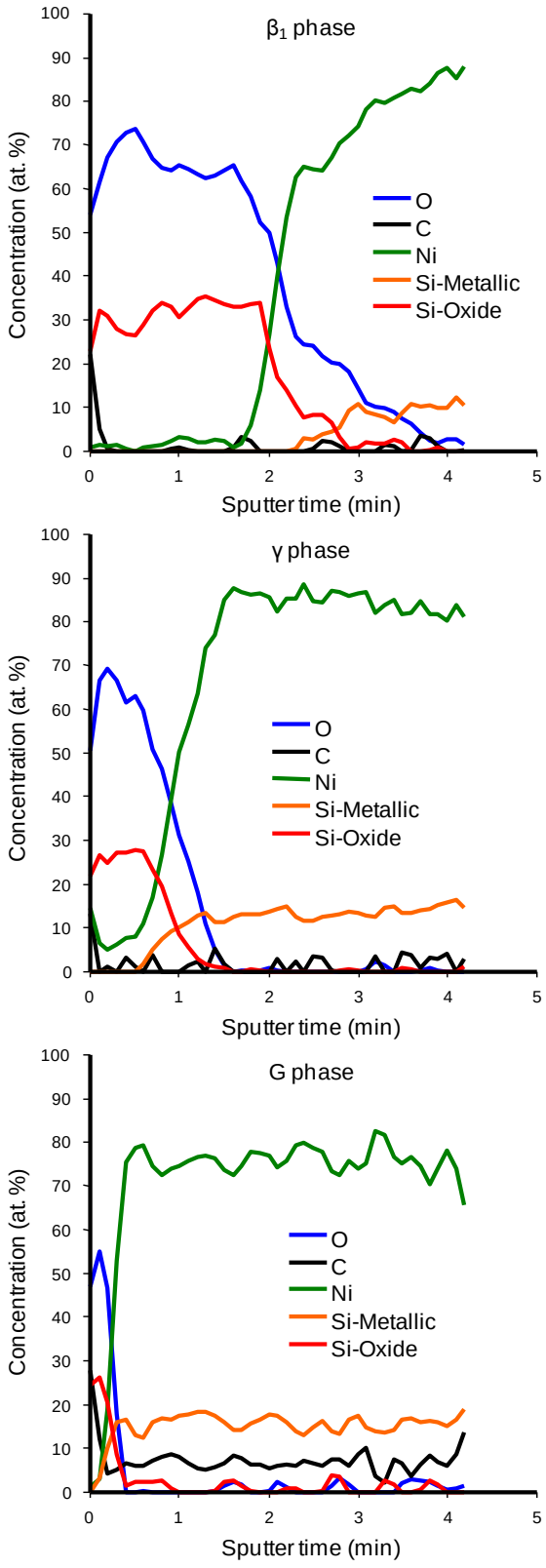

Figure 3.9 Compositional depth profiles of the corroded β_1, γ, and G phases shown in Figure 3.8. Compositions were obtained using scanning AES. The sputter rate was 150 nm/min.

Figure 3.10 - Figure 3.13 display BSE images of Ni-Si, Ni-Si-Nb, Ni-Si-Nb-Ti, and Ni-Si-Ti surfaces that were exposed to boiling 70 wt. % sulfuric acid for 10 minutes respectively. Figure 3.14 - Figure 3.17 show EDS composition maps of these respective surfaces.

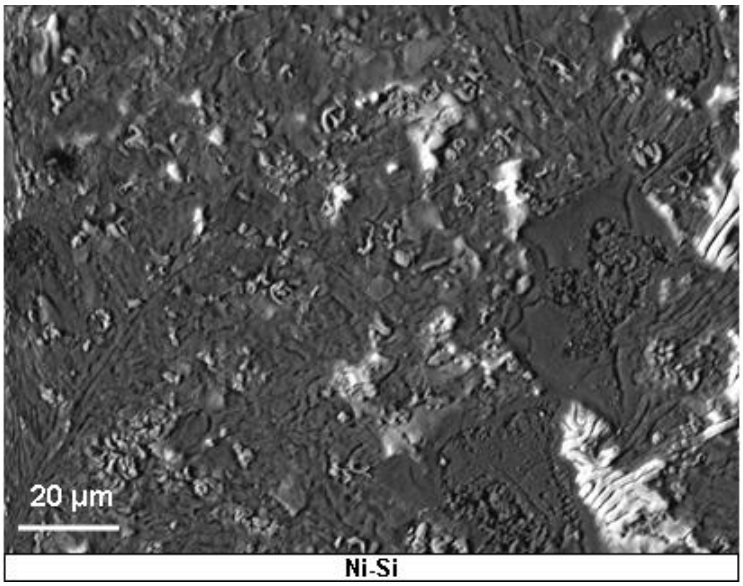

Figure 3.10 BSE image of a Ni-Si alloy surface exposed to boiling 70 wt. % sulfuric acid for 10 minutes.

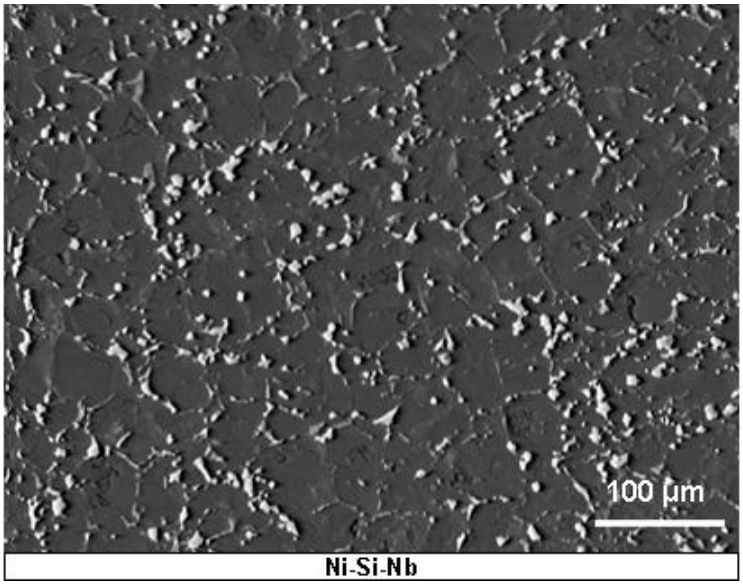

Figure 3.11 BSE image of a Ni-Si-Nb alloy surface exposed to boiling 70 wt. % sulfuric acid for 10 minutes.

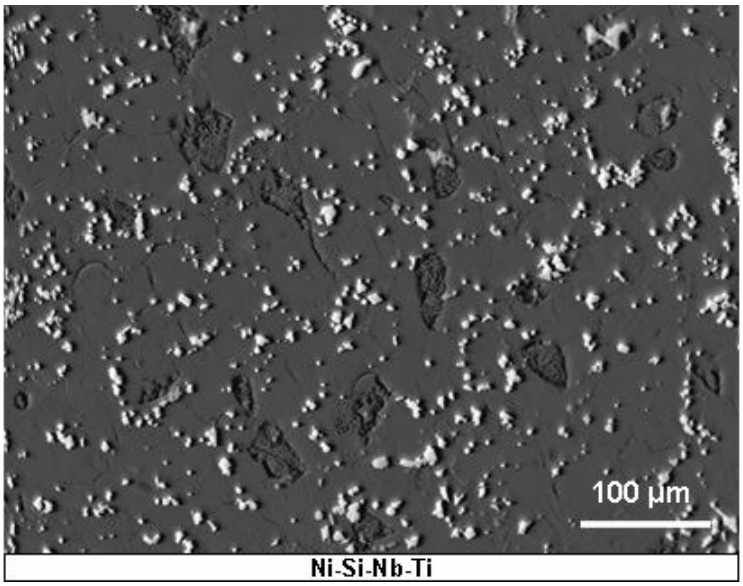

Figure 3.12 BSE image of a Ni-Si-Nb-Ti alloy surface exposed to boiling 70 wt. % sulfuric acid for 10 minutes.

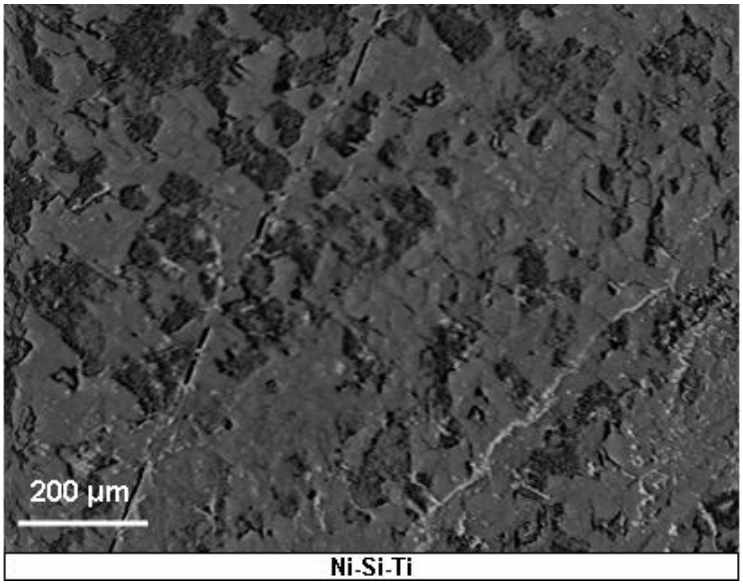

Figure 3.13 BSE image of a Ni-Si-Ti alloy surface exposed to boiling 70 wt. % sulfuric acid for 10 minutes.

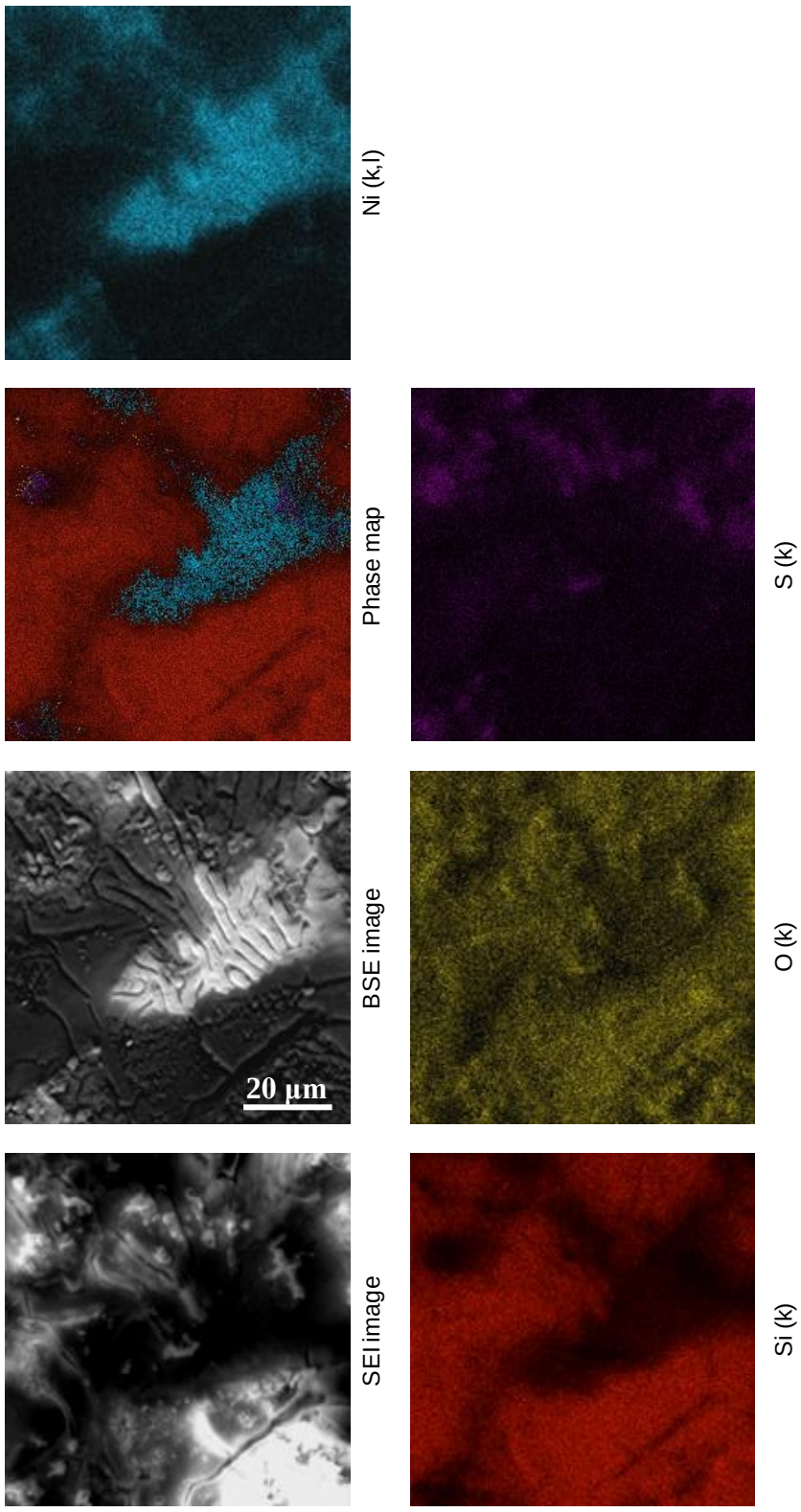

Figure 3.14 EDS map of a Ni-Si surface following 10 minutes of exposure to boiling 70 wt. % sulfuric acid.

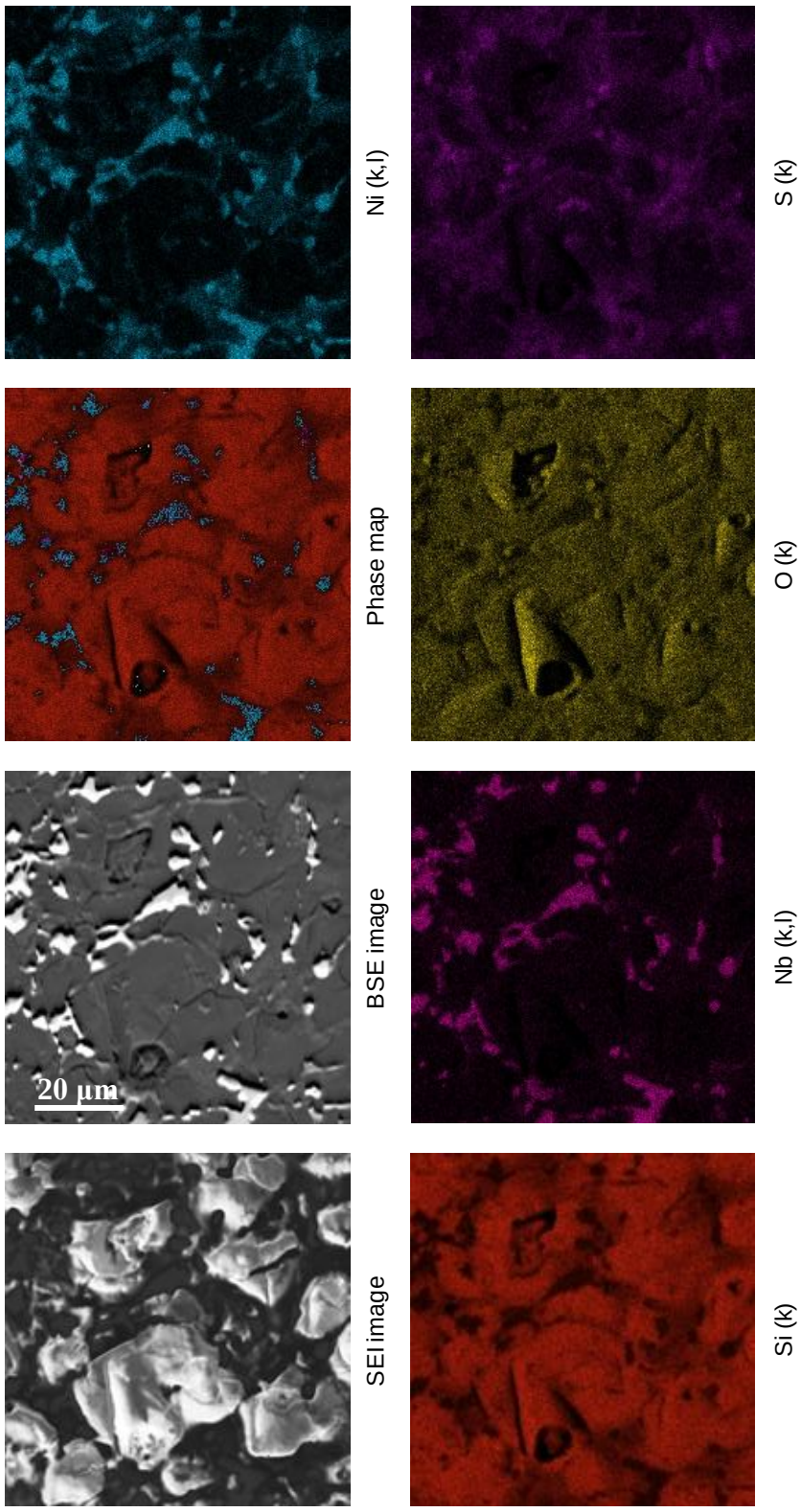

Figure 3.15 EDS map of a Ni-Si-Nb surface following 10 minutes of exposure to boiling 70 wt. % sulfuric acid.

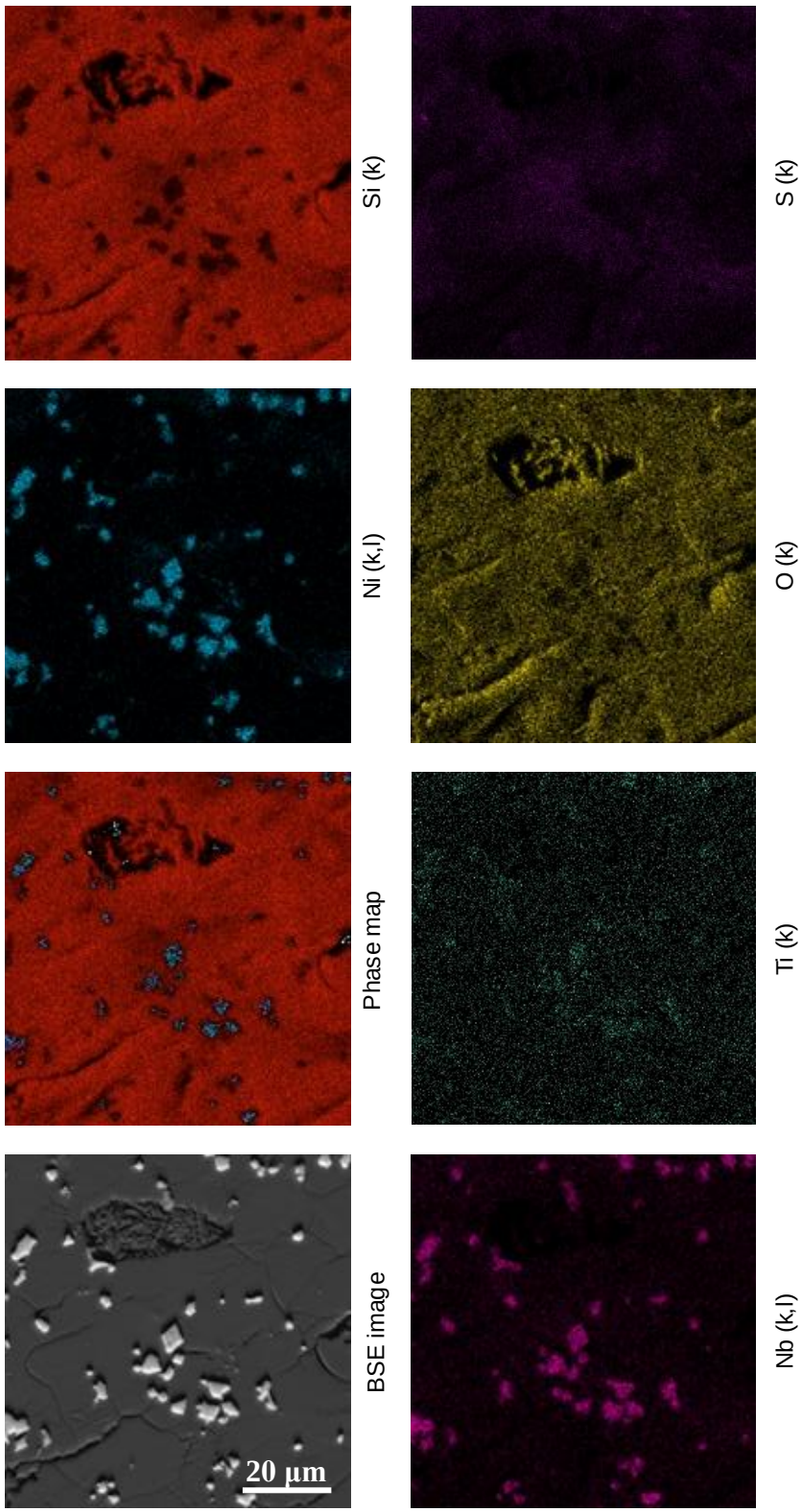

Figure 3.16 EDS map of a Ni-Si-Nb-Ti surface following 10 minutes of exposure to boiling 70 wt. % sulfuric acid.

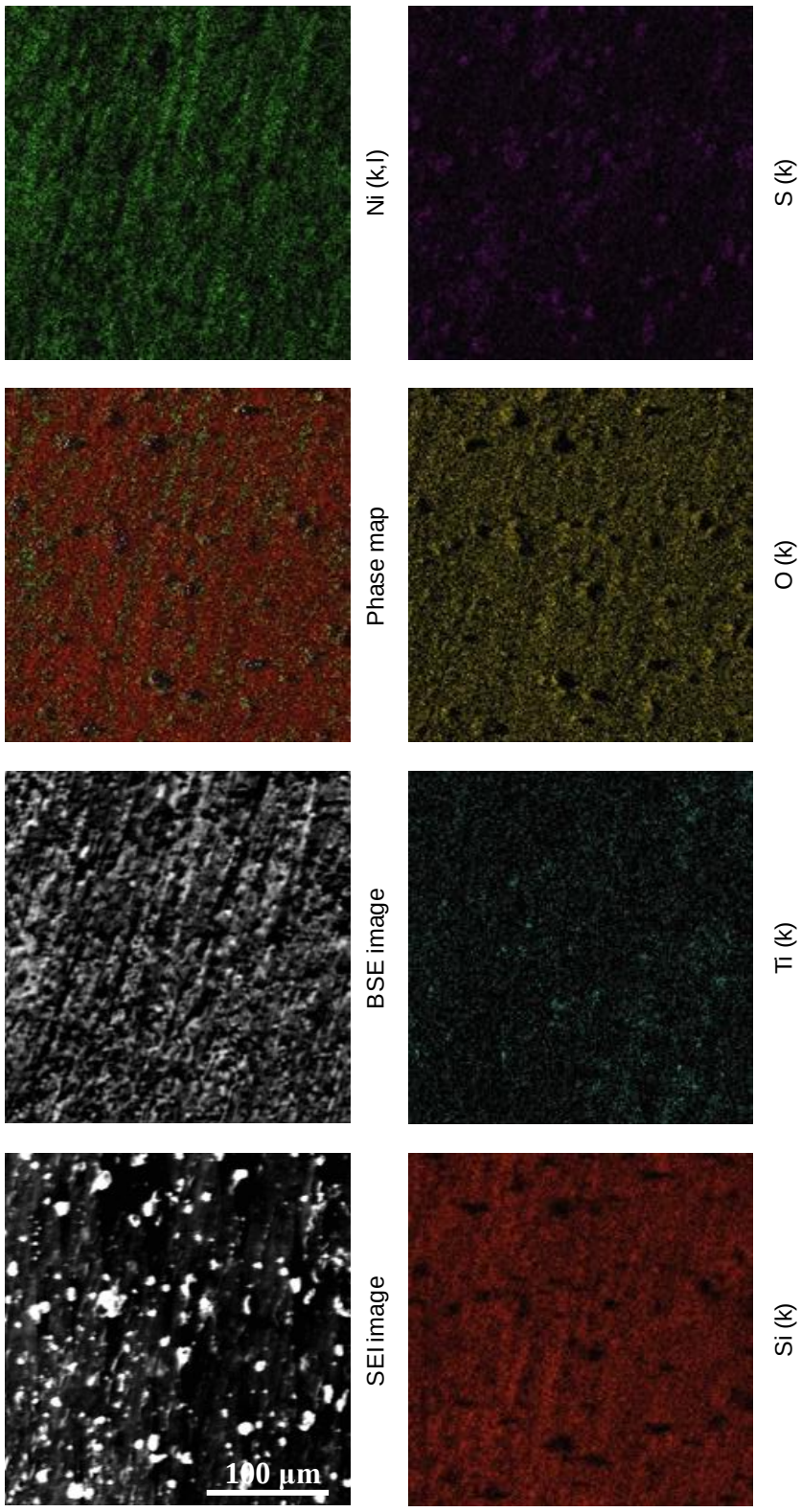

Figure 3.17 EDS map of a Ni-Si-Ti surface following 10 minutes of exposure to boiling 70 wt. % sulfuric acid.

There are several important observations regarding the morphologies and compositions of these corroded surfaces.

- Each of the alloy surfaces is rich in silicon and oxygen, whereas it is deficient in nickel, relative to its un-corroded surface.
- The Ni-Si alloy surface shows oxidation of the matrix β_1-phase, whereas there are certain regions (possibly individual phases) that appear to remain oxide-free.
- The Ni-Si-Nb alloy surface shows oxidation of the β_1-phase, whereas the G phase appears to be oxide-free.
- The Ni-Si-Nb-Ti alloy surface shows identical behavior to that of Ni-Si-Nb, but with a significant increase in the number of corrosion pit sites.
- The Ni-Si-Ti alloy surface shows uniform oxidation over its surface relative to the other alloys.

3.2.4. Film structure from XRD. X-ray diffraction performed on corroded alloy surfaces revealed differences in film structures for each alloy composition. Figure 3.18 - Figure 3.20 respectively show XRD plots data from Ni-Si-Nb, Ni-Si-Ti, and Ni-Si-Nb-Ti surfaces that were exposed to boiling 70 wt. % sulfuric acid for 6 days.
The XRD data reveal several important differences between these alloy surfaces with respect to film structure. They are summarized as follows:

- Amorphous SiO_2 is present on each of these surfaces. This is evidenced by the broad feature near 20 – 25 degrees.
- The corroded Ni-Si-Nb surface contains retgersite and nickel hexahydrite (both crystalline forms of $NiSO_46H_2O$), as well as quartz (crystalline SiO_2).
- The corroded Ni-Si-Ti surface contains metallic nickel and crystalline SiO_2.
- The corroded Ni-Si-Nb-Ti surface contains metallic nickel. A separate crystalline phase is present, but was not identified.
- The corroded Ni-Si-Nb surface exhibits a higher degree of crystallinity than Ni-Si-Ti and Ni-Si-Nb-Ti surfaces (based on the intensities of the sharp diffraction peaks).

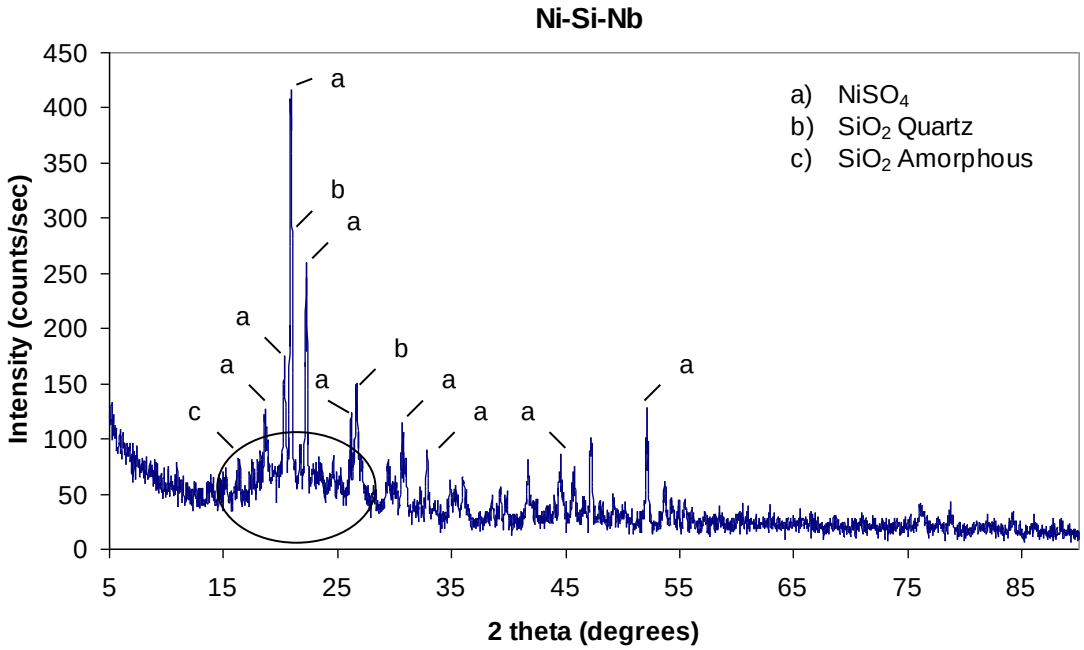

Figure 3.18 XRD pattern taken from a corroded Ni-Si-Nb alloy surface following exposure to boiling 70 wt. % sulfuric acid for 6 days.

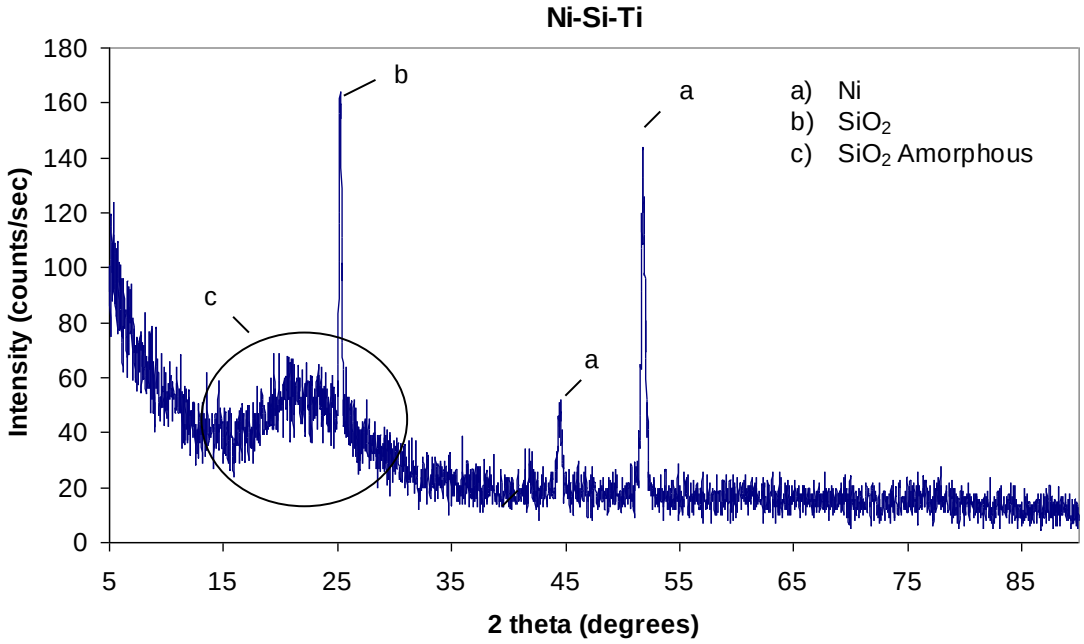

Figure 3.19 XRD pattern taken from a corroded Ni-Si-Ti alloy surface following exposure to boiling 70 wt. % sulfuric acid for 6 days.

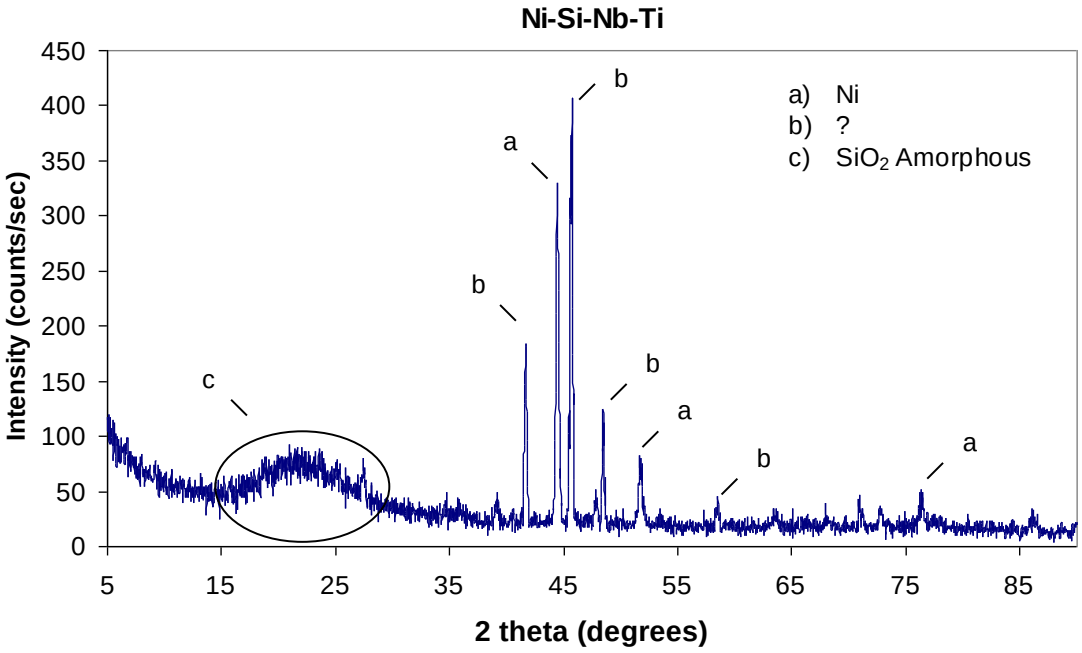

Figure 3.20 XRD pattern taken from a corroded Ni-Si-Nb-Ti alloy surface following exposure to boiling 70 wt. % sulfuric acid for 6 days.

3.2.5. Cross-section characterization of corrosion films. An EDS map taken from the cross section of a Ni-Si-Nb alloy that was exposed to boiling 70 wt. % sulfuric acid for three days is shown Figure 3.21 (page 40). There are four important observations that were made from this map.

- The film consists of silicon and oxygen.
- There is a depletion of nickel in the film relative to the underlying alloy.
- There is a depletion of niobium in the film relative to the underlying alloy.
- The film is 10 – 30 μm thick.

This cross-section is representative of all alloy compositions that were studied. There are not significant quantities of nickel, niobium, or titanium in the surface films. Table 3.3 lists the compositions of the phases labeled 'Alloy' and 'Oxide film' in Figure 3.21 that were obtained from standardless EDS analysis.

Table 3.3 Compositions of the 'Alloy' and 'Oxide film' regions that are labeled in Figure 3.21.

Phase	Composition obtained from standardless EDS analysis (at. %)*				
	Ni	Si	Nb	O	S
Alloy	79	19	2	0	0
Oxide film	4	34	2	57	3

*Atomic percent values given to within ± 10 %.

The composition of the 'Alloy' phase is consistent with the nominal composition of the Ni-Si-Nb alloy. The surface film however is enriched in silicon and oxygen relative to the nominal alloy composition. The strong overlap in the silicon and oxygen EDS maps indicates the presence of SiO_2.

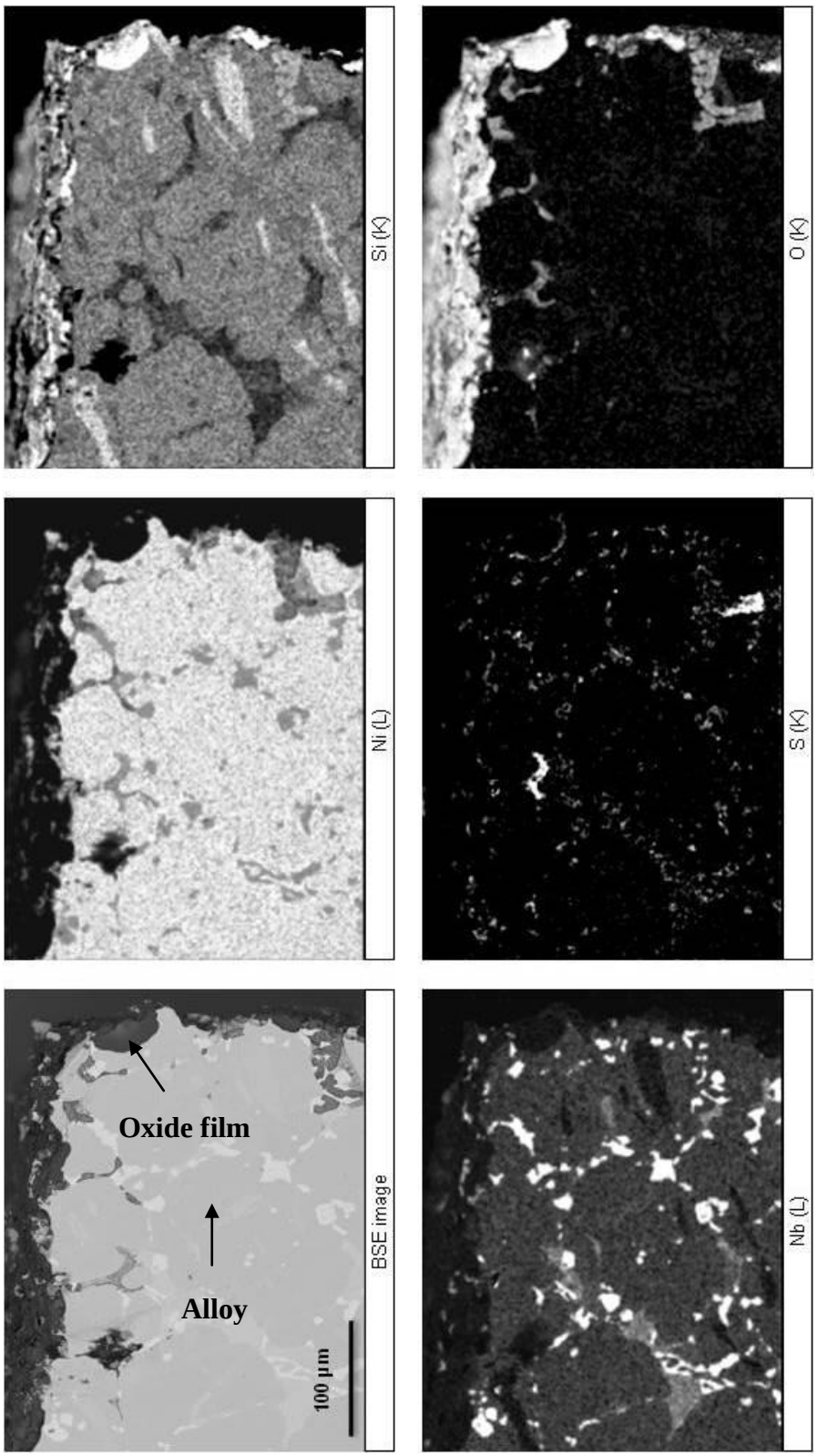

Figure 3.21 EDS map of the cross section of a Ni-Si-Nb alloy exposed to boiling 70 wt. % sulfuric acid for 3 days. This cross section is representative of alloy composition.

3.3. THE CHEMISTRY OF CORRODED ALLOY SURFACES

The analyses in this section describe the results of x-ray photoelectron spectroscopy experiments done on corroded Ni_3Si alloy surfaces. Low resolution survey scans were taken on alloy surfaces to determine the relative abundances of elements on each surface. This was done by fitting the photoelectron peaks with Gaussian functions, integrating them over a specified energy ranges, and comparing the areas of each function. The intensities of the Ni 2*p* and Nb 3*d* photoelectron spectra were calculated from both of their spin-orbit doublet features. The relationship between the intensity of a photoelectron peak emanating from atom X (I_x), and the atomic concentration of atom X (C_x), is given below in Equations 3.1.

$$C_x = \frac{I_x / S_x}{\sum_i I_i / S_i} \tag{3.1}$$

where S is the atomic sensitivity factor and is determined by the detection efficiency of the XPS instrument. Table 3.5 below lists the relative sensitivity factors of Ni 2*p*, Si 2*p*, Nb 3*d*, Ti 2*p*, O 1*s*, and S 2*p* photoelectrons used to quantify this data. For simplicity, each of the sensitivity factors is referenced to $S_{Ni\ 2p}$.

Table 3.4 X-ray photoelectron sensitivity factors used to calculate elemental concentrations.

Photoelectron	**Ni 2*p***	**Si 2*p***	**Nb 3*d***	**Ti 2*p***	**O 1*s***	**S 2*p***
Sensitivity factor (S)*	1.0	0.10	0.82	0.55	0.19	0.18
Sensitivity factor (S)**	1.0	0.13	0.76	0.59	0.23	0.25

* The atomic sensitivity factor for XPS spectra taken in the MRC at Missouri S&T
** The atomic sensitivity factor for XPS spectra taken in the HTML at ORNL

High resolution scans were taken in narrow energy ranges corresponding to Ni 2*p*, Si 2*p*, Nb 3*d*, Ti 2*p*, O 1*s*, S 2*p*, and C 1*s* photoelectron binding energies. These scans revealed binding energy shifts between photoelectrons emitted from metallic, oxide,

sulfate, and sulfide environments. Table 3.5 lists the binding energies taken from the literature to identify these features. In addition to calculating the atomic concentrations of elements using low resolution survey scans, the high resolution Si 2*p* photoelectron spectra were deconvoluted into their metallic and oxide components and the relative concentrations of Si^{0+} and Si^{4+} sites were found.

Table 3.5 Photoelectron binding energies taken from literature [20, 21].

Element	Environment	Binding energy of photoelectron (eV)				
		1*s*	$2p_{1/2}$	$2p_{3/2}$	$3d_{3/2}$	$3d_{5/2}$
Ni	Metal NiO $NiSO_4$		869.7 871.7	852.3 853.3 857		
Si	Metal SiO_2			99.3 103.4		
Nb	Metal NbO NbO_2 Nb_2O_5 NbS_2				205.0 205.9	202.2 203.5 205.5 207.5 207.5
Ti	Metal TiO_2		459.9 464.2	453.8 458.5		
O	Oxide	529-533				
S	SO_2 Sulfide Sulfate			167.8 161-163 168-170		
C	Hydrocarbon	284.6				

Figure 3.22 - Figure 3.25 show survey spectra taken from Ni-Si, Ni-Si-Nb, Ni-Si-Ti, and Ni-Si-Nb-Ti surfaces, respectively, following exposure to boiling 70 wt. % sulfuric acid. These spectra are color-coded according to the amount of time spent in solution. Binding energies were corrected according to the standard C 1*s* binding energy of 284.6 eV. The untreated, three, and six-day exposed surfaces were sputtered for 60 seconds at a rate of 100 nm/min to reduce the presence of adventitious carbon. Surfaces exposed for 30 minutes were lightly sputtered for only 30 seconds at a rate of 100 Å/min so as not to remove significant portions of the films. The one and 10 minute surfaces were not sputtered at all.

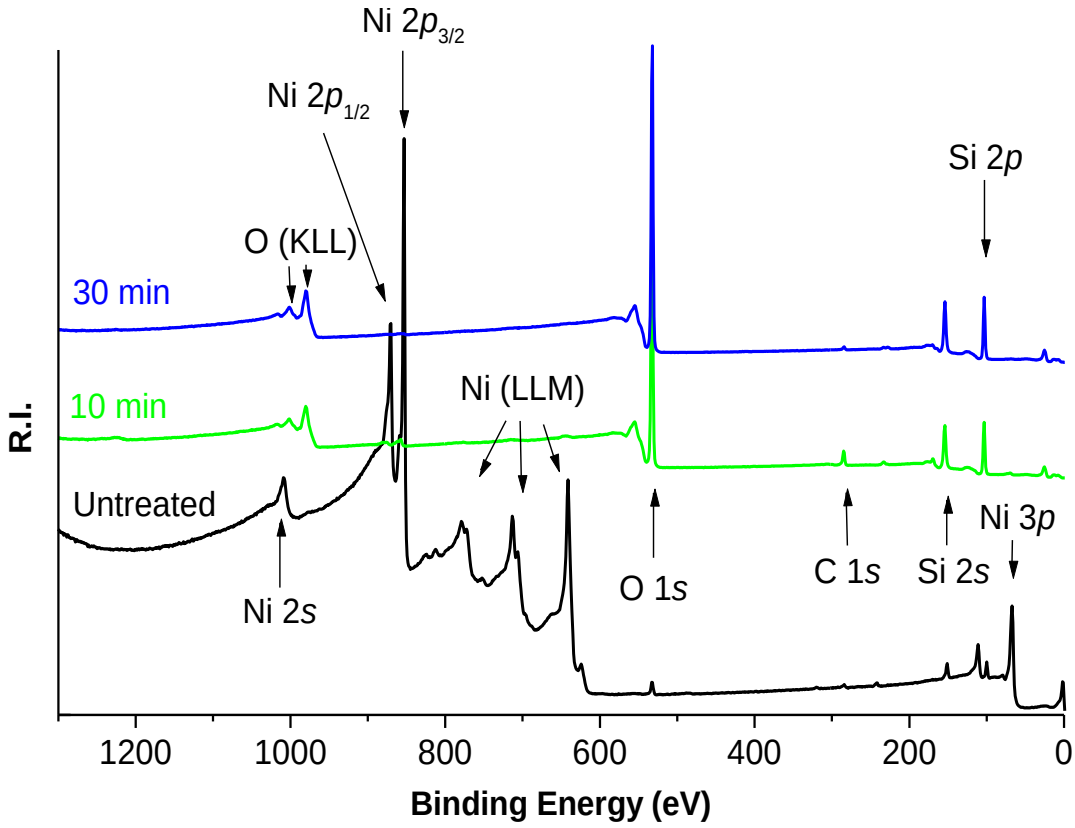

Figure 3.22 Low resolution x-ray photoelectron spectra taken on a Ni-Si alloy surfaces following exposure to boiling 70 wt. % sulfuric acid.

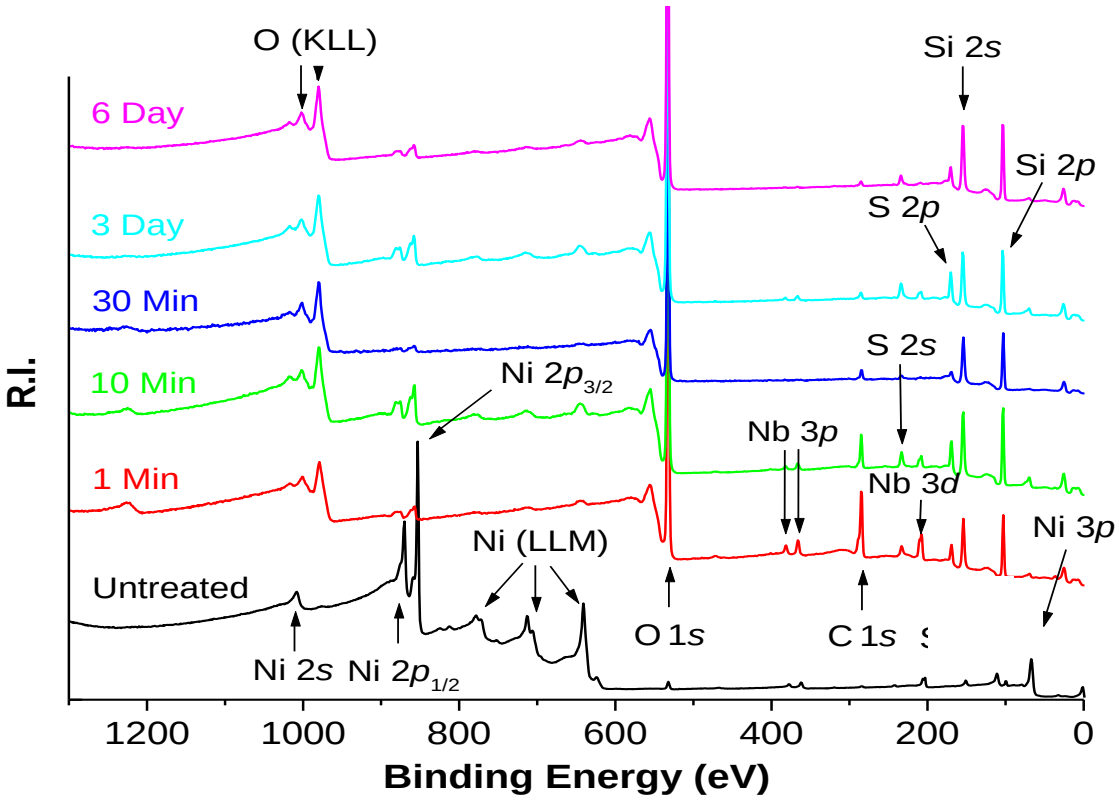

Figure 3.23 Low resolution x-ray photoelectron spectra taken on a Ni-Si-Nb alloy surface following exposure to boiling 70 wt. % sulfuric acid.

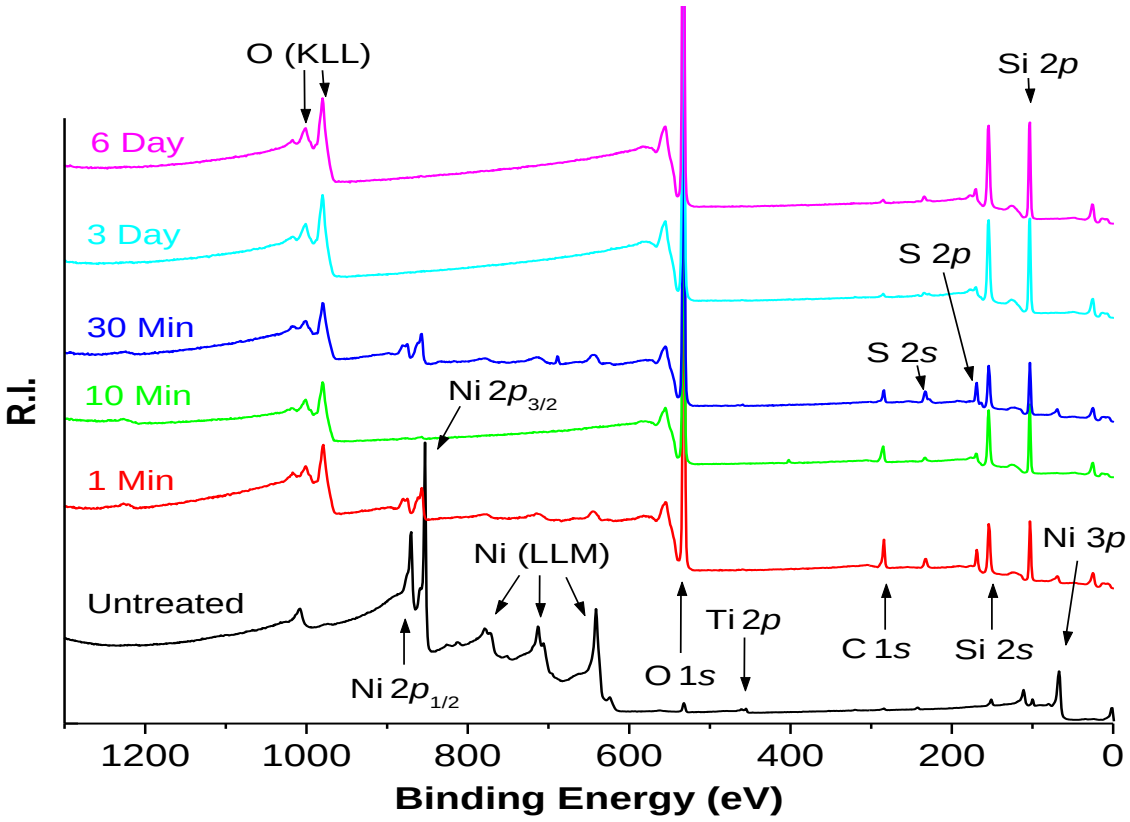

Figure 3.24 Low resolution x-ray photoelectron spectra taken on a Ni-Si-Ti alloy surface following exposure to boiling 70 wt. % sulfuric acid.

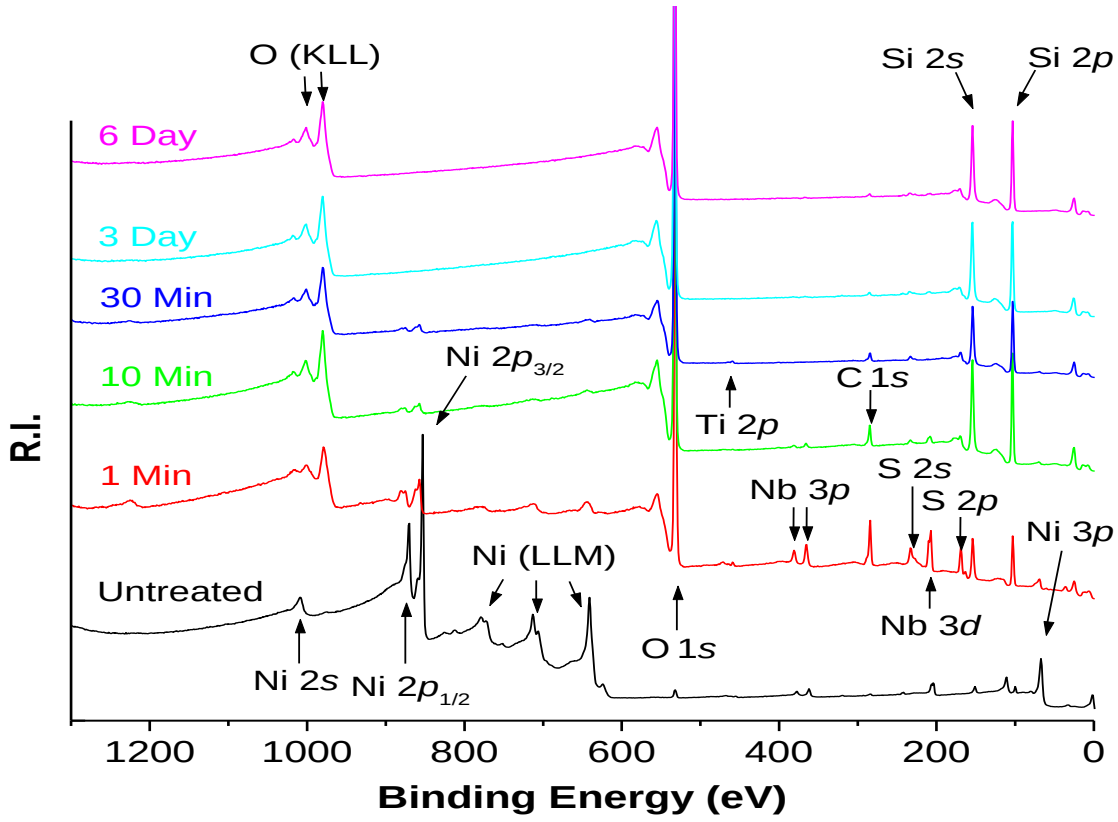

Figure 3.25 Low resolution x-ray photoelectron spectra taken on a Ni-Si-Nb-Ti alloy surface exposure to boiling 70 wt. % sulfuric acid.

Five important observations can be made from the low resolutions survey spectra shown in Figure 3.22 – Figure 3.25:

- The Ni 2*p* photoelectron intensity decreases significantly after one minute of exposure.
- The O 1*s* and Si 2*p* photoelectron intensities increase after one minute of exposure.
- The intensity of the Nb 3*d* photoelectron peak decreases with increasing time and is undetectable after 30 minutes of exposure.
- Only the uncorroded Ni-Si-Ti alloy has detectable amounts of titanium on its surface. Only Ni-Si-Nb showed detectable amounts of nickel on its surface after three and six days of exposure.

Based on these results it is clear that the reaction between these alloys with boiling 70 wt. % sulfuric acid produces a surface film that is rich in silicon and oxygen. The significant decrease of the Ni 2*p* photoelectron intensity suggests that the initial reaction involves significant nickel dissolution. The depletion of nickel from the outer layer following one minute in acid cannot be accounted for by silicon diffusion alone, considering that at 165 °C, metal ion diffusion is likely a rate limiting process.

High resolution Ni 2*p*, O 1*s* and S2*p*, Ni 2*p* and S 2*p* taken from a nickel sulfate species, Si 2*p*, Nb 3*d*, and Ti 2*p* x-ray photoelectron spectra are shown in Figure 3.26 - Figure 3.31 respectively. Each of the uncorroded alloy surfaces exhibit Ni $2p_{1/2}$ and $2p_{3/2}$ binding energies that are characteristic of metallic nickel (see Table 3.5). The Ni $2p_{3/2}$ binding energy from the corroded Ni-Si-Nb surface shows complete conversion from metallic nickel to nickel sulfate. Each of the other three alloy compositions shows partial conversion to nickel sulfate, along with some residual metallic nickel. Also, Ni-Si-Nb was the only alloy with nickel present on its surface after three and six days of corrosion testing.

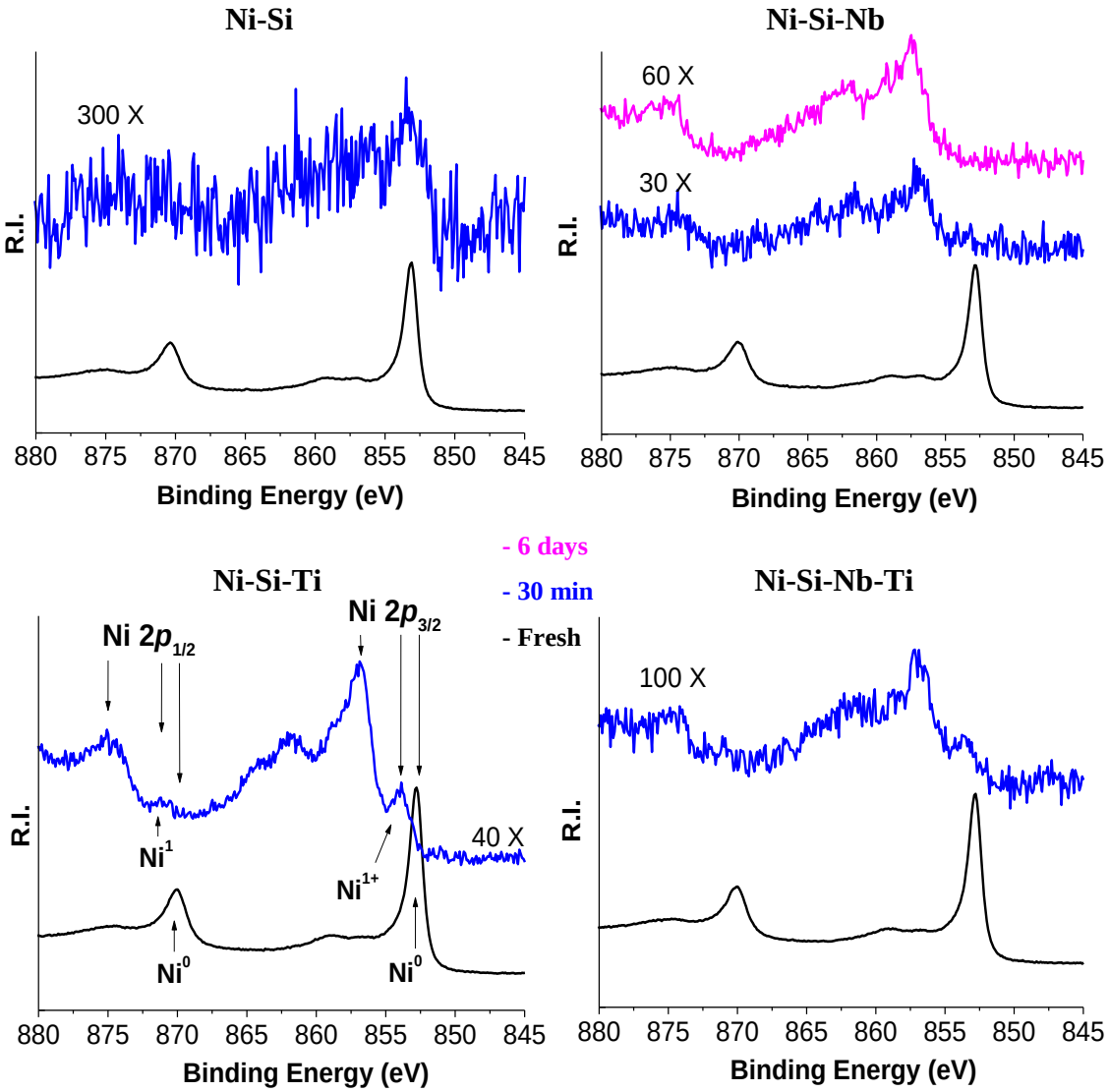

Figure 3.26 High resolution Ni 2*p* spectra of Ni_3Si alloy surfaces following exposure to boiling 70 wt. % sulfuric acid.

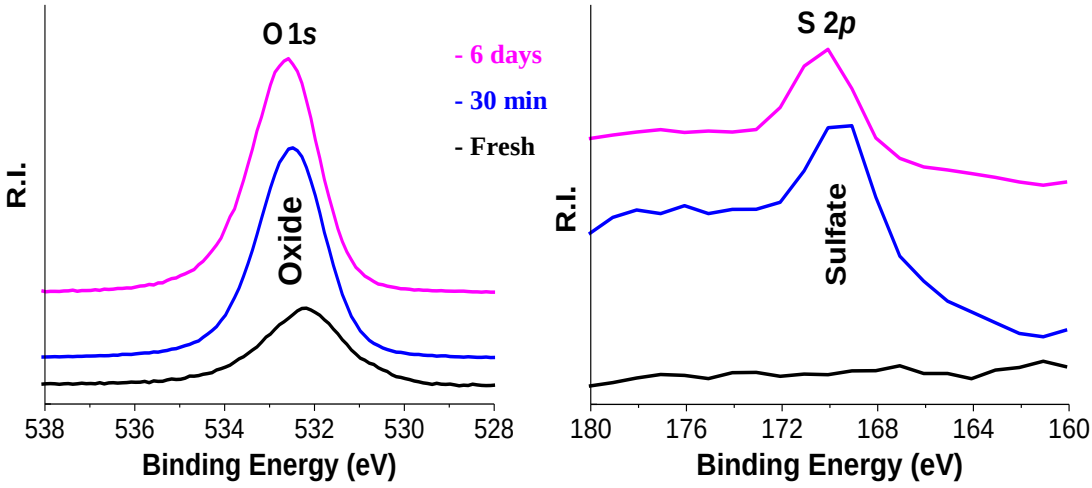

Figure 3.27 High resolution O 1*s* and S 2*p* XPS spectra taken from the Ni-Si-Nb alloy.

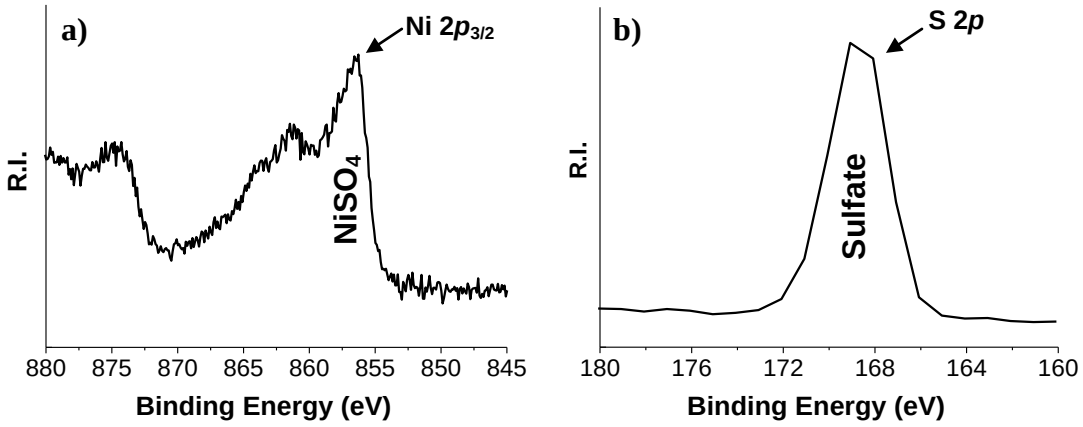

Figure 3.28 High resolution a) Ni 2*p* and b) S 2*p* photoelectron spectra of nickel sulfate.

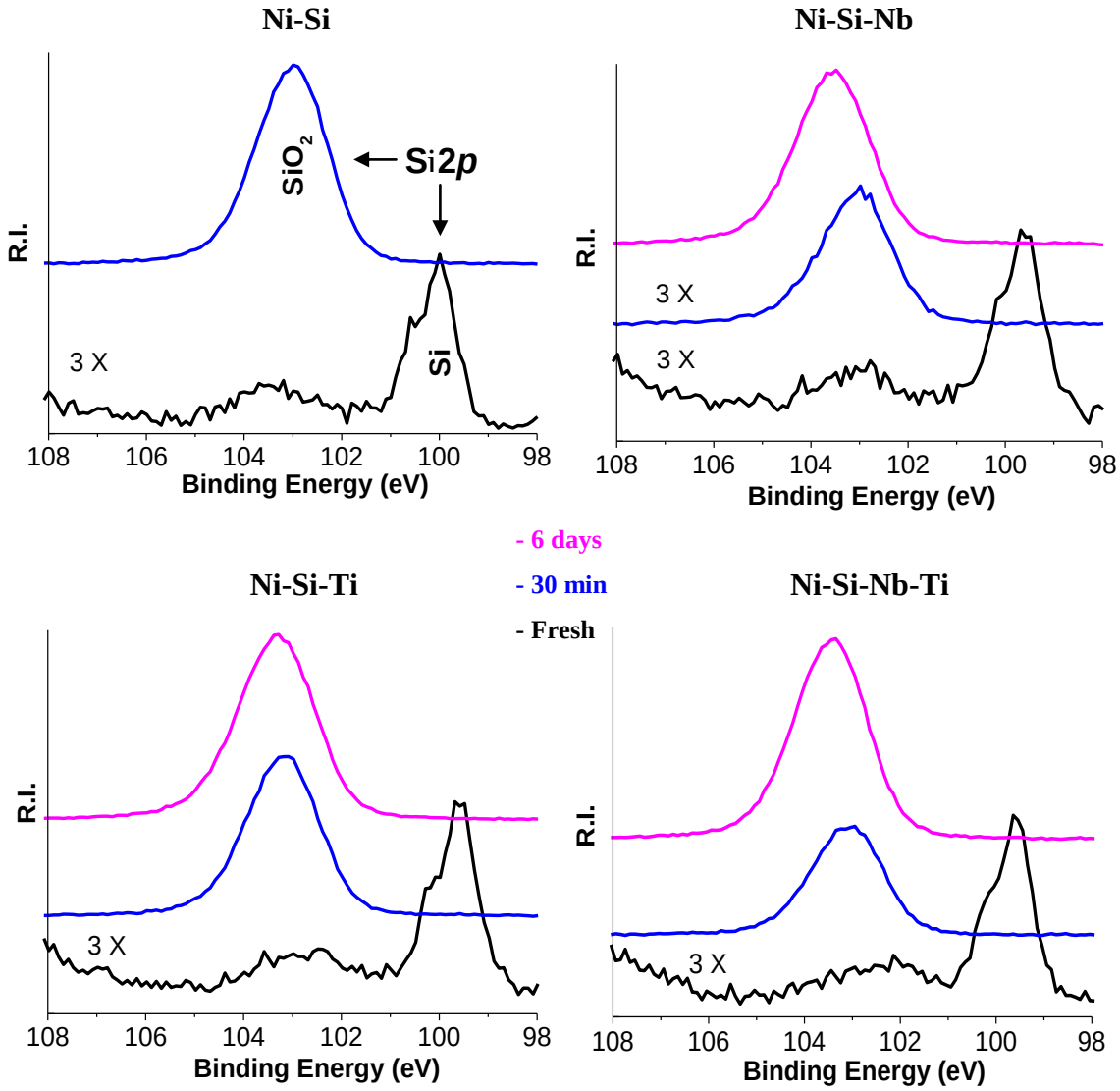

Figure 3.29 High resolution Si 2*p* spectra taken from Ni_3Si alloys following exposure to boiling 70 wt. % sulfuric acid

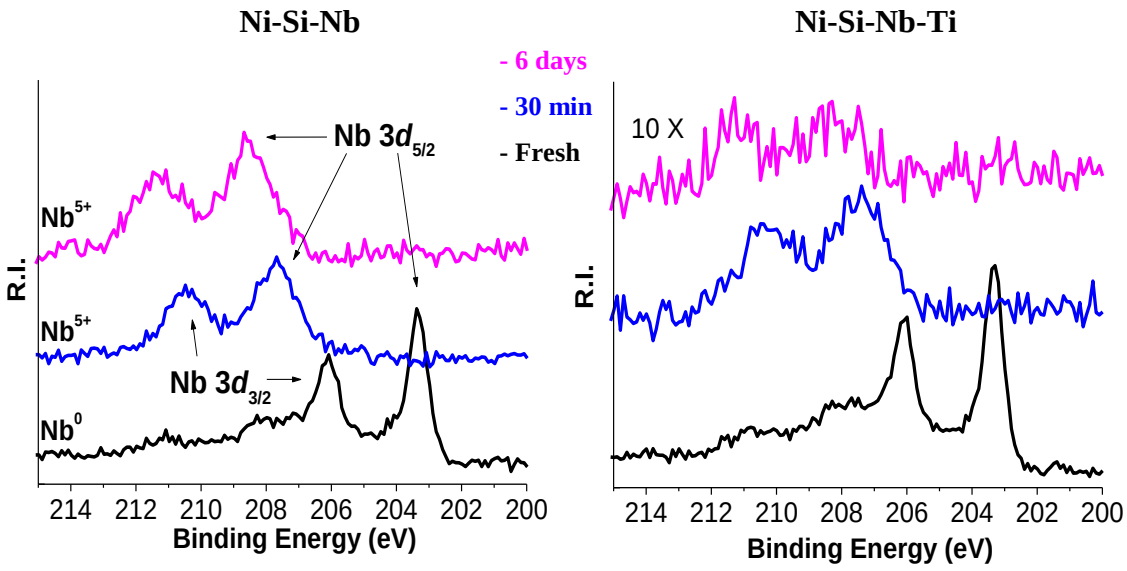

Figure 3.30 High resolution Nb 3*d* spectra taken from Ni_3Si alloys following exposure to boiling 70 wt. % sulfuric acid.

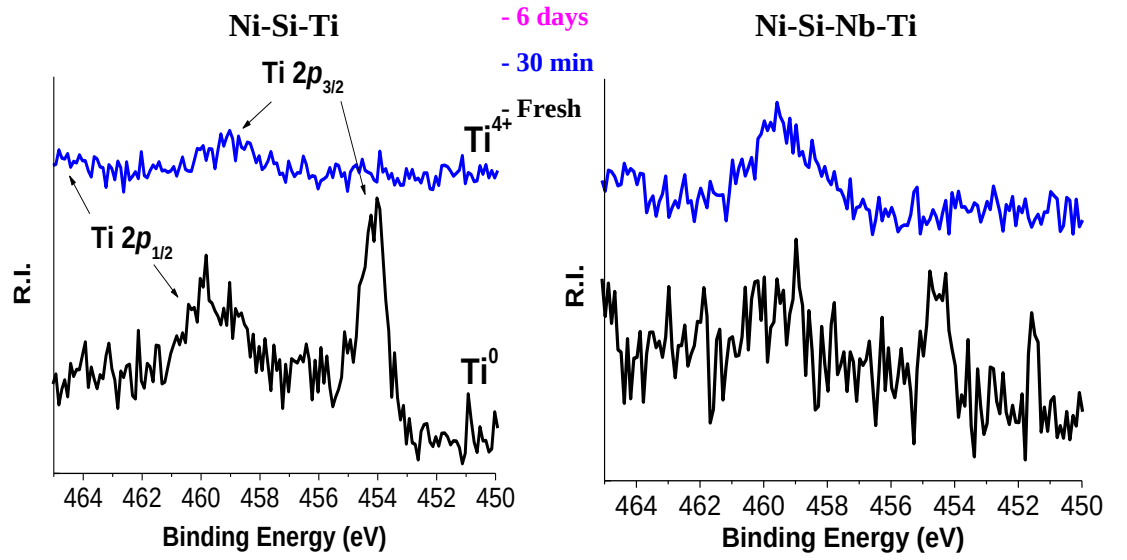

Figure 3.31 High resolution Ti 2*p* spectra taken from Ni_3Si alloys following exposure to boiling 70 wt. % sulfuric acid.

According to the Ni 2*p* and S 2*p* binding energies listed in Table 3.5, Figure 3.26 and Figure 3.27 indicate that nickel and sulfur atoms are bonded in a $NiSO_4$ environment. Smaller amounts of metallic nickel and in some cases nickel oxide are also detected on the corroded Ni-Si, Ni-Si-Ti, and Ni-Si-Nb-Ti surfaces, but not on the corroded surfaces of Ni-Si-Nb. High resolution O 1*s* and S 2*p* spectra taken from the Ni-Si-Nb alloy surfaces are representative of the O 1*s* and S 2*p* spectra taken from each of the surfaces studied. These spectra indicate the presence of oxides and sulfides. Comparison of the Ni 2*p* and S 2*p* spectra shown in Figure 3.26 andFigure 3.27 with the Ni 2*p* and S 2*p* spectra taken from a known nickel sulfate standard (Figure 3.28) confirms this.

Each of the uncorroded alloy surfaces exhibits Si 2*p* binding energies characteristic of metallic silicon (99.5 - 100 eV) with a small amount of SiO_2 (near 103.5 eV). After one minute of exposure the metallic Si 2*p* feature completely disappears, whereas the intensity of the Si^{4+} 2*p* feature increases significantly. These data clearly indicate that exposure of these surfaces to boiling 70 wt. % sulfuric acid cause the formation of SiO_2.

In addition to $NiSO_4$ and SiO_2, high resolution Nb 3*d* and Ti 2*p* photoelectron spectra indicate the presence of niobium and titanium oxides. Each of the uncorroded alloy surfaces exhibits Nb $3d_{5/2}$ photoelectron binding energies near 203.5 eV, which are characteristic of metallic niobium. After one minute of exposure the metallic Nb 3*d* feature completely disappears, whereas the intensity of the Nb^{5+} $3d_{5/2}$ feature near 207.5 eV increases significantly. This binding energy shift indicates a transition from metallic Nb to Nb_2O_5. Similarly, each of the corroded alloy surfaces exhibit Ti 2*p* binding energies that are characteristic of metallic titanium. After one minute of exposure, the Ti^0 $2p_{3/2}$ feature near 454.5 eV disappears, while the intensity of the Ti^{4+} $2p_{3/2}$ feature near 459 eV increased significantly.

Figure 3.32 summarizes the compositions of the four Ni_3Si alloy surfaces that were studied. The silicon concentrations listed for all exposed surfaces represent Si^{4+} sites, whereas silicon concentrations listed for unexposed surfaces represent Si^0 sites. Also, nickel concentrations were calculated from the metallic, nickel oxide, and nickel sulfate Ni 2*p* features. Following one minute of exposure, the outer surface undergoes a complete transformation from the base alloy to an SiO_2 film.

Each of the alloy surfaces exhibit very similar chemical compositions. With the exception of oxygen, the atomic concentrations of the uncorroded surfaces are representative of the alloy stoichiometry. After one minute of exposure, nickel contents decreased to roughly 2 at. %, whereas the oxygen and silicon contents increased to ~ 68 and between 25 and 30 at. %, respectively. The ~ 2:1 ratio of oxygen to silicon suggests that the corrosion film consists primarily of SiO_2. A slight decrease in the niobium concentration was observed following one minute of exposure, and after 30 minutes the Nb 3*d* peak was not detected. Also, non-trivial amounts of titanium were only observed on the uncorroded surface of Ni-Si-Ti. Boron was not detected on any of the surfaces

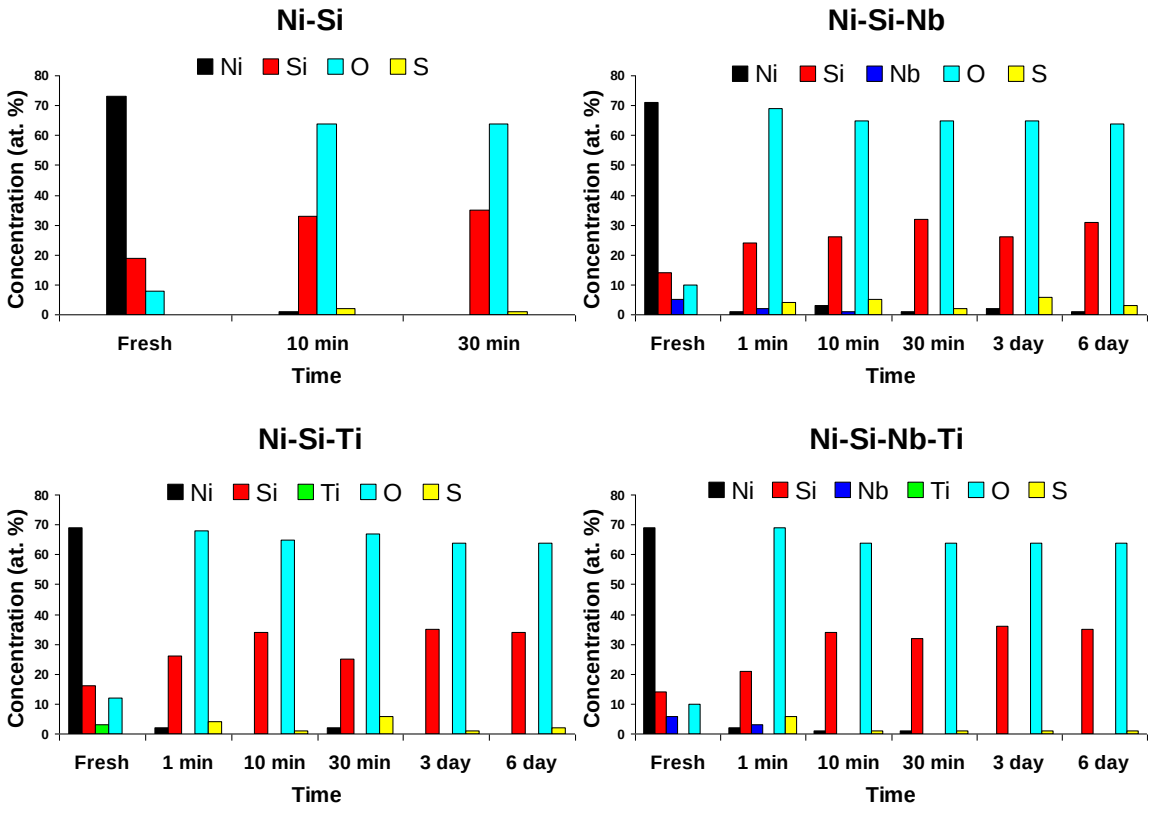

Figure 3.32 Concentrations of elements on Ni-Si, Ni-Si-Nb, Ni-Si-Ti, and Ni-Si-Nb-Ti surfaces following exposures to boiling 70 wt. % sulfuric acid.

4. DISCUSSION

4.1. CORROSION FILM ANALYSIS

Four Ni_3Si alloys were evaluated in boiling 70 wt. % sulfuric acid. The corrosion rates, surface compositions, and surface chemistries of these alloys are summarized below in Table 4.1.

Table 4.1 Corrosion rates and surface chemistries of alloys treated in 70 wt. % sulfuric acid.

Alloy	Corrosion Rate (mpy)			Surface composition (at. %)		Possible species (XPS)
	Active I	Active II	Passive			
Ni-Si	2138	-	9	Ni Si O S	0 35 64 1	- Si^{4+} Oxide Sulfate
Ni-Si-Nb	13	-	-	Ni Si Nb O S	2 26 0 65 6	$NiSO_4$ Si^{4+} - Oxide Sulfate
Ni-Si-Ti	1287	7743	158	Ni Si Ti O S	0 35 0 65 0	- Si^{4+} - Oxide -
Ni-Si-Nb-Ti	732	1890	11	Ni Si Nb Ti O S	0 35 0 0 64 1	- Si^{4+} - - Oxide Sulfate

It is evident that niobium and titanium have very different effects on the corrosion resistance of Ni_3Si in boiling 70 wt. % sulfuric acid. Compared to the Ni-Si alloy, the Ni-Si-Nb alloy has superior resistance, whereas each of the titanium containing alloys has

significantly less corrosion resistance. But while the corrosion behavior is sensitive to niobium and titanium contents in the alloy, there is strong evidence indicating that the chemistry and composition of the surfaces are very similar (see Table 4.1). The strong tendency of each Ni_3Si alloys to form an SiO_2 surface film is evident from the high resolution Si 2*p* photoelectron spectra shown in Figure 3.29. Fresh alloy surfaces contain primarily Si^0 photoelectrons with binding energies near 99.5 eV, whereas corroded alloy surfaces show Si^{4+} photoelectrons with binding energies near 103.5 eV. Furthermore, low resolution photoelectron spectra reveal that all of the alloy surfaces are comprised of silicon and oxygen in a ~ 1:2 ratio. Additionally, the cross section EDS map shown in Figure 3.21 provides further evidence of this. It is clear that the passivation of Ni_3Si alloys in 70 wt. % sulfuric acid is imparted by the formation of an inert SiO_2 barrier film, regardless of alloy composition. Nickel, niobium, sulfur, and titanium atoms are not present in significant quantities at the corroded surfaces (see Figure 3.32). Also, boron was not detected on any of the alloys surfaces studied (uncorroded and corroded). The high resolution Nb 3*d* and Ti 2*p* photoelectron spectra shown in Figure 3.30 and Figure 3.31 indicate that niobium and titanium exist as oxides, however, these atoms were not observed on alloy surfaces exposed for 30 minutes or more. The high resolution Ni 2*p* and S 2*p* photoelectron spectra shown in Figure 3.26 - Figure 3.28 indicate that nickel and sulfur atoms on the corroded surfaces are bonded primarily in a nickel sulfate environment. Small amounts of nickel oxide were also observed on the surfaces of the two titanium containing alloys. One important difference between the alloy compositions is the small amount of nickel on the Ni-Si-Nb alloy surface (< 2 at. %) following 3 and 6 days. Detectable quantities of nickel were not observed on either of the titanium containing alloy surfaces following 3 and 6 days. This observation is consistent with the x-ray diffraction pattern of the Ni-Si-Nb surface shown in Figure 3.18, which indicates the presence of nickel sulfate on this surface. Because nickel is the abundant element in the alloy (~ 77 at. %), it seems likely that an increase in the stability of nickel in the films would lead to enhanced corrosion resistance. This may be one of the reasons why the Ni-Si-Nb alloy has superior corrosion resistance in boiling 70 wt. % sulfuric acid.

Figure 3.7 - Figure 3.16 show the microstructures of uncorroded and corroded alloy surfaces. The presence of niobium-rich G phases on the surfaces of Ni-Si-Nb and

Ni-Si-Nb-Ti alloys appears to have an effect on the corrosion mechanism. EDS maps shown in Figure 3.14 - Figure 3.16 indicate that G phases and α-phases contain little oxygen after 10 minutes of exposure, whereas the matrix β_1 phase shows significant oxygen and silicon enrichment. This result possibly indicates that galvanic coupling between G/α phases with the β_1 phase is the mechanism controlling the corrosion of these alloys during initial exposure (i.e. prior to passivation). On the other hand, the Ni-Si-Ti alloy exhibits uniform attack over its surface (see Figure 3.12). Uniform corrosion and oxidation on this surface is understandable considering that this alloy has a single β_1-phase microstructure.

4.2. CORROSION KINETICS

Figure 3.2 - Figure 3.5 show logarithmic representations of the mass losses of Ni_3Si alloys in boiling 70 wt. % sulfuric acid. The time intervals over which the logarithmic weight loss curves exhibit linear behavior are separated and fit with linear functions. Reaction controlled corrosion mechanisms (i.e. nickel dissolution without the presence of a protective SiO_2 film) typically result in linear behavior of the form $\Delta W = kt$, where k is the rate constant and t is time. On the other hand, diffusion controlled corrosion mechanisms (e.g. diffusing ions through a SiO_2 barrier film) result in parabolic behavior of the form $\Delta W = kt^{1/2}$. Table 4.2 lists the n values of each linear region shown in Figure 3.2 - Figure **3.5**. n values range from 0.4 to 1.9.

Table 4.2 The slopes of the linear regions in Figure 3.2 - Figure 3.5

Alloy	**n values ($\Delta W = kt^n$)**		
	Active I	**Active II**	**Passive**
Ni-Si	0.66	-	0.04
Ni-Si-Nb	0.35	-	-
Ni-Si-Ti	0.33	1.95	0.10
Ni-Si-Nb-Ti	0.17	1.14	0.04

These Ni_3Si alloys do not strictly obey reaction controlled or diffusion controlled corrosion kinetics in boiling 70 wt. % sulfuric acid. For example, the behavior of the Ni-Si alloy in region one may be indicative of both diffusion controlled and reaction controlled corrosion mechanisms. The majority of the Ni-Si alloy surface after 10 minutes of exposure (see Figure 3.10 - Figure 3.14) appears to be covered with an oxide layer, however metallic phases are present in lower quantities (see bottom right portion of Figure 3.10 and the corresponding EDS map in Figure 3.14). Therefore, it seems likely that a reaction controlled corrosion mechanism is occurring over areas that are not covered with a film, whereas diffusion controlled mechanisms govern corrosion in the areas containing a film. Non-uniform oxidation over this surface might allow for both of these processes to occur simultaneously, and it would result in a power law of the form $\Delta W = kt^n$ with $0.5 \leq n \leq 1.0$ (the n value in the active region for Ni-Si is 0.66). This behavior makes qualitative sense considering that the two rate laws governing these corrosion mechanisms have n values of 0.5 and 1. Ni-Si-Ti and Ni-Si-Nb-Ti alloys exhibit behavior in region one that cannot be explained with simple reaction controlled and diffusion controlled corrosion mechanisms.

The transition between regions one and three of the Ni-Si and Ni-Si-Nb alloys are similar (these alloys do not exhibit an intermediate corrosion behavior). The decrease in the slope in region three marks the onset of passivation on these surfaces. Ni-Si-Ti and Ni-Si-Nb-Ti alloys exhibit an intermediate region over which there is a significant increase in slope. This intermediate region is followed by a third region which resembles the third regions of the Ni-Si and Ni-Si-Nb alloys. The presence of the intermediate region on each of the two titanium containing alloys may be indicative of cyclic corrosion in which portions of the film spall and then re-form. Spallation and re-passivation of these surfaces would indicate that titanium has detrimental effects on the chemical and/or mechanical stability of the film in this environment. However, there is no evidence that titanium is present in these films, and therefore it would be presumptuous to assume that titanium has detrimental effects on the film stability.

4.3. A MODEL FOR CORROSION AND PASSIVE FILM FORMATION

There are several pieces of information presented in Chapter 3 which provide clues to the mechanism of corrosion and film growth on Ni_3Si alloys in boiling 70 wt. % sulfuric acid. First is the preferential dissolution of nickel, niobium, and titanium relative to silicon. Chemical analyses of test solutions reveal that nickel is dissolved in the amount of ~ 95 at. % relative to the other alloy elements (i.e. Si, Nb, and Ti). Niobium and titanium concentrations are consistent with their concentration in the alloys. Silicon on the other hand is not detected in significant quantities in these solutions. Si^{4+} species were detected by XPS on all of these surfaces, and EDS maps of film cross-sections corroborated these findings. Based on this evidence it is likely that the passivation of these alloys is due to the rapid dissolution of nickel and subsequent formation of a protective SiO_2 barrier film. One approach to model the film growth on these alloys is to assume that all silicon atoms which disassociate from Ni_3Si sites during nickel dissolution subsequently react to form SiO_2. The mass of silicon (M_{Si}) that is involved in this process can be calculated using Equation 4.1 and from the mass of nickel (M_{Ni}) observed in the corrosion test solutions (Table 3.2).

$$M_{Si} = A_{Si/Ni} K M_{Ni} \tag{4.1}$$

where K is the weight ratio of one silicon atom to one nickel atom (K = 0.478), and $A_{Si/Ni}$ is the atomic ratio of silicon to nickel in the material. It is assumed that $A_{Si/Ni}$ has a value of 1/3, since it is believed that the β_1 phase is the primary constituent in the microstructure being oxidized. The mass of silicon resulting from this process can be used to calculate the mass of the resulting SiO_2 barrier film (Equation 4.2).

$$M_{SiO2} = M_{Si}(1+2K') \tag{4.2}$$

where K' is the weight ratio of one oxygen atom to one silicon atom (K' = 0.5695), and the factor of two reflects the atomic ratio of oxygen to silicon in SiO_2. An estimate of the film thickness can be made by assuming that the film density is equal to that of SiO_2.

The XRD patterns in Figure 3.18 - Figure 3.20 indicate that the film structure contains both quartz (ρ = 2.65 g/cc) and silica (ρ = 2.22 g/cc). The range of film thicknesses given in Table 4.3 were calculated assuming that the density of the film falls in between the density of silica and quartz.

Table 4.3 Film thickness calculation using ICP MS results shown in Table 3.2.

Alloy	Days	Mass of dissolved ions (g/cm^2)	Msi (g/cm^2)	M_O (g/cm^2)	M_{SiO2} (g/cm^2)	Film thickness (µm)
Ni-Si-Nb	3	0.01737	0.00277	0.00316	0.00593	22 - 27
	6	0.02505	0.00400	0.00455	0.00855	32 - 39
Ni-Si-Nb-Ti	3	0.0218	0.00348	0.00396	0.00744	28 - 34
	6	0.02618	0.00418	0.00476	0.00893	34 - 41
Ni-Si-Ti	3	0.14218	0.02268	0.02584	0.04852	183 - 221
	6	0.21018	0.03352	0.03820	0.07172	271 - 326

Collectively, this information provides a basic picture of the passive film formation on these surfaces. A simple model for the corrosion and film growth is as follows (Figure 4.1 illustrates this corrosion process):

- During initial sulfuric acid exposure nickel is dissolved rapidly, resulting in a porous, silicon-rich surface.
- Active dissolution of nickel continues while the silicon-rich outer layers begin to oxidize to form SiO_2. Nickel dissolution starts to slow as the SiO_2 phases begin coalescing to form a continuous film.

- Eventually enough SiO_2 is formed so that the mechanism of corrosion switches from bulk dissolution of nickel via a reaction controlled mechanism, to the transport of mass/vacancies across the silica film.

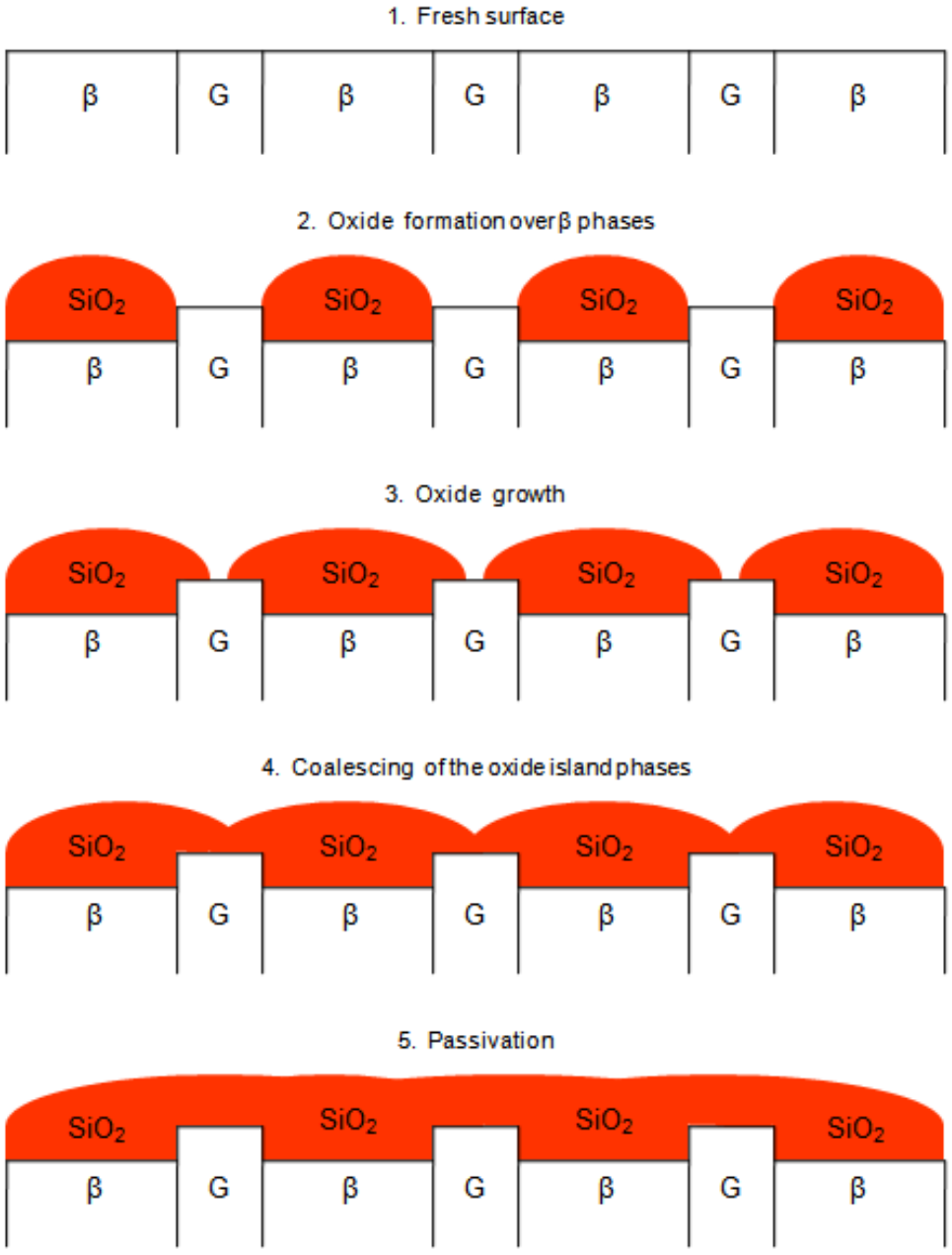

Figure 4.1 The corrosion process of Ni_3Si alloys in boiling 70 wt. % sulfuric acid.

5. CONCLUSIONS

The corrosion behavior of four Ni_3Si based intermetallic alloys in boiling 70 wt. % sulfuric acid has been evaluated. Corrosion films were analyzed to better understand the passivation mechanism of these alloys in this environment. Weight loss measurements provided information regarding the corrosion kinetics. X-ray photoelectron spectroscopy experiments were performed to determine the surface compositions and chemistries of the films. Scanning electron microscopy and energy dispersive spectroscopy experiments were performed to provide a three dimensional characterization of these films. Inductively coupled plasma mass spectrometry was performed on corrosion test solutions to measure the amount of alloy elements dissolved into solution. The conclusions drawn from these analyses are summarized below.

1. Ni-Si, Ni-Si-Nb, and Ni-Si-Nb-Ti alloys exhibit good corrosion resistance (~ 10 mpy following passivation) to boiling 70 wt. % sulfuric acid.
2. The passivation of Ni_3Si alloys in boiling 70 wt. % sulfuric acid is imparted by a SiO_2 barrier film that forms as a corrosion product. The rapid dissolution of nickel during the initial stages of corrosion results in a silicon-rich surface that subsequently reacts to form silicon oxides that provide a barrier to further corrosion. Chemical and elemental analysis of these surfaces has confirmed that the stable corrosion product is SiO_2.
3. Sulfur was detected in small quantities within these films. XRD and XPS data suggest that nickel sulfate is the probable chemical environment of sulfur and nickel atoms in these films.
4. The lack of segregation of niobium and titanium into the corrosion films suggests that the differences in corrosion resistance between these alloys are likely due to microstructure rather than film chemistry (i.e. chemical and/or mechanical stability in sulfuric acid).
5. Boron was not detected via EDS, XRD, or XPS on any of the surfaces studied. The effect of boron on the corrosion resistance is likely insignificant.

6. The difference in corrosion behavior of the Ni-Si-Ti alloy is a result of the single β_1 phase microstructure imparted by the presence of titanium. Niobium-rich G phases on the surfaces of Ni-Si-Nb and Ni-Si-Nb-Ti alloys act as cathodes and result in galvanic coupling between phases. The initial corrosion of the Ni-Si, Ni-Si-Nb, and Ni-Si-Nb-Ti alloys is likely controlled by galvanic cell reactions between phases in the alloy, whereas initial corrosion of the Ni-Si-Ti alloy is controlled by uniform attack over its single β_1-phase microstructure. Further work should be aimed at confirming this (possibly using electrochemical testing).
7. A model has been proposed to explain the formation of the passive SiO_2 film on these alloys. This model provides an estimate for film thickness. The estimated thicknesses are in reasonable agreement with the films observed on Ni-Si-Nb and Ni-Si-Nb-Ti alloy surfaces following 3 days of exposure.
8. It is proposed that Nb-rich precipitate phases (which are observed to form along grain boundaries) act to impede corrosion along grain boundaries. This may be a key mechanism by which niobium additions improve the corrosion resistance of Ni_3Si.
9. The process by which Ni_3Si alloys corrode occurs in different stages, each governed by a different mechanism. The corrosion mechanisms do not obey reaction controlled or diffusion controlled kinetics. Further work should be aimed at gaining a deeper understanding of these corrosion mechanisms.

6. FUTURE WORK

The present study has provided information regarding the way Ni_3Si alloys corrode in boiling 70 wt. % sulfuric acid. However, there are several missing pieces of information that will be critical to the further development of Ni_3Si alloys for the S-I thermochemical cycle. Not only will these be of interest to the application, but also to corrosion science. The future work which needs to be done is outlined below.

1. The decomposition loop of the S-I thermochemical cycle will contain sulfuric acid in the range of 50 – 98 wt. %. Further evaluation of these alloys in the full range of acid concentrations, temperatures, and pressures encountered in the S-I cycle needs to be performed.
2. In this study the corrosion behavior on Ni_3Si alloys has been evaluated over short and intermediate time intervals. These include active and passive periods of the corrosion process. However, for the S-I thermochemical cycle, the long term corrosion resistance (i.e. the passive region) is the most important factor. Therefore, corrosion testing over longer periods of time (i.e. months) needs to be performed to assure that the passive SiO_2 films provide protection indefinitely.
3. Corrosion testing under dynamic conditions needs to be performed to identify how erosion affects the corrosion resistance of these alloys. Under dynamic conditions the mechanical strength and adhesion of the film become important factors. These were not considered in the present study.
4. Film thicknesses need to be measured with time so that the kinetics of the film growth can be understood. Chemical analysis of corrosion test solutions following multiple many times also needs to be performed. Quantitative information regarding the film composition, thickness, and density can be deduced from these analyses.
5. The effect of pre-passivating Ni_3Si alloy surfaces in an oxidizing acid medium prior to corrosion testing should be explored. Zhang [2] found that pre-treatment of certain alloys in 70 wt. % nitric acid at room temperature improved corrosion

resistance in boiling sulfuric acid. The formation of a barrier film prior to testing will improve the corrosion resistance in more corrosive acid environments.

6. The effect of applying a silica coating to the alloy surfaces should be explored. Silica coatings should have similar effects to pre-treating the surface in an oxidizing acid medium, however, this method has the advantage of being able to control the film thickness.
7. An electrochemical testing method to evaluate these alloys in boiling sulfuric acid needs to be developed. Zhang [2] performed room temperature electrochemical analyses in concentrated sulfuric acid, however, electrochemical testing in boiling temperature sulfuric acid has not been done.
8. To better understand how the microstructure affects the corrosion of $Ni_3Si_{20}(Nb,Ti)_3$ alloys, single α, β_1, γ, and G phase compounds should be fabricated and evaluated in sulfuric acid.

REFERENCES

1. K. Ohira, Y. K., H. Tsuda, T. Takasugi (2005). Intermetallics 14(4): 367-376.

2. Zhang, S. (2000). The Development of Nickel Silicide based Alloy For Sulfuric Acid Application. Metallurgical Engineering. Rolla, University of Missouri-Rolla. Ph.D: 155.

3. R.G. Davis, N. S. S. (1965). TMS-AIME 233: 714.

4. K. Aoki, O. I. (1978). Trans. Jpn. Inst. Metals 19: 203.

5. E.M. Schulson, L. J. B., I. Baker (1990). Acta Metallurgica 38: 207-213.

6. C.T. Liu, W. C. O. (1991). Scripta Metallurgica 25: 1933-1937.

7. J.S. Jang, C. H. T. (1992). High Temperature Aluminides and Intermetallics: Part 2.

8. T. Takasugi, H. K., Y. Kaneno (2001). Materials Science and Technology 17: 671-680.

9. Kumar, P. (1984). Mat. Res. Soc. Symp. Proc., Boston, MA.

10. T. Takasugi, D. S., O. Izumi, M. Hirabayashi (1990). Acta Metallurgica 38: 739

11. C.T. Liu, E. P. G., W.C. Oliver (1996). Intermetallics 4: 77-83.

12. N. B. Pilling, R. E. B. (1923). J. Inst. Met. 29: 529.

13. Wagner, C. (1933). Z. Physik Chemie 21: 25.

14. N. Cabrera, N. F. M. (1949). Reports on Progress in Physics 12(1): 163-184.

15. F. P. Fehlner, N. F. M. (1970). Oxid. Met. 2: 59.

16. Castro, E. B. (1994). Electrochimica Acta 39: 2117-2123.

17. Castro, E. B. (1998). 4th International Symposium on Electrochemical Impedance Spectroscopy, Rio De Janeiro.

18. C. Y. Chao, L. F. L., D. D.Macdonald (1981). J. Electrochem. Soc.: Electrochemical Science and Technology 128(6): 1187-1194.

19. V. barbarossa, S. B., M. Diamanti, S. Sau, G. De Maria (2005). International Journal of Hydrogen Energy 31: 883-890.

20. Crist, B. V. (2000). Handbook of Monochromatic XPS Spectra - The Elements and Native Oxides. New York, NY, John Wiley & Sons.

21. C. D. Wagner, A. V. N., A. K. Vass, J. W. Allison, C. J. Powell, J. R. Rumble Jr. NIST X-ray Photoelectron Spectroscopy Database, NIST. 20.

APPENDIX A
MODELS FOR PASSIVE FILM GROWTH

In 1924 Carl Wagner proposed a model [13] that derived from the earlier work of Nernst and Debye, who developed a mathematical treatment for the diffusion of ions in electrolytes. Wagner's theory of oxidation rests on the assumption that metal oxidation proceeds via the diffusion of charged particles. He considered only thick, adherent, and stoichiometric corrosion films in his analysis. His assumptions were the following: 1) diffusion of charged species (cations, anions, electrons, or electron holes) is the rate limiting process, 2) thermodynamic equilibrium is present at the metal/oxide and oxide/gas interface, 3) the oxide composition is stoichiometric, and 4) oxygen does not diffuse across the metal/oxide interface. There are two fundamental driving forces for diffusion in Wagner's theory. First, because thermodynamic equilibrium exists at both interfaces, oxygen and metal concentration gradients across the film give rise to chemical potential. Second, as a result of the chemical potential, oxygen and metal ions diffuse across the oxide in opposite directions. The resulting motion of these charged particles gives rise to an electric field, which adds an additional driving force. Using the linear diffusion equation for charged particles provided by Nernst and Debye , Wagner derived coupled expressions for the flux of cations, anions, and electrons across the oxide:

$$J = -D\frac{\partial C}{\partial x} + \mu EC \tag{1}$$

where E is the electric field and μ is the mobility of the diffusing species. E and μ are related to the diffusion coefficient D through the Einstein relation $ZeD = \mu k_B T$, where Z is the valence of the diffusing species, e is the charge, and k_B is Boltzmann constant. The resulting total ionic flux is related to the chemical and potential gradients by:

$$J_{x,i} = -\frac{\sigma_i}{(z_i e)^2}\left[\frac{d\mu_i}{dx} + (z_i e)\frac{d\phi}{dx}\right] \tag{2}$$

From Equation 2 we see that the total ionic flux is linearly dependent on the gradients of the chemical potential and electric field. If it is assumed that one of the three charged species does not exhibit significant flux across the oxide (which is the case for

oxygen/sulphur in metal/film/gas systems), then the other two coupled expressions, J_c and J_e in Equation 2, can be solved to find L(t). This yields the same parabolic growth behaviour, $L(t) = \sqrt{2kt}$, as derived by Pilling and Bedworth in Equation 1.1, however the rate constant k now takes on the form:

$$k = \frac{D_C}{2} \ln\left(\frac{P_O}{P_i}\right) \tag{3}$$

where D_C is the diffusion coefficient of the metal cation in the oxide, and P_o and P_i are the partial pressures of oxygen in the gas and oxide respectively. Unlike the Pilling-Bedworth parabolic growth rate theory, the rate constant derived by Wagner is a function of the partial pressure of oxygen P_o and P_i, temperature T, cation conductivity σ_c, cation concentration C_c, and the cation valence Z_c ($D_c \alpha T, \sigma_c, C_c, Z_c$). Wagner's theory successfully accounts for the effects of charged particle diffusion in corrosion films, however it does have fundamental flaws. Very few metal systems (e.g. NiO and CoO are a few exceptions) exhibit true parabolic growth kinetics. Most pure metals, and nearly all metal alloys, deviate from this behaviour. The problems with Wagner's theory result from the assumptions made. First, corrosion films are rarely compact, completely adherent, and stoichiometric. Second, the condition of thermodynamic equilibrium at the metal/film and film/gas interfaces is unrealized in most experiments. Third, the diffusion of charged species results solely from the necessity to maintain electroneutrality within the film. Wagner made two key assumptions in order to solve Equation 4 for the film thickness. First, he approximated the flux of anions within the film to be negligible ($J_a = 0$). Secondly, a condition of electroneutrality, $Z_cJ_c + Z_eJ_e = 0$, was stipulated such that the linear system of equations shown in Equation 2 could be solved. The condition of electroneutrality provides a means to obtain L(t), however it is not based on any empirical evidence.

In the 1940's a number of models for passive film growth in aqueous solution were developed which identified high electric field strength as the primary initiator of film growth. These theories fall under the general classification of high-field model (HFM). The Cabrera-Mott model (CMM) [14] is perhaps the most well known HFM.

CMM has previously been reviewed in depth by MacDonald [18]. Cabrera and Mott based their model on four assumptions: 1) The film grows via cation diffusion through the film to the film/solution interface where they are reacted with the electrolyte, 2) The driving force for cation diffusion is a high electric field strength within the oxide, 3) The total potential drop and the electric field strength are both independent of the oxide thickness L, and 4) The rate-limiting step of the film growth is the dissolution of metal cations into the film at the metal/film interface. On the basis of these assumptions Cabrera and Mott derived the following rate equation:

$$\frac{dL}{dt} = N\Omega\upsilon e^{\frac{(-E_a + \frac{qa\phi_f}{2L})}{kT}} \tag{4}$$

Integration of Equation 4 by parts yields a Taylor series of L. Neglecting higher order terms (n > 0) yields an inverse logarithmic rate law:

$$L(t) = \frac{1}{C - D\ln(t)} \tag{5}$$

$$C = \frac{2}{qa\phi_f}\left\{E_a - kT\ln\left[\frac{2(E_a - 39kT)^2 N\Omega\upsilon}{\phi_f aqkT}\right]\right\}$$

$$D = \frac{2kT}{qa\phi_f}$$

In the 1970's Fehlner and Mott [15] provided a modified version (FMM) of the Cabrera-Mott model that included the linear dependence of the activation energy on film thickness (which CMM did not). Their assumptions were as follows: 1) The film grows via anion diffusion through the film, 2) The activation energy E_a is linearly proportional to the film thickness L(t), 3) The electric field strength is independent of the film

thickness L, and 4) The rate-limiting step of the film growth is the emission of anions into the film at the film/solution interface. They assumed that the activation energy took the form $E_a = E_{a0} + \mu L$, which replaced the E_a term in Equation 5. From here they integrated the dL/dt expression to obtain a logarithmic growth rate, which is shown below in Equation 6.

$$L = A' + B' \ln(t + t_0) \tag{6}$$

$$A' = \frac{kT}{\mu}\left[\ln\frac{\mu}{kT} + \ln N\Omega\upsilon - \frac{E_{a0}}{kT} + \frac{qa\varepsilon}{2KT}\right]$$

$$B' = \frac{kT}{\mu}$$

Up until the mid 1970's, models for passive film growth had little experimental data to compare with. Therefore, a critical assessment of the high-field models was not possible. In the 1980's experimental data began to show that the Cabrera-Mott moc along with other versions of HFM, were flawed.

Castro [16] pointed out that transition metals such as Fe and Ni commonly exhibited passive films with chemical gradients, which suggested that the field strength was not constant throughout the film. This fundamentally disagreed with the third assumption of the Cabrera-Mott model. This also raised the question of whether the driving force for ionic diffusion arose only from high electric field strength since the build-up of ionic species would result in a chemical potential. MacDonald pointed out that logarithmic growth behaviour observed on metals in low pH environments where film dissolution is significant was not explained by the CMM because it doesn't consider the effects of film dissolution. Further, radioactive tracer studies done on several metal systems found that anion diffusion was largely responsible for film growth. This refuted CMM's assumption that ion transport occurs only via cation diffusion. The Fehlner-Mott model, which does consider anion diffusion, has also been criticized. Studies involving

rapid changes in the applied potential showed that the equilibrium reaction $O_{oxide} + 2H^{+}_{aq} + 2e^{-} \leftrightarrow H_2O$ is rapidly established. This result disagreed with FMM's assumption that the rate limiting step is the emission of anions into the oxide at the film/solution interface.

Perhaps the most successful model for passive film behaviour proposed to date was provided by MacDonald [18] in 1981. Since then he and other authors have made several extensions to the original. The point defect model (PDM) fundamentally differs from high-field models in that it identifies point charge defects as the primary transport of charge through the film. A high concentration of point defects ($> 10^{20}$ cm^{-3}) is assumed to create a network of ion vacancies and electron holes by which oxide growth and dissolution occurs. The role of ion vacancies in the growth and dissolution of the film can be summarized as follows; 1) Film growth results from the oxidation of metal cations at the metal/film interface and the filling of anion vacancies at the film/solution interface, and 2) Film dissolution results from the creation of cation vacancies at the film/solution interface. Furthermore, MacDonald assumed the rate determining step to be the filling of anion vacancies by metal cations at the metal/film interface. Similar to HFM, PDM assumes a high electric field ($\sim 10^{6}$ Vcm^{-1}) within the oxide. However, due to the high concentration of electron holes assumed in this model, the tunnelling of electrons impedes this field and lessens its strength. The impedance prevents the electric field strength from exceeding the breakdown strength of the film and thus protects the film from self destructing.

PDM has been able to successfully account for the linear dependence of film thickness on the potential, as well as the exponential dependence of the steady state current on the potential. In addition, MacDonald was also able to incorporate four new parameters into the expression for dL/dt, all of which he felt had an effect on the gr rate of the oxide. They are as follows; 1) $\varphi_{f/s}$ (An intrinsic constant), 2) α (The potentıaı dependence of $\varphi_{f/s}$), 3) β (the pH dependence of $\varphi_{f/s}$), and 4) ε (the electric field strength). The initial rate equation proposed by MacDonald is given below in Equation 7.

$$\frac{dL}{dt} = \frac{A(B-1)}{e^{2KL} - 1} \qquad (7)$$

$$A = 2KD_{v0}e^{\left[-\frac{2F}{RT}(\alpha V_{ext}+\beta pH+\phi_{f/s}{}^{0})+\frac{\Delta G_{31}{}^{0}}{RT}-4.606\,pH\right]}$$

$$B = e^{\left[\frac{2F}{RT}(V_{ext}+\phi_{R})-\frac{2\Delta G_{21}{}^{0}}{xRT}-\frac{\Delta G_{31}{}^{0}}{RT}+4.606\,pH\right]}$$

Integration of Equation 8 gives the following modified logarithmic rate law:

$$e^{2KL} - 2KL - 1 = 2KA(B-1)t \tag{8}$$

MacDonald observed that for most anodic films, the field strength is on the order of 10^6 Vcm^{-1}, and therefore the $2KL = 2F_{\varepsilon}L/RT \approx .75L$. Thus if $L \geq 5$Å then $\exp(2KL) >> 2KL >> 1$, and Equation 8 can be simplified to:

$$L_T(t) = \frac{1}{2K}\ln 2KA(B-1) + \ln t \tag{9}$$

For small thicknesses, Equation 9 can be manipulated by expanding the exp (2KL) term (i.e. $\exp(2KL) = 1 + 2KL + 2K^2L^2 + 4/3K^3L^3 + \ldots$) and dropping the higher order terms (i.e. $n > 2$). Equation 10 shows a $t^{1/2}$ dependence of the film thickness for very thin films.

$$L_S(t) = \sqrt{t\frac{A(B-1)}{K}} \tag{10}$$

APPENDIX B

CORROSION BEHAVIOR IN 50 WT. % SULFURIC ACID

Figure 1 displays an image of Ni_3Si alloys following three days of exposure to boiling 50 and 70 wt. % sulfuric acid solution. The images were captured with a 35 mm DSLR camera. The magnified images were captured with an optical microscope.

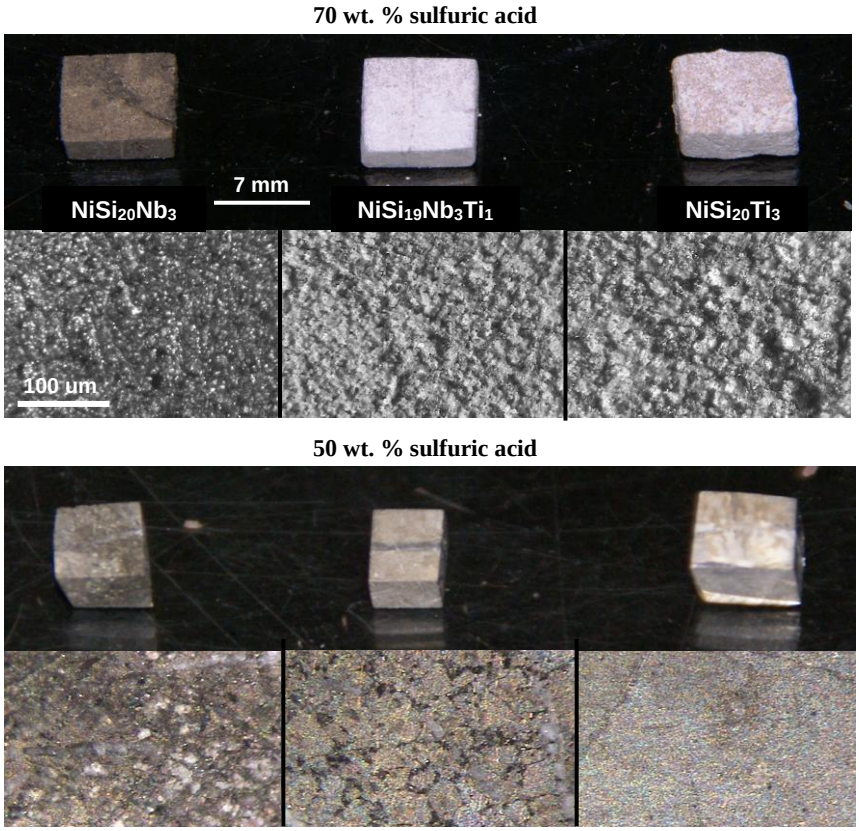

Figure 1 Optical images of Ni-Si-Nb, Ni-Si-Nb-Ti, and Ni-Si-Ti alloys following 3 days of exposure to boiling 50 and 70 wt. % sulfuric acid.

There are noticeable differences in the appearance of alloys shown in Figure 1 following three days in solution. The alloys exposed to 70 wt. % solution each have obvious corrosion films on their surfaces, as discussed in the body of the text. The morphologies range from relatively smooth on the Ni-Si-Nb alloy, to very course and grainy on that of the Ni-Si-Ti alloy. Their behavior in 50 wt. % solutions was markedly different. The surfaces were significantly less coarse, and no spallation was observed on any of the alloys. Table 1 lists the corrosion rates in 50 and 70 wt. % sulfuric acid.

Table 1 The corrosion rates of Ni_3Si based alloys following 3 and 6 days of exposure to boiling 50 and 70 wt. % sulfuric acid.

Alloy	Corrosion Rate (mpy)		
	50 wt. % H_2SO_4 140 °C	70 wt. % H_2SO_4 165 °C	
	3 days	1st 3 days	6 days/2nd 3 days
Ni-Si	78	61	43 / 9
Ni-Si-Nb	309	19	13 / 7
Ni-Si-Ti	25	952	517 / 98
Ni-Si-Nb-Ti	212	151	80 / 8

APPENDIX C

THE CORROSION BEHAVIOR OF A NI-SI-NB ALLOY WITH RARE EARTH ADDITIONS

In addition to the four alloy compositions discussed throughout the body of the text, an additional Ni-Si-Nb-Re alloy was studied as well (Re represents cerium and lanthanum in a ~ 4:1 atomic ratio). The composition is shown in Table 1. The compositions of the four alloys discussed throughout the body of the text are shown for comparison.

Table 1 Composition of the Ni-Si-Nb-Re alloy (at. %). The compositions of the four alloys discussed in the body of the text are shown for comparison.

Alloy	Heat treatment	Alloy composition					
		Ni	Si	Nb	Ti	B	Re*
"Ni-Si" $NiSi_{22}B_{0.01}$	900 °C for 24 hours in Ar	78.87	21.12	-	-	0.01	-
"Ni-Si-Nb" $NiSi_{20}Nb_3B_{0.05}$	900 °C for 24 hours in Ar	77.08	19.69	3.05	-	0.02	-
"Ni-Si-Ti" $NiSi_{20}Ti_3B_{0.025}$	900 °C for 24 hours in Ar	77.40	19.77	-	2.83	0	-
"Ni-Si-Nb-Ti" $NiSi_{19}Nb_3Ti_1B_{0.05}$	900 °C for 24 hours in Ar	79.17	17.02	3.16	0.66	0	-
"Ni-Si-Nb-Re" $NiSi_{20}Nb_3B_{0.05}Re_{0.05}$	**900 °C for 24 hours in Ar**	**76.13**	**20.54**	**3.23**	**-**	**0.05**	**0.05**

*Re was added in the form of mischmetal. The composition of the mischmetal is (as determined from standardless EDS analysis): ~ 80 at. % Ce and 20 at. % La.

Figure 1.a. shows the mass loss of the Ni-Si-Nb-Re alloy in boiling 70 wt. % sulfuric acid. The testing conditions used for this alloy were identical to the other four alloys studied. Figure 1.b. displays a logarithmic representation of the data. The corrosion rates over the different corrosion regions outlined in this figure are listed in Table 2.

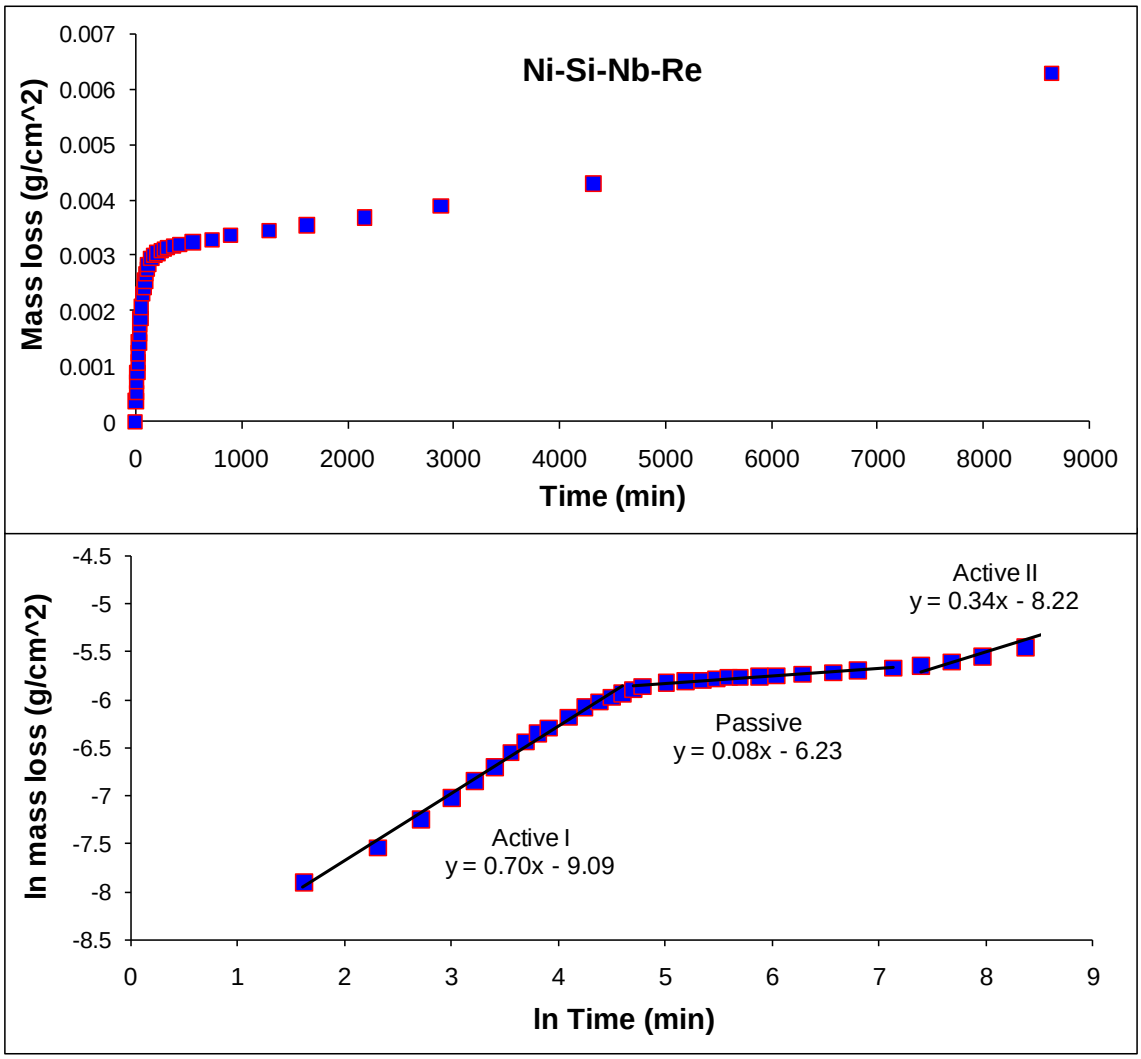

Figure 1 a) The mass loss of Ni-Si-Nb-Re in boiling 70 wt. % sulfuric acid, and b) logarithmic plot of the mass loss data shown in part a).

Table 2 Comparison of the corrosion rate of the Ni-Si-Nb-Re alloy with the alloys studied in the body of the text.

Alloy	**Corrosion Rate (mpy)**			
	Active I	Active II	Passive	Total
Ni-Si	2138	-	9	43
Ni-Si-Nb	13	-	-	13
Ni-Si-Ti	1287	7743	158	517
Ni-Si-Nb-Ti	732	1890	11	80
Ni-Si-Nb-Re	**633**	**10**	**16**	**19**

APPENDIX D

AUGER ANALYSES OF CORRODED ALLOY SURFACES

Ni-Si-Nb

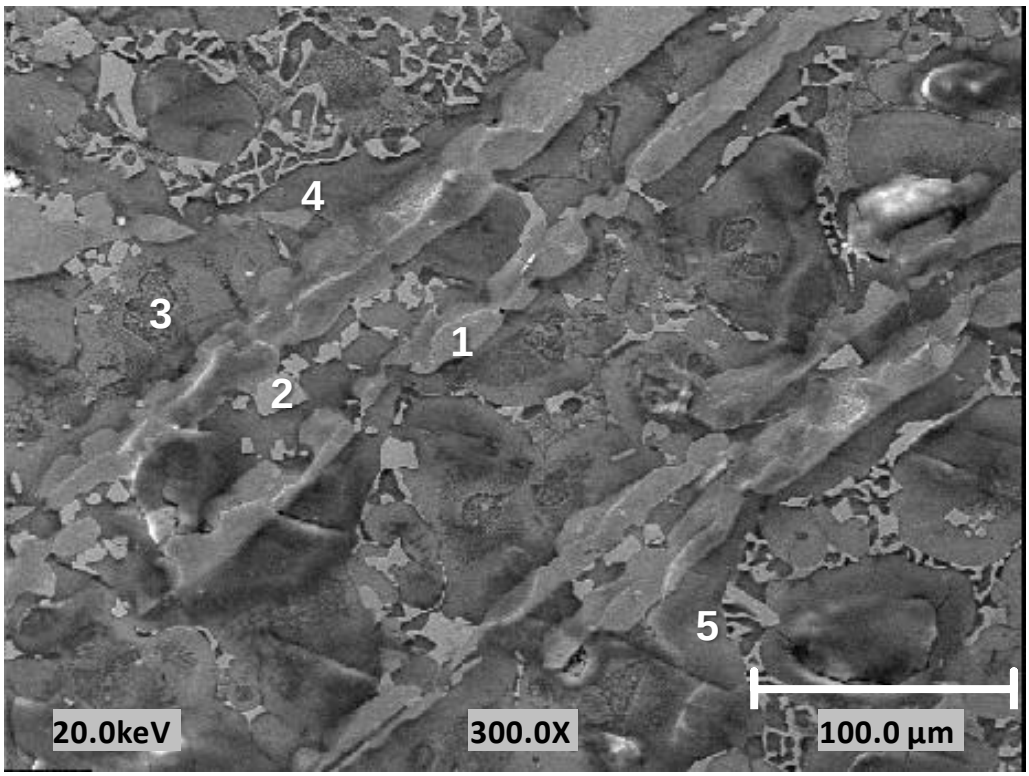

	Composition (at.%)				
Area	**C**	**O**	**Si**	**Ni**	**Nb**
1	0.0	62.7	34.2	3.1	0.0
2	0.0	67.7	27.7	2.4	2.2
3	0.0	67.0	30.4	2.5	0.0
4	0.0	66.9	28.2	3.5	1.4
5	0.0	64.6	32.1	2.0	1.3

Figure 1 Backscatter electron image of an Ni-Si-Nb alloy surface that was corroded for 1 minute in boiling 70 wt. % sulfuric acid. The compositions of areas 1-5 are listed in the table.

Ni-Si-Nb-Ti

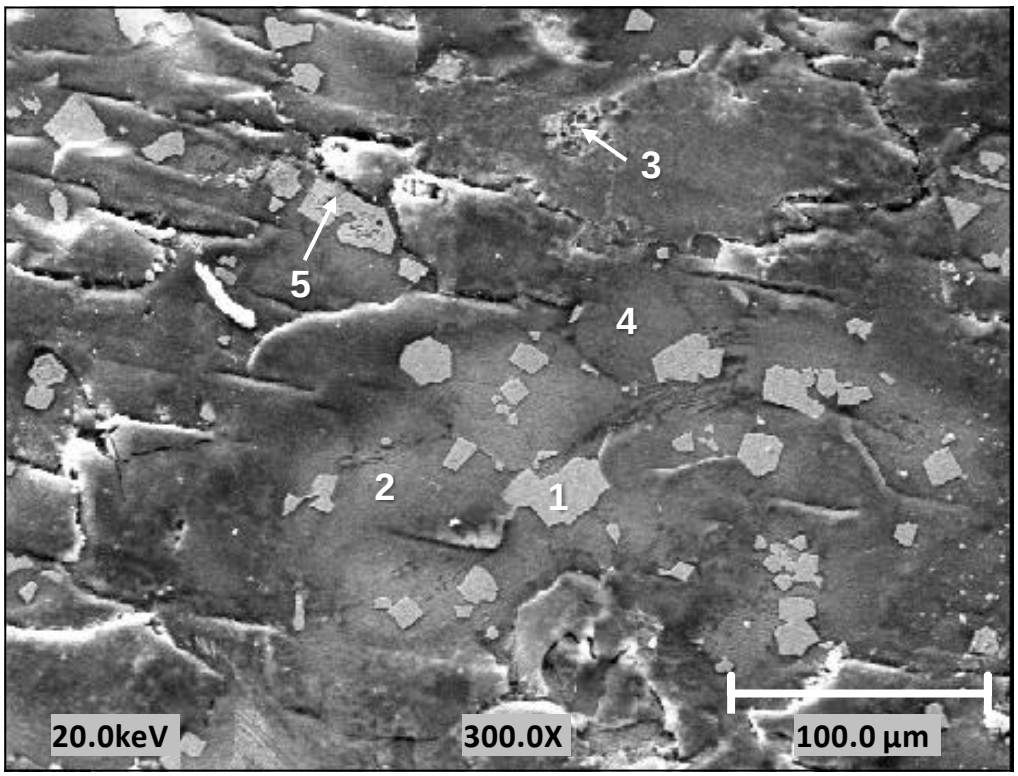

	Composition (at.%)					
Area	**C**	**O**	**Si**	**Ni**	**Nb**	**Ti**
1	0.0	63.0	8.3	27.1	0.0	1.6
2	0.0	61.0	32.1	0.0	2.7	4.2
3	0.0	52.4	5.2	32.5	9.8	0.0
4	0.0	62.3	31.4	0.0	6.3	0.0
5	0.0	56.6	23.6	17.0	0.0	2.8

Figure 2 Backscatter electron image of an Ni-Si-Nb-Ti alloy surface that was corroded for 1 minute in boiling 70 wt. % sulfuric acid. The compositions of areas 1-5 are listed in the table.

Ni-Si-Ti

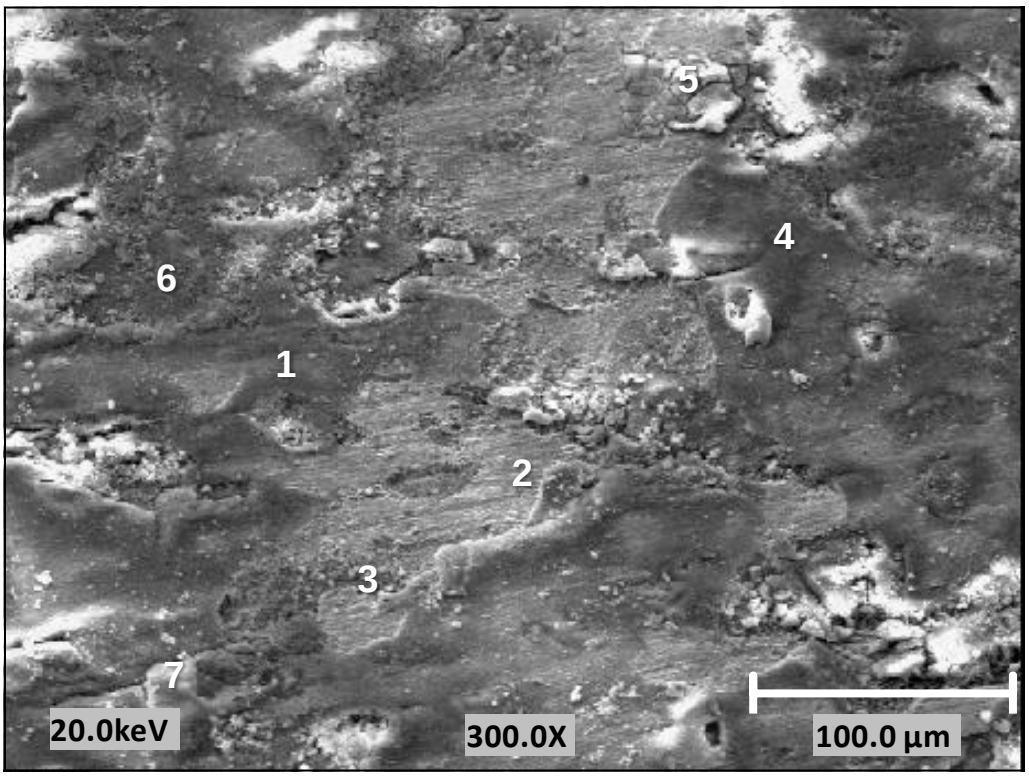

	Composition (at.%)				
Area	**C**	**O**	**Si**	**Ni**	**Ti**
1	0.0	47.2	39.1	10.6	3.2
2	0.0	68.7	10.4	19.2	1.7
3	4.4	58.3	11.8	25.5	0.0
4	0.0	49.9	24.0	23.6	2.5
5	0.0	60.0	10.3	29.7	0.0
6	0.0	51.0	33.5	15.5	0.0
7	0.0	63.1	27.7	9.2	0.0

Figure 3 Backscatter electron image of an Ni-Si-Ti alloy surface that was corroded for 1 minute in boiling 70 wt. % sulfuric acid. The compositions of areas 1-7 are listed in the table.

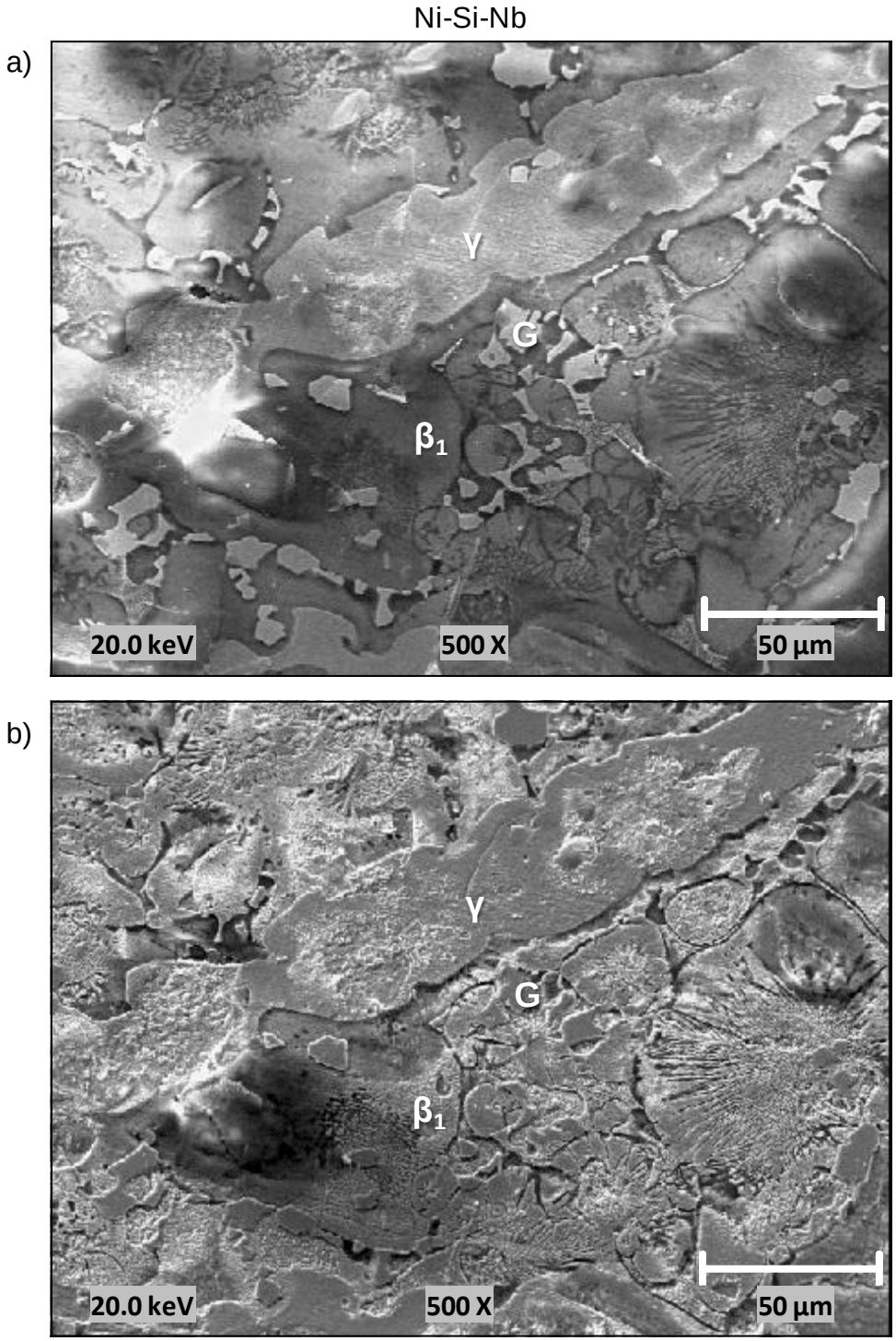

Figure 4 BSE images taken a) before, and b) after sputter profiling of a Ni-Si-Nb alloy surface that was corroded in boiling 70 wt. % sulfuric acid for one minute. Auger composition maps of the β_1, γ, and G phases labeled in this figure are shown in Figure 5.

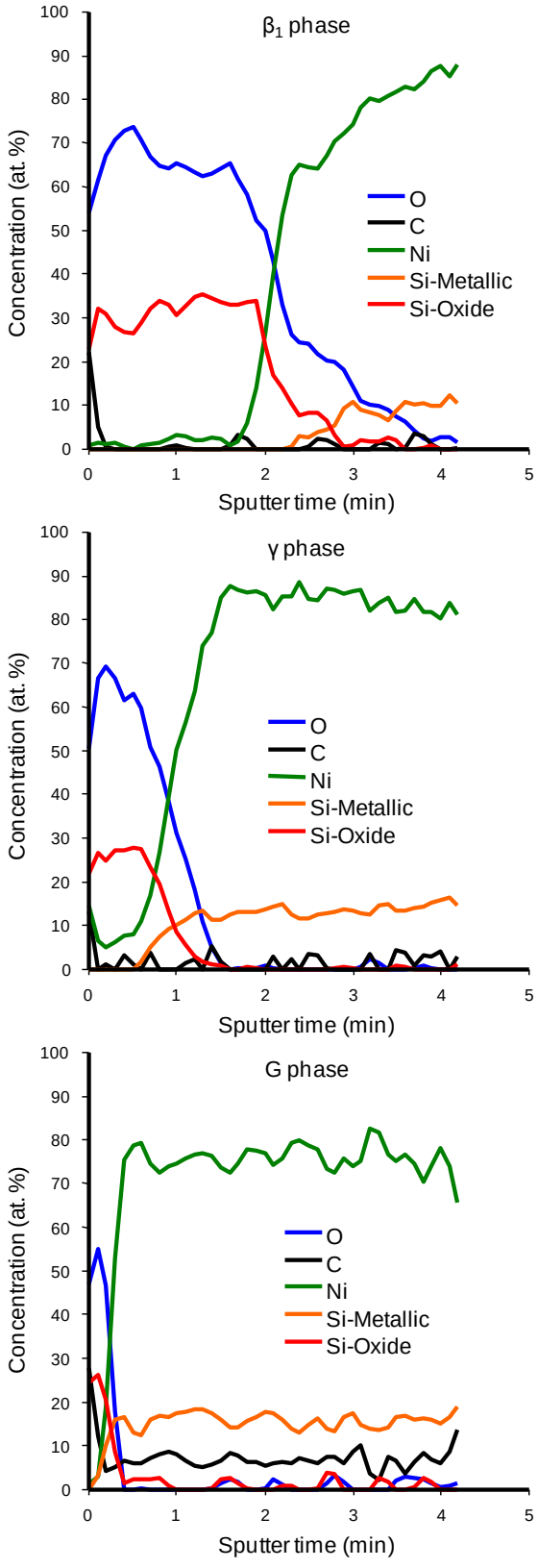

Figure 5 Sputter profiles of the β_1, γ, and G phases labeled in Figure 4. A sputter rate of 150 nm/min was used.

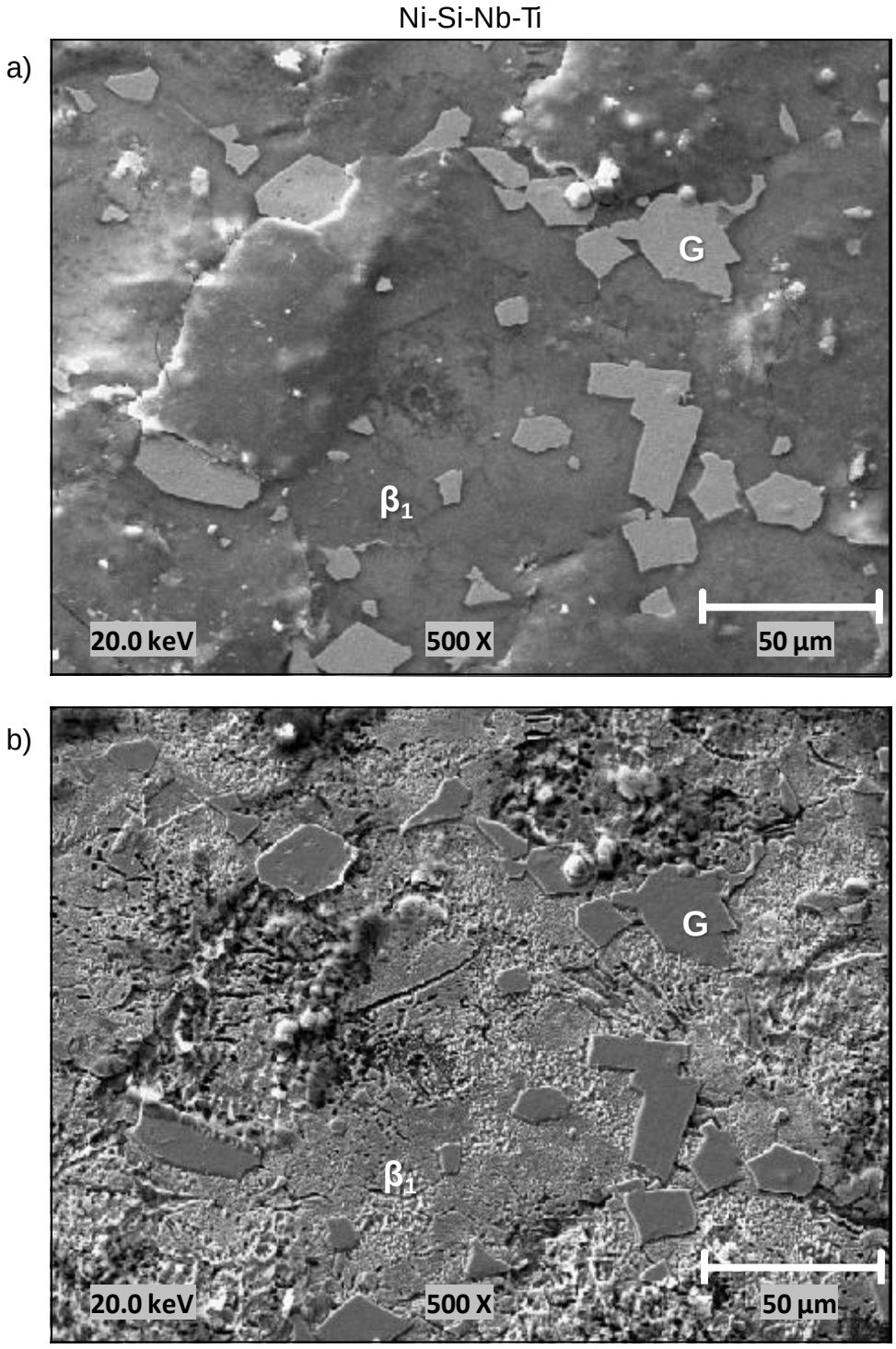

Figure 6 BSE images taken a) before, and b) after sputter profiling of a Ni-Si-Nb-Ti alloy surface that was corroded in boiling 70 wt. % sulfuric acid for one minute. Auger composition maps of the β_1 and G phases labeled in this figure are shown in Figure 7.

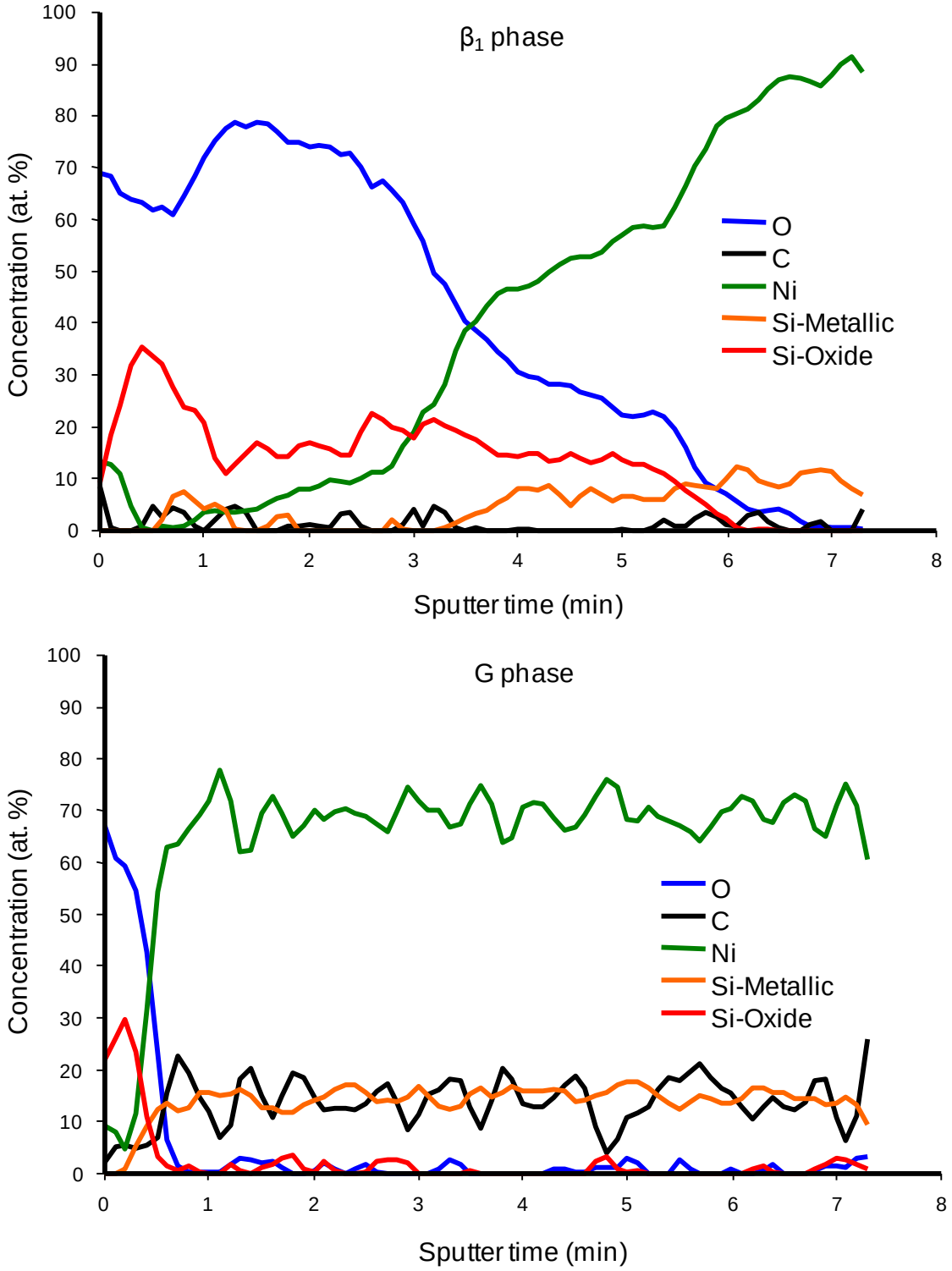

Figure 7 Sputter profiles of the β_1 and G phases labeled Figure 6. A sputter rate of 150 nm/min was used.

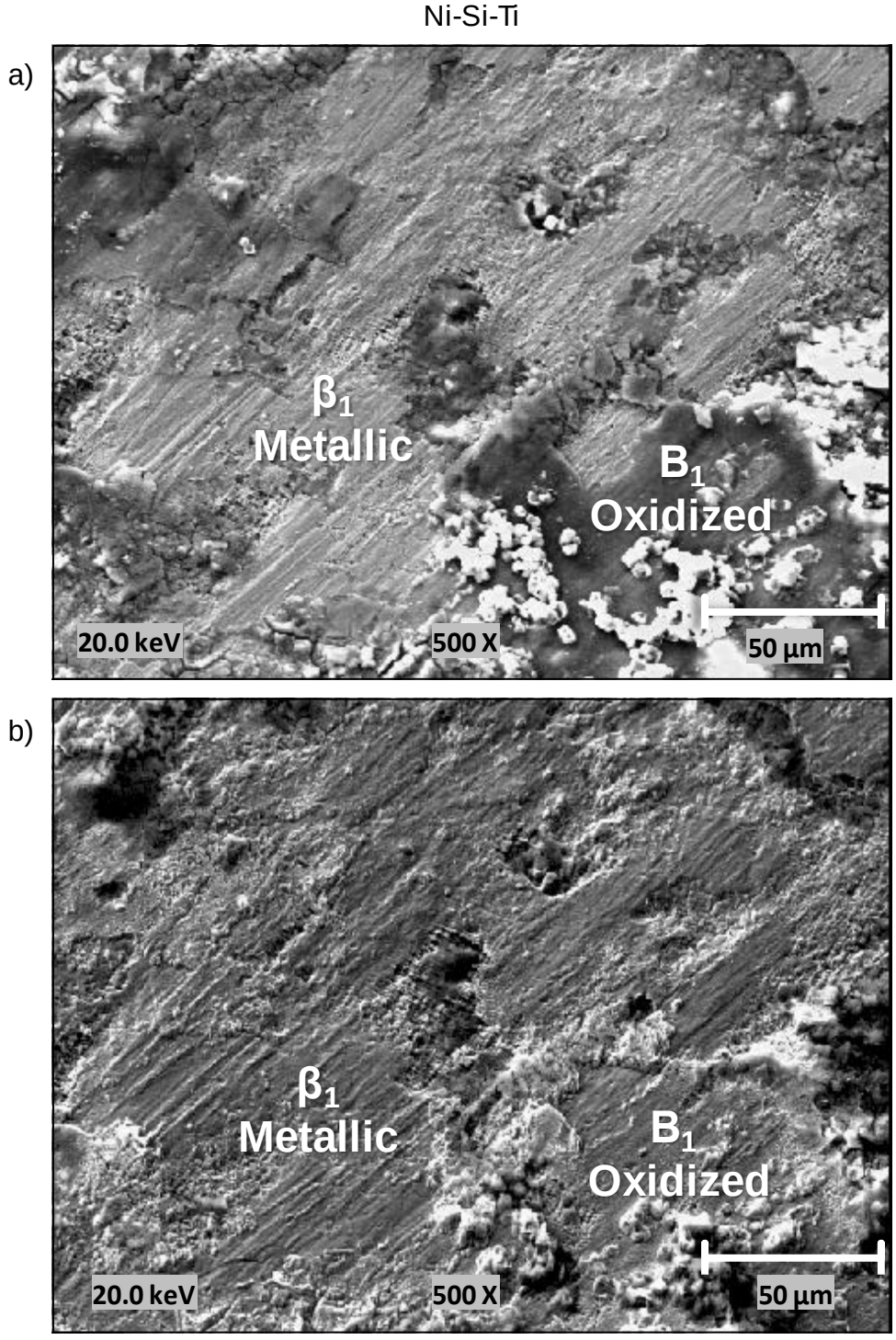

Figure 8 BSE images taken a) before, and b) after sputter profiling of a Ni-Si-Ti alloy surface that was corroded in boiling 70 wt. % sulfuric acid for one minute. Auger composition maps of the oxidized and metallic β_1 phases labeled in this figure are shown in Figure 9.

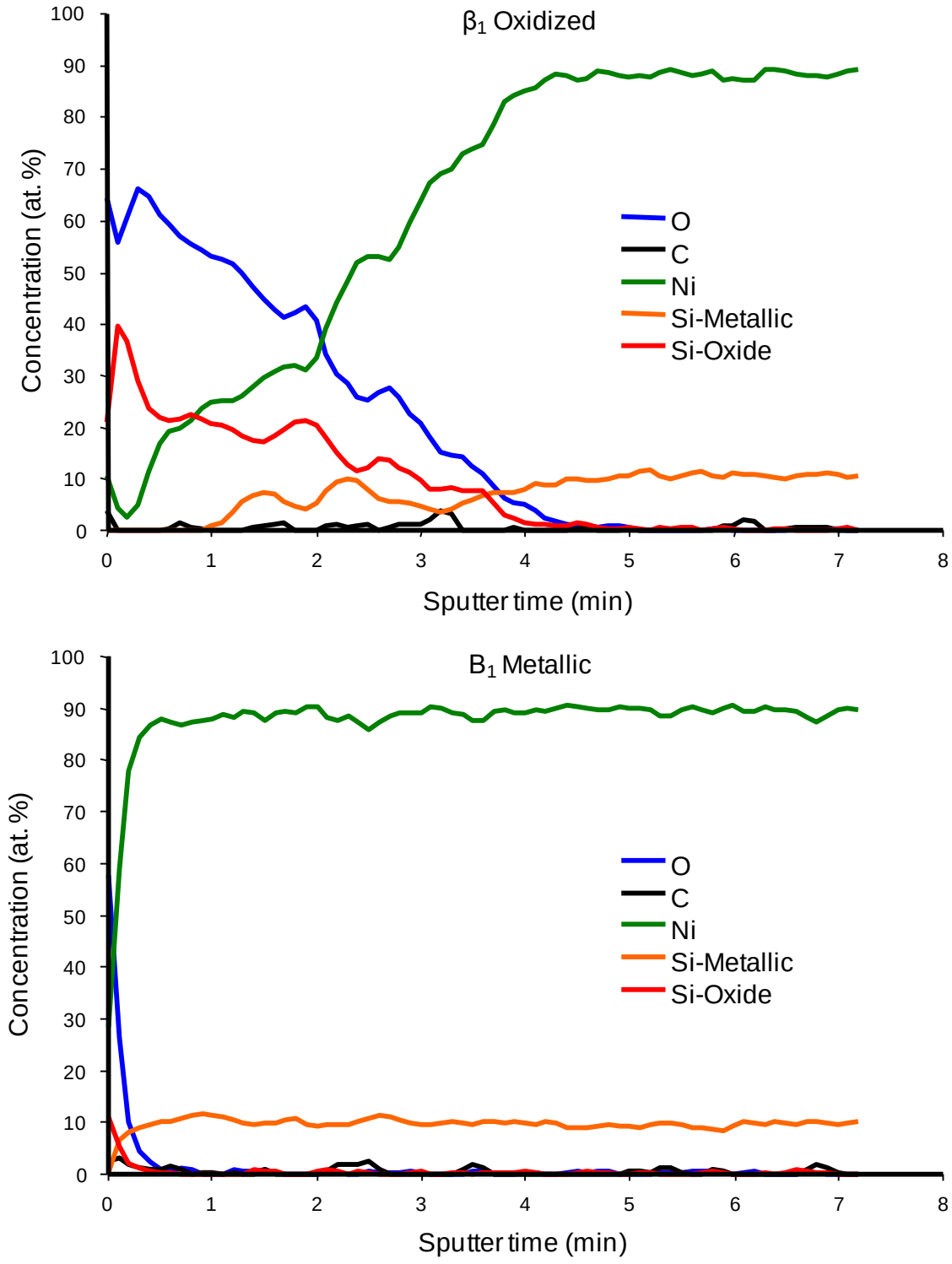

Figure 9 Sputter profiles of the oxidized and metallic $\beta_1$phases labeled Figure 8. A sputter rate of 150 nm/min was used.

VITA

Christopher Marc Larson was born in Iowa City, Iowa on October 2, 1983 to Warren and Mary Larson. Christopher grew up in Iowa City where he attended West High School. After graduating in May of 2002, he enrolled in the physics program at Coe College and graduated in May, 2006. He was a member of the Sigma Pi Sigma National Physics Honors Society and the baseball team. Chris obtained his Master's degree in Materials Science and Engineering from the Missouri University of Science & Technology in May, 2009. In February, 2009 Chris accepted a position at Kennedy Space Center as a Materials Engineer.